Solution-processed submicron chalcopyrite absorbers for thin film solar cells

Von der Fakultät für Ingenieurwissenschaften, Abteilung

Maschinenbau und Verfahrenstechnik der

Universität Duisburg-Essen

zur Erlangung des akademischen Grades

eines

Doktors der Naturwissenschaften

Dr. rer. nat.

genehmigte Dissertation

von

Yao Gao

aus

Guangxi, China

Gutachter: Univ.-Prof. Dr. rer. nat. Markus Winterer

Univ.-Prof. Dr. rer. nat. Martina Schmid

Tag der mündlichen Prüfung: 28. 06. 2024

Contents

Abstract

Photovoltaic (PV) devices can directly convert sunlight into electricity. So far, the Si-wafer-based PV module is the dominant product of the global PV market. There are still thin-film PV module productions. They occupy a small share of the total global PV market, including cadmium telluride, amorphous silicon (a-Si), and copper indium (gallium) diselenide (CIGSe). The thickness of thin film solar cells can be about 100 times thinner than Si-based PV, since they can absorb most of the illumination light owing to their high absorption coefficient. The efficiency of lab-scale CIGSe solar cells has achieved 23.6% (vacuum-based process), comparable with the Si-based technology. The alternative solution process has been applied for CIGSe solar cell fabrication, owing to low equipment cost and high material utilization. So far, the efficiency of the state-of-the-art solution-processed CIGSe has achieved 18.1% via a hydrazine precursor solution. However, hydrazine is a highly toxic and reactive solvent and, therefore, it is necessary to protect the human body and the environment by using appropriate protective equipment to prevent physical contact or exposure to either vapor or liquid.

Due to hydrazine's shortcomings, the hydrazine solution is not beneficial for mass production. Thus, developing a non-toxic solution precursor for absorber fabrication has attracted great attention. The fabrication cost of CIGSSe solar cells can be further reduced by thinning the absorber thickness. In this thesis, solution-processed submicron copper indium sulfoselenide (CISSe) and copper indium gallium sulfoselenide (CIGSSe) solar cells are fabricated on molybdenum (Mo) and tin-doped indium oxide (ITO) back contacts by a less toxic N, N-Dimethylformamide (DMF) solution.

In the first results chapter of this thesis, annealing conditions are investigated, including annealing in pure selenium and a mixture of S and Se (sulfur and selenium) atmospheres. With increasing selenium content for annealing, the corresponding CISSe devices present better PV parameters. After sulfur doping, the open circuit voltage and fill factor of CISSe solar cells are significantly improved, leading to higher efficiency than annealing in pure selenium atmosphere. The open circuit voltage of the S and Se co-annealed CISSe solar cell can reach over 600 mV, which is remarkably higher than reported in the literature.

The second results chapter of this thesis focuses on PV performance improvement by sodium chloride (NaCl) solution treatment. Three strategies for Na incorporation into solution-processed CISSe by soaking in NaCl aqueous-ethanol solution are researched, either prior to absorber deposition (pre-deposition treatment, Pre-DT), before selenization (pre-selenization treatment, Pre-ST), or after selenization (post-selenization treatment, PST). The Pre-ST CISSe solar cells achieve a better PV performance than those from the other two strategies of Na incorporation. For optimization, soaking times (5 min, 10 min, and 15 min) and NaCl concentrations (from 0.2 M to 1.2 M) of the Pre-ST are researched. When the precursor films are soaked in 1 M NaCl for 10 min, CISSe solar cells achieve an efficiency of 9.6%.

The third results chapter of this thesis is a CISSe absorber prepared on transparent conductive oxide (TCO) back contact through an environmentally benign solution, which shows great potential in the bifacial application. Ultra-thin (around 550 nm) CISSe solar cells were successfully deposited on ITO back contact via spin-coating of metal-chloride DMF solution followed by selenization. With increasing the absorber thickness to sub-micron (740 nm), the solar cells not only exhibited a higher short-circuit current density but also an improved fill factor compared to the ultra-thin devices, which results in an efficiency enhancement. Furthermore, NaCl solution pre-selenization treatment was demonstrated to improve the performance of CISSe solar cells.

In the fourth part of this thesis, the parasitic absorption in CIGSSe solar cells emerging from the Mo back contact can be significantly reduced by replacing it with ITO back contact. However, an undesirable GaO_x layer forms at the CIGSSe/ITO interface during the high-temperature selenization process, which hinders photo-carrier extraction. A thin Cu-In-TU-DMF (TU: thiourea, DMF: N, N-Dimethylformamide) intermediate layer for modification of the CIGSSe/ITO interface, which can reduce the recombination at the rear interface. Furthermore, carrier transport and collection are improved, leading to a significant improvement in efficiency.

Zusammenfassung

Photovoltaische (PV) Bauelemente können Sonnenlicht direkt in Strom umwandeln. Bisher dominiert das Si-Wafer-basierte PV-Modul den globalen PV-Markt. Die Produktion von Dünnschicht-PV-Modulen nimmt immer noch einen kleinen Anteil am gesamten globalen PV-Markt ein, einschließlich Dünnschicht-Modulen aus Cadmium-Tellurid, amorphem Silizium (a-Si) und Kupfer-Indium(-Gallium)-Diselenid (CIGSe). Aufgrund ihres hohen Absorptionskoeffizienten kann die Dicke von Dünnschicht-Solarzellen etwa 100-mal geringer sein als bei PV auf Si-Basis, und dennoch den größten Teil des Beleuchtungslichts absorbieren. Der Wirkungsgrad von CIGSe-Solarzellen aus vakuumbasierten Prozessen im Labormaßstab hat 23,4 % erreicht, vergleichbar mit der Si-basierten Technologie. Das alternative Flüssigphasenverfahren auf Basis von Lösungen weist niedrige Ausrüstungskosten und eine hohe Materialausnutzung eine hohe Materialausnutzung und einen hohen Durchsatz auf. Bisher hat die Effizienz des hochmodernen lösungsverarbeiteten CIGSe gerfertigt aus einer Hydrazin-Vorläuferlösung einen Wirkungsgrad von 18,1 % erreicht. Hydrazin ist jedoch ein hochgiftiges Lösungsmittel und sollte nur mit geeigneter Schutzausrüstung gehandhabt werden, um physischen Kontakt mit Dampf oder Flüssigkeit zu verhindern. Aufgrund dieser Probleme ist die Hydrazinlösung für die Massenproduktion nicht vorteilhaft. Die Entwicklung eines ungiftigen Lösungsvorläufers für die Absorberherstellung hat desalb große Aufmerksamkeit auf sich gezogen. Die Herstellungskosten von CIGSSe-Solarzellen können durch die Reduzierung der Absorberdicke weiter verringert werden.

In dieser Arbeit werden lösungsprozessierte submikrometer dicke-Kupfer-Indium-Sulfoselenid (CISSe)- und Kupfer-Indium-Gallium-Sulfoselenid (CIGSSe)-Solarzellen auf Molybdän- (Mo) und Zinn-dotiertem Indiumoxid- (ITO) Rückkontakt mit einer weniger giftigen N,N-Dimethylformamid (DMF)-Lösung hergestellt.

Im ersten Ergebniskapitel dieser Arbeit werden zunächst die Temperbedingungen untersucht, einschließlich Tempern in reinem Selen und einer Atmosphäre aus S und Se (Schwefel und Selen). Mit zunehmendem Selengehalt beim Tempern weisen die entsprechenden CISSe-Geräte bessere PV-Parameter auf. Nach der Schwefeldotierung werden die Leerlaufspannung und der Füllfaktor von CISSe-Solarzellen deutlich verbessert, was zu einer höheren Effizienz führt als beim Tempern in der reinen Selenatmosphäre. Die Leerlaufspannung einer CISSe-Solarzelle mit Ko-Tempern in S und Se kann über 600 mV erreichen, was deutlich höher ist, als in der Literatur angegeben.

Das zweite Ergebniskapitel dieser Dissertation konzentriert sich auf die Verbesserung der PV-Leistung durch Behandlung mit Natriumchlorid (NaCl)-Lösung. Drei Strategien für den Einbau von Na in lösungsverarbeitete CISSe durch Einwirken von wässriger Ethanol-NaCl-Lösung werden untersucht, entweder vor der Absorberabscheidung (pre-deposition treatment, Pre-DT), vor der Selenisierung (pre-selenization treatment, Pre-ST), oder nach der Selenisierung (post-selenization Treatment, PST). Die Pre-ST-CISSe-Solarzellen erreichen

eine bessere PV-Leistung als die aus den beiden anderen Strategien der Na-Einbindung. Zur Optimierung werden Einwirkzeiten (5 min, 10 min und 15 min) und NaCl-Konzentrationen (von 0,2 M bis 1,2 M) des Pre-ST untersucht.

Das dritte Ergebniskapitel in dieser Arbeit behandelt einen CISSe-Absorber hergestellt auf transparentem leitfähigem Oxid (TCO)-Rückkontakt mit Hilfe einer umweltfreundlichen Lösung, der großes Potenzial in der beidseitigen Anwendung zeigt. Ultradünne (ca. 550 nm) CISSe-Solarzellen wurden erfolgreich auf ITO-Rückkontakt durch Rotationsbeschichtung mit einer Metallchlorid-DMF-Lösung mit anschließender Selenisierung abgeschieden. Mit der Erhöhung der Absorberdicke in den Submikrometer (740 nm) zeigen die Solarzellen nicht nur eine höhere Kurzschlussstromdichte, sondern auch einen verbesserten Füllfaktor im Vergleich zu den ultradünnen Bauelementen, was zu einer Effizienzsteigerung führt. Darüber hinaus wurde gezeigt, dass die Behandlung mit NaCl-Lösung vor der Selenisierung die Leistung von CISSe-Solarzellen verbessert.

Im vierten Ergebniskapitel dieser Arbeit kann die durch den Mo-Rückkontakt entstehende parasitäre Absorption in CIGSSe-Solarzellen deutlich reduziert werden, indem dieser durch einen ITO-Rückkontakt ersetzt wird. Üblicherweise bildet sich während des Hochtemperatur-Herstellungsprozesses an der CIGSSe/ITO-Grenzfläche eine unerwünschte GaO_x-Schicht, die eine nachteilige Wirkung auf die Extraktion der photogenerierten Ladungsträger hat. Eine Cu-In-TU-DMF (TU: Thioharnstoff, DMF: N,N-Dimethylformamid) Zwischenschicht zur Modifikation der CIGSSe/ITO-Grenzfläche kann die Rekombination an der hinteren Grenzfläche verrringern. Darüber hinaus werden der Ladungsträgertransport und die Ladungsträgersammlung verbessert, was zu einer erheblichen Verbesserung des Wirkungsgrads führt.

1 Background and motivation

1.1 Potential energy crisis

In past decades, global energy consumption showed a very fast growth owing to rapid economic development. So far, the world energy consumption relies on non-renewable energy, which leads to global pollution expansion through the energy conversion. Fossil fuels, such as oil, natural gas, and coal are non-renewable, therefore, they will run out in the near future and may generate an energy crisis. Fossil fuels are limited and cannot reform in a short period of time. The Paris Agreement, a legally binding international treaty on climate change, entered into force in 2016, which set a goal of the increase in global temperature below 1.5℃ by the end of this century.[1-2] In order to achieve this ambitious goal, greenhouse emission should be significantly reduced. Fossil fuel sources are concentrated in a few countries and most countries need to import them. Therefore, the prices of fossil fuels are susceptible to significant impacts on production and transportation. Unlike fossil fuels, renewable energy sources are essentially inexhaustible and their use generates low or no additional CO_2 emission, leading to the reduction of the greenhouse effect and environmental pollution. Therefore, developing alternative renewable energy and reducing fossil fuel consumption are critical pathways to face the impending energy crisis. In addition, over 135 counties pledged to achieve a long-term target to attain net-zero emissions by 2060.[2] In the past decade, the renewable energies, including solar energy, wind energy, hydropower, and biomass energy, have attracted great attention.

1.2 Global energy demand

Renewable power capacity additions increased 17% in 2021 to reach more than 314 Gigawatt (GW), owing to the record expansion in solar PV and wind power (Figure 1.1). The renewable power capacity additions supported 83% of energy consumption for non-power energy demand (transport, heating, and cooling) and 17% for power demand. The renewable power capacity grew by 314.5 gigawatts (GW), and the total installed renewable power capacity reached 3146 GW. In 2011, electricity generation was provided by 68% of fossil fuels, 20.4% of renewable electricity, and 12% of nuclear power. Compared to 2011, the electricity generation in 2021 significantly increased. The renewable share of electricity generation increased to 28.3% for total electricity generation and the share of fossil fuels to electricity was reduced to 62%. It is the first time by the end of 2021 that more than 10% of the world's electricity was provided by solar and wind power.

1.3 Solar PV

Among the various renewable energy techniques, the ubiquitous availability of solar power makes it one of the most promising candidates. Photovoltaic (PV) technology is a promising long-term clean energy solution because it can convert solar light energy into electricity directly without any other energy addition during the application. The annual solar PV installation capacity additions remain consecutive and show accelerated growth (Figure 1.2a). The annual increment increases from 31 GW in 2011 to 175 GW in 2021, leading to a global solar PV capacity of 942 GW. The top 10 countries contribute 129.2 GW of Solar PV installation capacity additions, which constitutes around 73.8% of the Solar PV installation capacity additions in 2021 (Figure 1.2b).

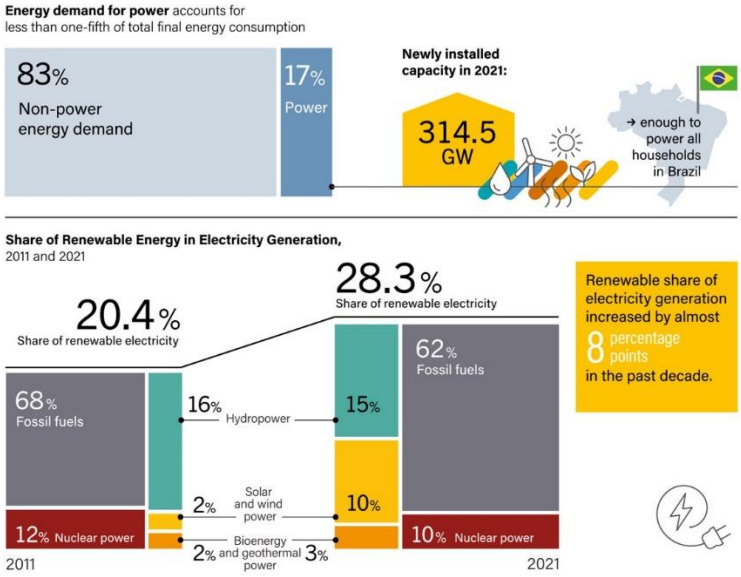

Figure 1.1: Role of renewable energies in electricity generation.[2]

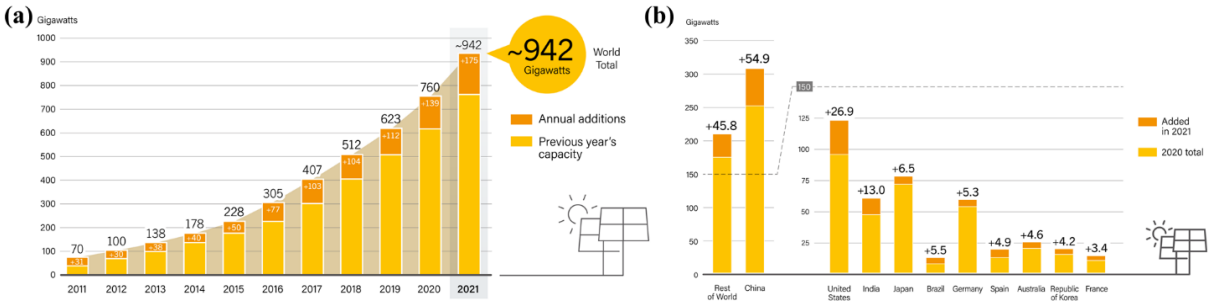

Figure 1.2: (a) Solar PV global capacity and annual addition (2011-2021), (b) Solar capacity and additions to capacity of top 10 countries in 2021.[2]

1.4 Progress of thin film solar cells and modules

Si-wafer-based PV modules are the dominant product of the global PV market. Thin film PV module production occupies a small share of the total global PV market, including cadmium telluride, amorphous silicon (a-Si), and copper indium (gallium) diselenide (CIGSe). In addition, the share of a-Si thin film started to decrease after 2011 (Figure 1.3a).[3] The CdTe thin film module production sharply increased in the past 3 years, whereas the CIGSe thin films module production only showed a slight improvement (Figure 1.3b).

In the current stage, photovoltaic technologies have two main challenges: cost and efficiency. The best thin-film solar cells, including lab-scale cells and modules, are shown in Figure 1.3c. The lab-scale cells' efficiencies are higher than those of the corresponding modules. The efficiencies of Si-based cells and modules are higher than cells and modules of other materials, 26.7% and 24.4% for Si mono-crystalline cells and modules as well as 23.4% and 19.2% for CIGSe cells and modules (Figure 1.3c).[4] Even though the perovskite thin film achieves 23.7 % for the cell, it only reaches 17.9% for the module. However, the long-term stability of the perovskite thin film is the dominant limitation of the application. In the past 40 years, the price of PV modules has continuously decreased (Figure 1.3d).[3]

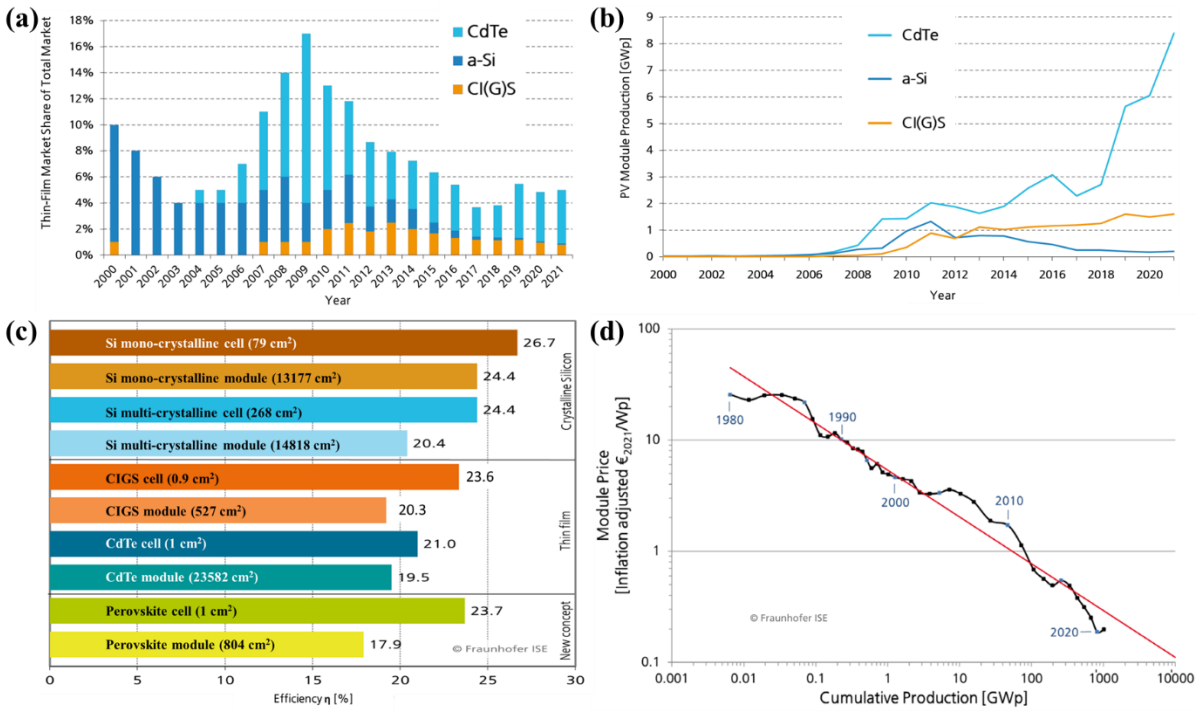

Figure 1.3: (a) Market share of thin-film technologies of total global PV production, (b) annual global PV module production, (c) efficiency comparison of technologies: the best lab cells *vs.* the best lab modules, and (d) the price of commercial PV modules.[3]

So far, the efficiency of CIGSSe solar cells with a standard absorber thickness (2-3 µm) has improved to 23.6%. However, the standard absorber thickness CIGSSe solar cells have a high consumption of scarce elements, leading to a high production price and long payback time.

One of the potential methods to reduce production price is to reduce material consumption via thinning absorber thickness. Reducing the absorber thickness below 1 µm presents an efficiency reduction caused by the apparent drop of short circuit current density (J_{sc}). The J_{sc} reduction originates from the incomplete light absorption of the thin absorber.[5-7] In addition, a serious parasitic absorption of the Mo back contact hinders high J_{sc} achievement. Fabricating a CIGSSe-based absorber on transparent conductive oxide (TCO) back contact joint with light management can effectively mitigate the absorption loss.[5, 8] Furthermore, the CIGSe/TCO solar cells can also be utilized for the bi-facial solar cells, which absorb rear and front illumination.[8] The other strategy for reducing the fabrication cost is developing a cost-effective solution-processed CIGSSe-based absorber.[9]

1.5 Outline of the thesis

The outline of this thesis is as follows: Chapter 2 introduces CIGSe-based thin film solar cells. Chapter 3 describes the characterization technologies. Selenium content affects the CIGSSe absorber quality because it impacts the pressure and formation of $Cu_{2-x}Se$ during the selenization. A high-quality CIGSSe absorber is essential for high efficiency CIGSSe solar cells. In chapter 4 optimum annealing conditions of the precursor films are investigated, including annealing in pure Se (low and high content Se) and Se and S co-annealing (high content of chalcogen). Chapter 5 describes strategies of Na incorporation for solution-processed CISSe solar cells. Simultaneously, the Na content for incorporation is controlled by changing the soaking time of precursor films and the concentration of the NaCl solution. In chapter 6, a semi-transparent CISSe solar cell is achieved by fabricating the CISSe absorber on tin-doped indium oxide (ITO) back contact. Chapter 7 modifies the $Cu(In,Ga)(S,Se)_2$/ITO (CIGSSe/ITO) interface with a thin Cu-In-S-Se interlayer to reduce the back barrier height by hindering the formation of the high-resistivity GaO_x layer at CIGSSe/ITO interface. Finally, a summary and outlook are presented in Chapter 8.

2 Overview of CIGSSe-based thin film solar cells

2.1 CIGSSe-based thin film solar cells

In this chapter, I will introduce the fundamental properties of $Cu(In_x,Ga_{1-x})(Se_y,S_{1-y})_2$ (CIGSSe) thin film solar cells. Our research focuses on the CIGSSe absorbers and the back contact (either ITO or Mo).

In this thesis, all solar cells are measured under the standard Air Mass (AM) 1.5G reference spectrum (defined by American Standards for Testing of Materials (ASTM), Figure 2.1a). Generally, the power and spectrum of the sun light are different owing to different times (day and night as well as summer or winter) and locations. When the solar zenith angle of incident light is 48.19º, the standard solar spectrum at the earth's surface is called AM1.5G (Figure 2.1b), where G represents for global and includes direct and diffuse radiation. The standard AM1.5G has been normalized to 1000 W/m^2 (or 100 mW/cm^2). In our laboratory, this standard AM1.5G illumination light is achieved by using a WACOM sun-simulator containing both a Xenon and a Halogen lamp.

A high-quality CIGSSe absorber plays a crucial role in achieving a high device performance. The device structure of the CIGSSe solar cell is shown in Figure 2.2. Generally, the CIGSSe absorber layer is deposited on a Mo-coated soda lime glass (SLG) or a TCO back contact (such as tin-doped indium oxide, fluorine-doped tin oxide, or aluminum-doped zinc oxide).[10-15] Sodium can diffuse into the absorber from the SLG substrate during the high-temperature fabrication and passivate grain boundary defects.[16-18] In addition, Na promotes the formation of large CIGSSe grains.[19]

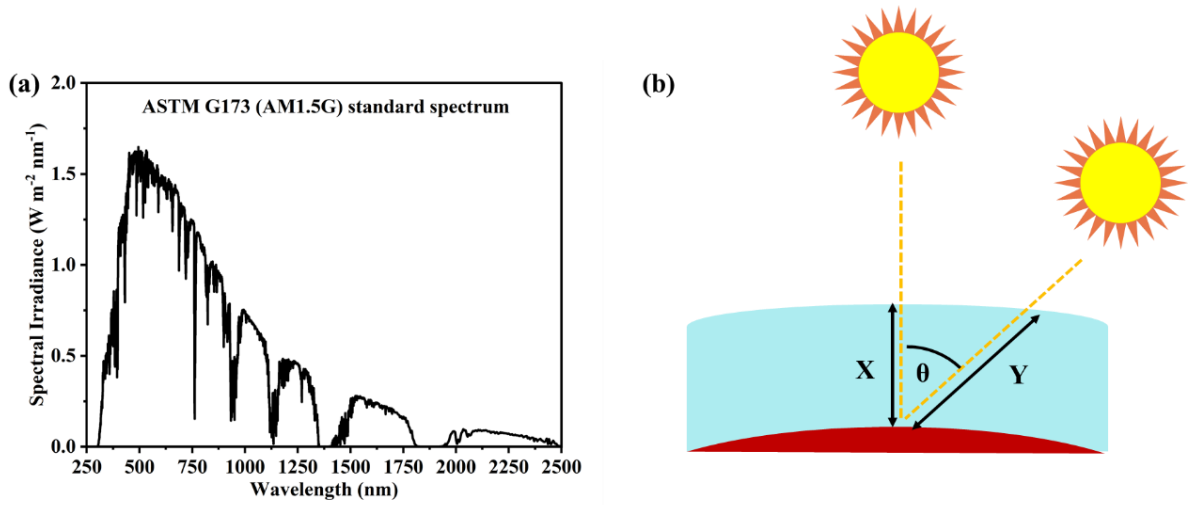

Figure 2.1: (a) Standard AM1.5G solar spectrum, (b) the illustration of air mass calculation. The AM1.5G solar spectrum was reproduced from NREL (rredc.nrel.gov/solar/spectra/am1.5/).

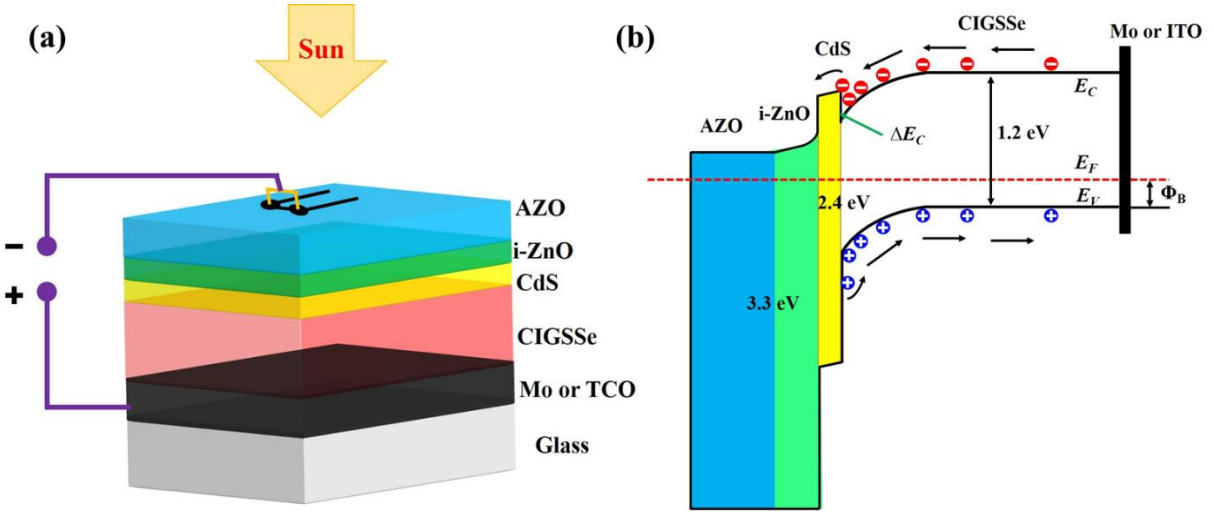

Figure 2.2: (a) Structure of a CIGSe solar cell, (b) the corresponding band diagram of a CIGSe.

When the absorber grows on a Mo back contact, an electrically beneficial thin $MoSe_2$ layer will form at the CIGSSe/Mo interface.[20] An n-type cadmium sulfide (CdS) buffer layer is fabricated on the CIGSSe absorber by a chemical bath deposition process, which can passivate the defects on the CIGSSe surface (such as copper vacancies).[21] The window layer with a double-layer structure, including intrinsic zinc oxide (i-ZnO) and aluminum-doped zinc oxide (AZO), are sputtered atop the CdS buffer layer. In order to form a good connection with the external circuit, a Ni/Al grid is evaporated on top of the window layer.

The band diagram of the CIGSSe device is presented in Figure 2.2b. The photo-generated electrons (red) move toward the CdS direction, whereas the photo-generated holes (blue) migrate toward the back contact. The conduction band (E_C) and valence band (E_V) of the CIGSSe absorber are bent at the front surface to form a space charge region. A spike-like structure is formed at the CdS/CIGSSe interface owing to the conduction band minimum being lower than that of the CdS buffer layer. In general, the CIGSSe devices with a spike-like structure can achieve high PV performance because the carrier recombination can be reduced at the CdS/CIGSSe interface. In addition, a back contact barrier (Φ_B) still exists at the CIGSSe/Mo or CIGSSe/ITO interface.

Figure 2.3 shows the current density-voltage (*J-V*) and external quantum efficiency (EQE) characteristics of high-efficient Si and CIGSSe solar cells. These CIGSSe absorbers for high-efficient solar cells are fabricated from vacuum processing techniques.[15, 22] Indeed, a vacuum deposition process can fabricate a high-quality CIGSSe semiconductor with good compositional control. Si and CIGSSe solar cells present a similar open-circuit voltage, however, the short-circuit current density of Si solar cells is higher than CIGSSe (Figure 2.3a and 2.3c).[4, 22] This higher short-circuit current density can be attributed to high EQE at 300-400 nm of Si solar cells (Figure 2.3b and 2.3d).

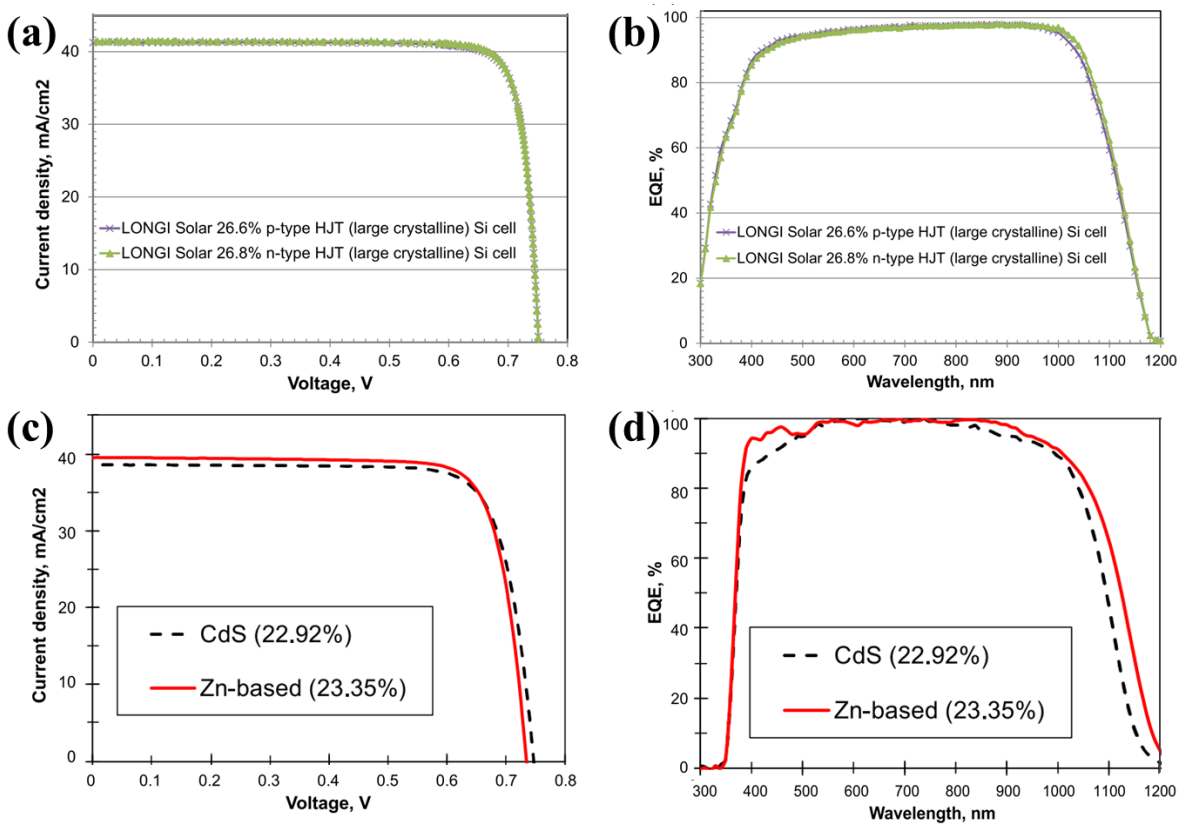

Figure 2.3: Comparison of (a) *J-V* and (b) *EQE* curves of high-efficient Si and CIGSe solar cells. Adapted with permission. Copyright 2018, Wiley-VCH[4] and Copyright © 2019, IEEE [22].

However, vacuum-based processes require high-purity metals, high energy input, and ultrahigh vacuum conditions, resulting in high operational costs. Therefore, developing an alternative cost-effective and large-scale production technique has gained great attention to balance efficiency and fabrication cost.

2.2 Alternative solution process

In the past decades, a solution process has been applied for thin film fabrication in ambient conditions, reducing the energy consumption and the cost for the ultrahigh vacuum equipment.[9, 23-26] Therefore, solution-processed fabrication can reduce the cost of the ultrahigh vacuum equipment and increase the manufacturing throughput. In addition, the solution-processed precursor film can be deposited from various precursors, including metal salts, metal oxides, and metal chalcogens, which does not require high-purity metals (over 99.999%).[9, 24, 27-28] Therefore, solution processing is a promising strategy for semiconductor fabrication.[23, 25-26]

Figure 2.4 shows the evolution of record efficiencies of lab-scale CIGSSe solar cells from molecular-based routes and the vacuum-based strategy. Several molecular solutions have been utilized for CIGSSe solar cells fabrication in the past decades. The highest efficiency (18.1%) of solution-processed CIGSe solar cells is fabricated from a hydrazine molecular solution.[29] However, hydrazine is a highly toxic solvent, and the human body should be protected by using appropriate protective equipment to prevent physical contact with either vapor or liquid. Owing to this shortcoming of hydrazine, the hydrazine solution is not beneficial for mass production. Thus, developing alternative solvents for CIGSSe fabrication has received great attention.

For the last decade, an inexpensive, safe, and nontoxic alcohol-based precursor solution has been utilized for CIGSSe solar cells fabrication.[9, 30-31] However, the CIGSSe absorber exhibits a multilayer morphology, i.e., a fine-grained and porous carbon-rich bottom layer.[30-31] This porous bottom layer deteriorates the electronic performance of the solar cell by increasing the series resistance, inhibiting grain growth, creating new recombination centers, and causing poor back contact adhesion.[30-32] The efficiency of alcohol-based CIGSSe solar cells has reached 14.4%.[30] However, a carbon residual layer is observed at the CIGSSe/Mo interface and the open circuit voltage deficit ($V_{oc,def}$) is large.

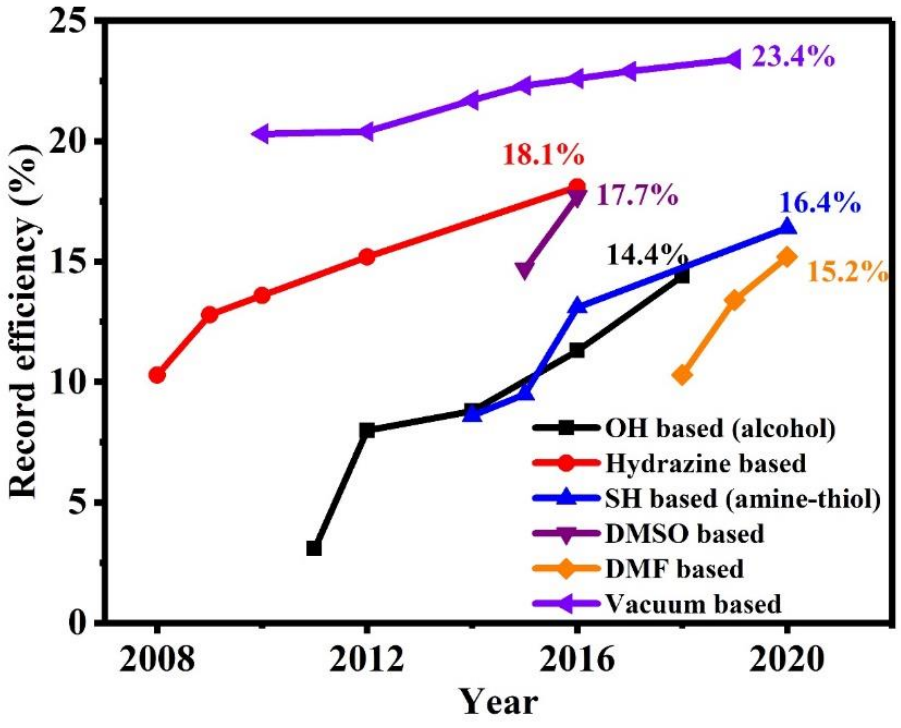

Figure 2.4: Evolution of record efficiency of lab-scale $Cu(In,Ga)(S,Se)_2$ solar cells from molecular-based routes and the record efficiency for vacuum-based solar cells.[9] Redrawn with permission from Wiley-VCH.

Alternative SH-based (amine-thiol) solvents have been applied for CIGSSe solar cells fabrication.[24, 27] The SH-based solvent can dissolve various metal reactants to form a stable molecular solution, including pure metals, metal salts, metal oxides, metal chalcogenides, and elemental chalcogens.[24, 27-28] The record efficiency of SH-based CIGSSe solar cells has achieved 16.4% by designing a copper-poor ordered vacancy compound (OVC) layer on the front surface of the absorber.[33] However, thiol and amine group solvents are still highly toxic. Simultaneously, the amine-thiol mixtures are inherently malodorous and will generate H_2S gas during the wet precursor film annealing on the hot plate.[27] The fabrication process of the CIGSSe absorber should be implemented in a glove box.

Additionally, the dimethyl sulfoxide (DMSO) solvent has been applied for CIGSSe solar cells fabrication. CIGSSe with 17.7% efficiency is reported by Solar Frontier, which is fabricated from metal chalcogenide molecular inks.[34] However, the low solubility of In^{3+} is a limitation for the application of DMSO molecular ink. The solubility of $In(DMSO)Cl_3$ is only 0.1 M at room temperature and 0.5 M at 120℃.[35] To fabricate a high-quality precursor film, the precursor ink should remain at a high temperature during the spin-coating process.

In contrast to the DMSO-based ink, the $InCl_3$ can be dissolved in dimethylformamide thiourea (DMF-TU) solution to form a stable molecular ink (0.65 M at room temperature and up to 1.8 M at 120℃ heating).[36-37] In addition, the DMF-TU solution can also dissolve Cu(II), Zn(II), Ge(IV), Ag(I), and Cu(I) very well, which can be utilized for kesterite and chalcopyrite absorber fabrication.[38] The DMF molecular solution has been applied to fabricate the CIGSSe absorber via a spin-coating process, and the corresponding solar cell efficiency has achieved 15.2%.[36] Furthermore, a densely packed large grain CIGSe without a layer of fine grains was obtained by using this DMF molecular solution. In addition, over 12% efficient CIGSSe solar cells can also be fabricated by doctor-blading, indicating that the DMF-TU molecular ink is a promising CISSe solar cell fabrication strategy.[39] Thus, we will use the DMF-TU molecular solution for our experiments in this thesis.

2.3 Submicron CISSe solar cells

Generally, high-efficiency CIGSSe solar cells utilize a 2-3 μm thick absorber for light absorption. However, the thick absorber increases the starting materials' budget due to high materials consumption. When the absorber is fabricated by the solution process, the thick absorber requires more cycles of spin-coating and annealing. In addition, the thick absorber hinders solvent evaporation and leads to a fine-grained bottom layer.[31] Thinning the absorber thickness can reduce the material consumption and shorten the duration of precursor film fabrication. Simultaneously, the thin absorber benefits from Se through-diffusion during the selenization process. In the past decades, a 15.2% efficient ultra-thin CIGSe solar cell (490 nm) has been achieved via the co-evaporation fabrication process (Figure 2.5a).[40]

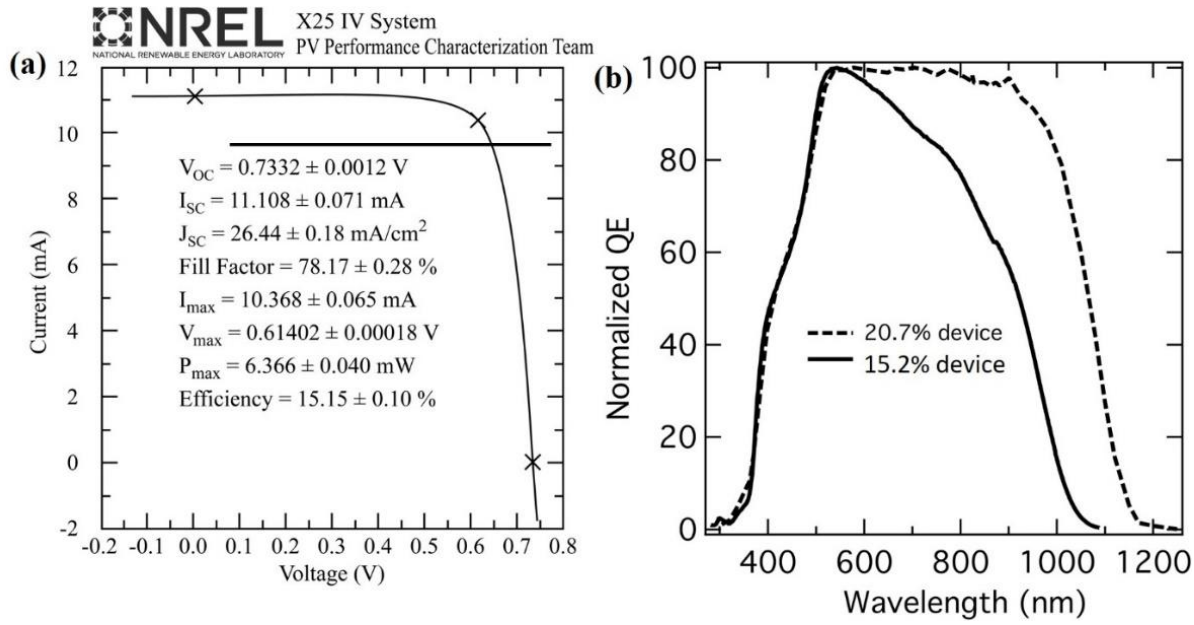

Figure 2.5: (a) *J-V* curve champion efficiency of ultra-thin CIGSe solar cell, and (b) comparison of external quantum efficiency spectrum between the standard-thickness CIGSSe device and the champion efficiency of ultra-thin CIGSe device. Adapted with permission. Copyright 2018, Wiley-VCH.[40]

However, reducing the absorber thickness below 1 μm will result in serious light absorption loss (incomplete absorption of the illumination light by the CIGSSe absorber, Figure 2.5b) and severe rear interface recombination, leading to a low short circuit current density (J_{sc}).[5-6, 13] Compared to the ultra-thin CIGSSe solar cells, submicron CIGSSe solar cells can increase the J_{sc} because of a thicker absorber.[41-42] When the CIGSSe absorber is deposited on a TCO back contact, the light not absorbed can be reflected into the absorber by a rear-reflector structure or a mirror underneath the substrate.[43-45] Furthermore, the CIGSSe/TCO solar cells (without the back reflector) can be utilized for bifacial applications.[8, 13, 46]

So far, there is still rare research on fabricating ultra-thin and submicron CIGSSe absorbers on TCO back contact via the solution process, especially solution-processed CIGSSe/TCO structure solar cells.

2.4 Sulfur doping for CIGSSe solar cells

The Cu-In-Ga stack or the solution-processed precursor film has to be subject to a selenization process. The Cu will react with Se to form a $Cu_{2-x}Se$ liquid phase at the beginning of the high-temperature selenization process. This $Cu_{2-x}Se$ liquid phase can be used as a precursor for forming large-grained CIGSSe and assisting the migration of elements. CIGSe performance can be further improved by H_2S gas for post-sulfurization (Figure 2.6a).[47]

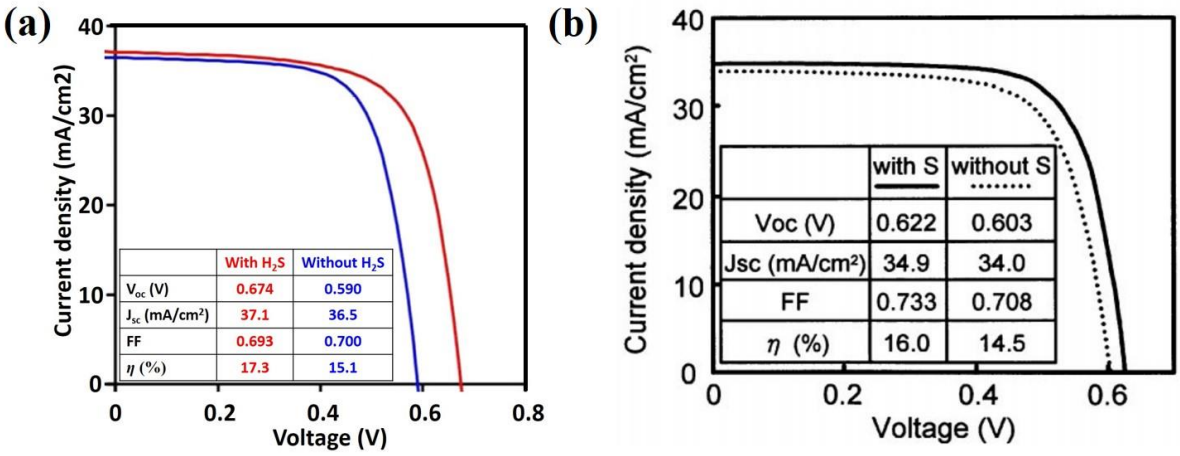

Figure 2.6: Performance improvement by post-sulfurization (a) in H_2S gas, Adapted with permission. Copyright © 2001 Elsevier Science B.V.[48] (b) in S vapor atmospheres, Adapted with permission. Copyright 2014, Wiley-VCH.[40]

Theoretically, the S-doped CIGSSe absorber has a wider band gap, and then the open-circuit voltage (V_{oc}) of the CIGSSe solar cells is improved when CIGSe and CIGSSe have similar absorber quality. After the H_2S post-sulfurization treatment, the absorber surface has a higher S concentration than the bulk of the absorber.[30] In addition, S incorporation will passivate the absorber's surface, leading to an improvement of the p-n heterojunction quality.[30, 49] However, S will aggregate at grain boundaries of the CIGSSe absorber after the H_2S post-sulfurization treatment, resulting in high charge carrier recombination at grain boundaries.[49] H_2S is a highly toxic gas, which will increase the budget for waste gas treatment equipment in the large-scale production of the CIGSSe module. Alternatively, S powder can be utilized for post-sulfurization. Compared to the CIGSe solar cells, all PV parameters of CIGSSe solar cells are improved by post-sulfurization in S vapor (Figure 2.6b).[48] These improvements are attributable to the passivation of trap states by S.

In the past few years, S incorporation was also achieved by a solution-processed surface sulfurization. The CIGSe absorber is soaked in ammonium sulfide solution $(NH_4)_2S$ and then annealed at 300°C for 2 min in a Se atmosphere (Figure 2.7a).[50] Alternatively, a spin-coating process is also utilized for surface sulfurization. The TA-DMF (Thioacetamide-Dimethylformamid) solution is deposited on the surface of the CIGSe absorber and then annealed in a glovebox at 300°C for 2 min (Figure 2.7b).[51] After the incorporation of sulfur, V_{oc}, FF, and efficiency of the CIGSSe device are obviously increased compared to the reference CIGSe device.

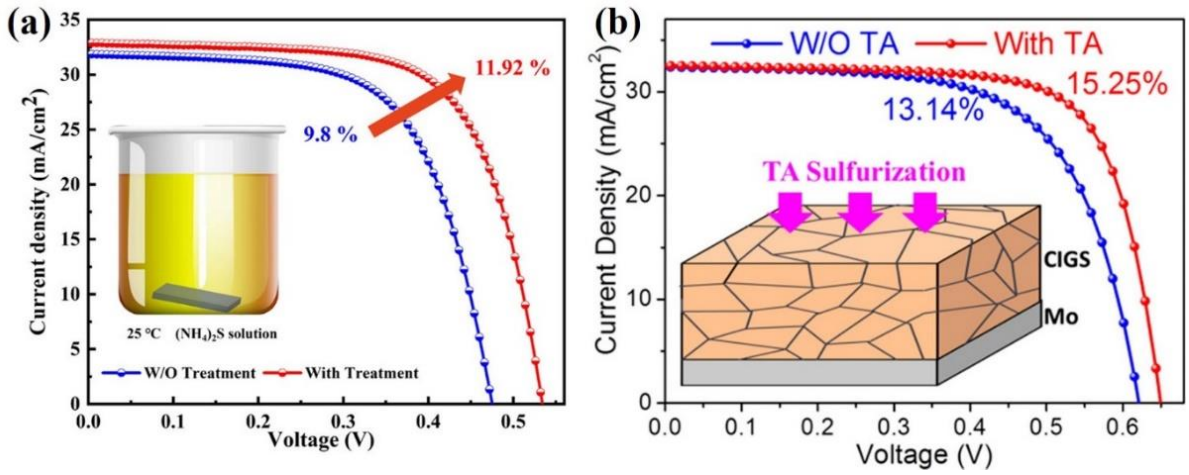

Figure 2.7: Options for surface sulfurization via a solution process. (a) CIGSe absorber soaking in $(NH_4)_2S$ solution.[50] Adapted with permission.[50] Copyright © 2020, American Chemical Society. (b) spin-coating TA-DMF solution on the surface of the CIGSe absorber.[51] Adapted with permission.[51] Copyright © 2021, American Chemical Society.

In the past decades, the CIGSSe absorbers have been fabricated by simultaneous selenization and sulfurization.[52-54] Unlike the H_2S post-sulfurization treatment and solution-processed surface sulfurization, simultaneous selenization and sulfurization with Se and S powders can shorten the annealing duration. However, the S content should be controlled, and the crystallinity of the absorber will be worse by annealing in a high ratio of S/(S+Se) atmosphere.[53-54]

2.5 NaCl treatment

Na plays a crucial role in improving photovoltaic (PV) performance.[16, 18, 21, 55] When the CIGSe is fabricated on soda lime glass (SLG, containing sodium), the crystallinity of the absorber and PV performance of the corresponding solar cell are better than when fabricated on a borosilicate glass substrate (Na-free).[16] This phenomenon can be attributed to the increase in V_{oc} and *FF*, resulting in improved efficiency. A general understanding is that the alkali element doping can passivate defects at the surface and grain boundaries of the p-type CIGSe absorber.[56] However, alkali doping does not change the donor concentration but decreases the compensating acceptor concentration.[16] Since the free carrier concentration is defined by the difference in donor and acceptor concentration, the CIGSe with the alkali doping will increase the p-type carrier concentration.

Na catalyzes the formation of Mo-Se and Cu-In-Se layers at the rear and front interface of the CIGSe absorber.[57] These layers are beneficial for separating and transporting photogenerated carriers, Mo-Se for the holes and Cu-In-Se for the electrons. In other words,

Na doping can reduce the recombination in CIGSe solar cells. The Na-treated absorber presents a Cu-poor surface and the Cu vacancies (V_{Cu}) are occupied by Na atoms to form Na_{Cu} defects. The Na_{Cu} defects can be converted to Cd_{Cu} donor defects after the CdS chemical bath deposition, leading to the formation of a good buried homojunction at the CdS/CIGSe interface.[21]

No matter if Na is from the SLG substrate or introduced by other methods, the PV performance will be improved when the Na atom density is lower than 10^{15} cm^{-3}.[16] However, when the Na concentration is higher than 1 at.% (atomic percentage), the device performance will become inferior. A high concentration of Na will induce the degradation of CIGSe grains, leading to a worse morphology of the CIGSe absorbers.[55-56, 58] The most common path for sodium incorporation in the co-evaporation process is the post-deposition treatment (PDT), i.e. deposition of a thin layer of NaF after the CIGSSe absorber growth.[7, 44] Compared to absorber fabrication by co-evaporation, Na atoms can be introduced at different steps of CIGSSe growth from the precursor solution.[56, 58] For example, Na ions can be added into the precursor solution, prior to the precursor deposition, before or after selenization. Compared to NaF, NaCl offers low cost, benign nature, and good solubility in water.[56, 59] The typical strategy for sodium incorporation into solution-processed CIGSSe solar cells is to soak the precursor thin films in NaCl solution.[60]

Figure 2.8 shows the results of the CIGSSe solar cells via a solution-processed sodium incorporation. The copper indium gallium sulfide (CIGS) nanocrystal films are soaked in a 1 M NaCl (1 molarity NaCl) solution for 10 min before selenization.[60] The reference CIGSSe absorber exhibits a typical morphology of solution-processed CIGSSe, which contains small size grains and a rough surface (Figure 2.8a). For the NaCl-treated CIGSSe absorber, a significant improvement in the morphology is observed (Figure 2.8b).

Large, micron-sized and densely packed grains are obtained with the NaCl pre-selenization treatment. Additionally, the surface of the NaCl-treated CIGSSe is smoother than the one of CIGSSe without NaCl treatment. The NaCl-treated CIGSSe device shows a remarkable improvement in PV performance (Figure 2.8c).

The NaCl concentration for soaking affects the Na content in the selenized CIGSSe absorber, which impacts the PV performance.[56-57] With increasing the NaCl content, the surface morphologies of CIGSSe absorbers first improves and then deteriorates, which can be attributed to the excess Cl^- ion (from NaCl).[56, 61] The deteriorative morphology of CIGSSe results in inferior PV performance.

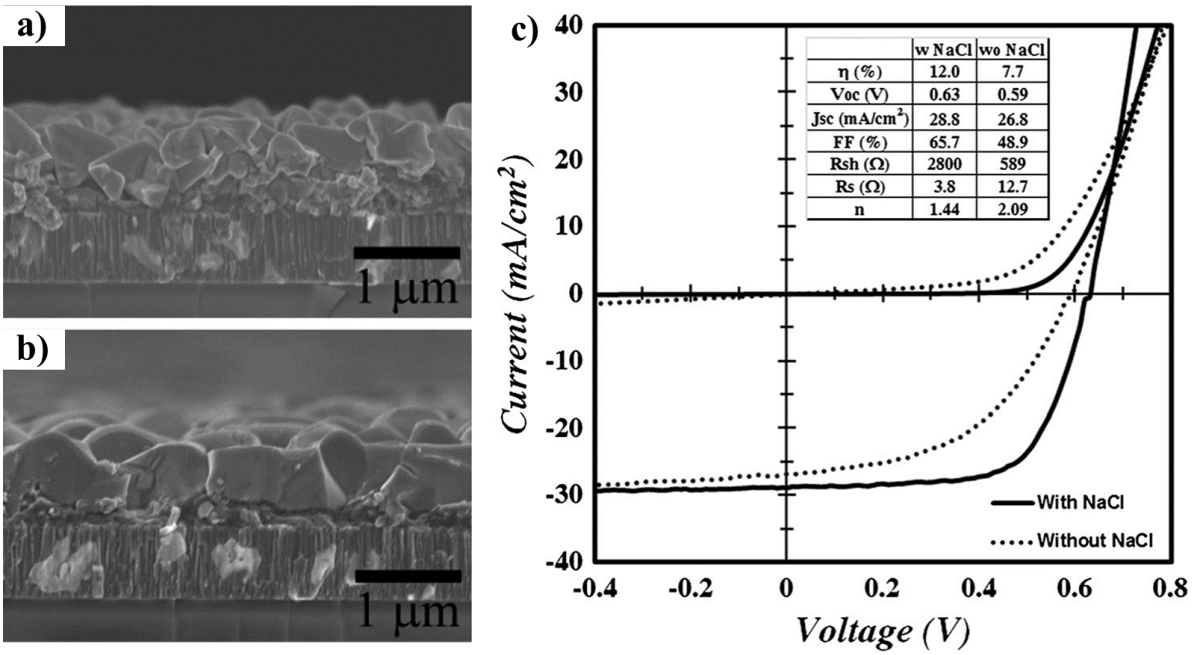

Figure 2.8: Cross-sectional SEM images of CIGSe film (a) without NaCl treatment and (b) with NaCl treatment by soaking the precursor films in NaCl solution. (c) Photovoltaic parameters of *J-V* characteristics of the resulting CIGSSe thin film solar cells with and without NaCl treatment.[60] Adapted with permission.[60] Copyright 2018, Wiley-VCH.

2.6 CISSe solar cells on transparent conductive oxide back contact

The traditional CIGSe solar cell is deposited on an opaque Mo back contact. The efficiency of solar cells on Mo back contact increased slowly in the past decade, and the J_{sc} has achieved 89% of the short circuit current density of the Shockley-Queisser limit (J_{sc}^{SQ}).[62] The CIGSe solar cell with a 1.08 eV band gap absorber shows 39.6 mA/cm^2, and the J_{sc}^{SQ} is 44.6 mA/cm^2.[15, 63] It is difficult to further improve the efficiency of CIGSe solar cells by increasing J_{sc}. Compared to the opaque Mo back contact, the transparent conductive oxide (TCO) back contact can be applied not only for the fabrication of tandem devices but also for a bifacial configuration of solar cells.[8, 46, 55, 64]

The TCO back contact should avoid decomposition and unfavorable reactions with the CIGSe absorber during the high-temperature growth.[65] In addition, the outstanding conductivity and transmission properties should be retained in the final device. So far, several n-type TCO back contacts are utilized for CIGSe solar cell research, including fluorine-doped tin oxide (FTO), tin-doped indium oxide (ITO), hydrogen-doped indium oxide (IOH), and aluminum-doped zinc oxide (AZO).[46, 65-66] Compared to the CIGSe/Mo device, a pronounced reduction of the *FF* is observed for the CIGSe/TCO device.[67] This phenomenon originates from two possible reasons: 1. The increase in sheet resistance of the TCO back contact after high-temperature absorber fabrication, leading to a high series resistance of the CIGSe device.[65] 2.

A high extraction barrier for holes at the CIGSe/TCO interface because of Schottky contact formation due to a highly resistive GaO_x layer.[67] Ga will accumulate at the rear interface of the CIGSe absorber owing to inter-diffusion between In (towards the front surface of the absorber) and Ga (towards the rear interface of the absorber).[68] To solve extraction issues of photogenerated holes, Mo, MoO_3, Au, or Ag thin interlayers are inserted between CIGSe and TCO. Thus, the CIGSe/TCO interface is changed from a Schottky contact to an Ohmic-like contact.[21, 69-71]

The highest efficient CIGSSe/TCO solar cell was fabricated by depositing a 15 nm Ag layer on the ITO back contact before CIGSe absorber co-evaporation. Additionally, sodium fluoride (NaF) and rubidium fluoride (RbF) post-deposition treatment techniques were applied to improve the absorber quality (Figure 2.9).[8] When the CIGSe absorber was deposited on the SLG (with a SiO_x barrier for Na) substrate, the bifacial CIGSe device presented 19.77% efficiency for front illumination and 10.89% for illumination from the rear side. The efficiency of flexible bifacial CIGSe devices shows 15.36% and 6.61% efficiencies under the front and rear illumination.

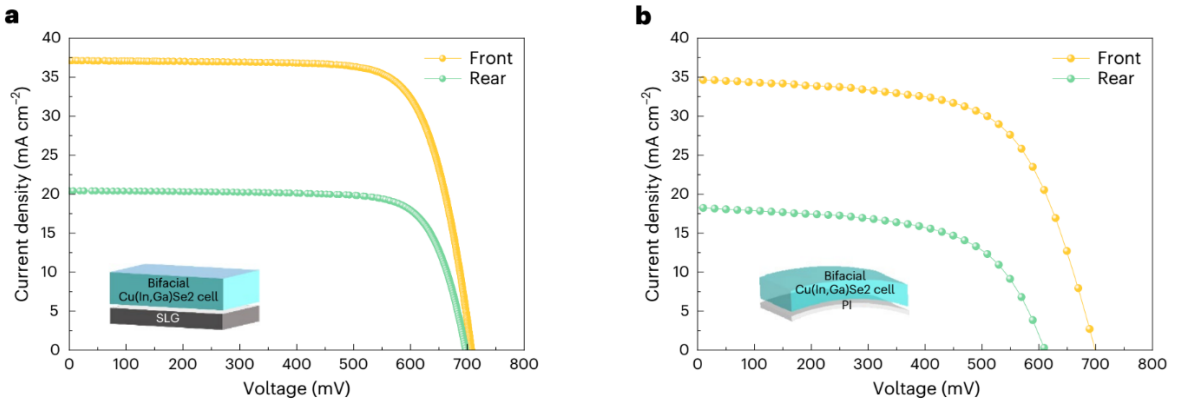

Illumination	V_{OC} (mV)	J_{SC} (mA cm^{-2})	FF (%)	PCE (%)
Front	707.85	37.13	75.23	19.77
Rear	697.67	20.41	76.46	10.89

Illumination	V_{OC} (mV)	J_{SC} (mA cm^{-2})	FF (%)	PCE (%)
Front	699.60	34.65	63.34	15.36
Rear	611.35	18.22	59.37	6.61

Figure 2.9: The champion efficiency CIGSe/TCO solar cell deposited on (a) soda lime glass (SLG) substrate and (b) polyimide substrate. Adapted with permission. Copyright 2022, Springer Nature.[8]

3 Characterization methods

3.1 X-ray diffraction measurement

The by-product compounds will strongly impact the performance of chalcopyrite solar cells, such as the $Cu_{2-x}Se$. Therefore, fabricating a high-quality absorber is crucial to achieve high power conversion efficiency. X-ray diffraction (XRD) can be applied to analyze the structural properties of crystals, crystalline quality, as well as to distinguish between crystal phases of the same chemical species. When the incident X-ray strikes a crystal, scattering will take place determined by Bragg's law:

$$2d \sin\theta = n\lambda \tag{3.1}$$

where d is the spacing between the lattice planes, θ the incident angle, n any integer, and λ the wavelength of the incident beam. Regarding thin film samples, grazing incidence X-ray diffraction (GIXRD) analyses is used to identify the crystalline structure, lattice parameters, and physical properties. In this work, GIXRD with an incidence angle of 0.5 ° is applied to measure the structure of the as-prepared films. The data is collected employing an X'Pert PRO diffractometer (PANalytical) with Ni-filtered Cu Kα radiation and a PIXcel detector.

3.2 Raman Spectroscopy

Vibrational and rotational modes of atoms or groups of atoms in materials can be analyzed using Raman spectroscopy. This technique relies on the inelastic scattering between incident photons and the vibrational states in materials (Figure 3.1). Raman shift values are calculated by the following formula:

$$\Delta\nu = \nu_0 - \nu_1 \tag{3.2}$$

where $\Delta\nu$ is the Raman shift, ν_0 the excitation frequency, and ν_1 the scattering frequency. Our research employs a home-built system by Femtika with an excitation laser of a wavelength 532 nm for measuring Raman spectroscopy.

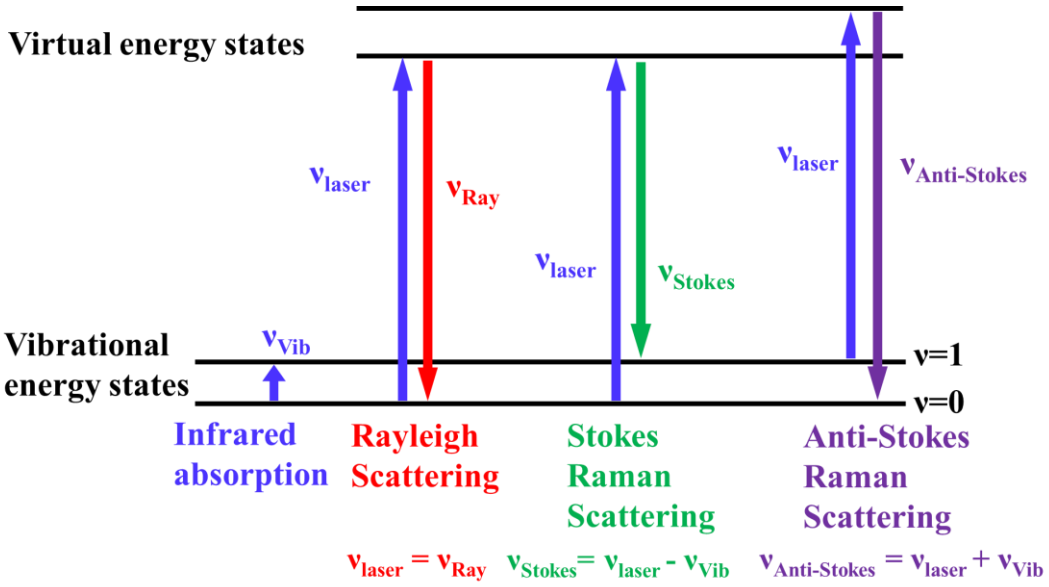

Figure 3.1: Energy-level diagram of the elastic scattering and inelastic scatterin of incident photons.

3.3 X-ray fluorescence and glow discharges optical emission spectroscopy

The composition of the absorber is measured by the X-ray fluorescence (XRF) technique, a non-destructive analytical technique for elemental composition analysis. When a primary X-ray beam irradiates the sample, the characteristic fluorescent X-ray photons specific to each of the elements are excited if the primary beam energy is above the characteristic X-ray energy. The characteristic fluorescent X-rays can be applied to determine the elements contained in the sample qualitavely and quantitavely. In our group, compositions of the CISSe absorbers are measured by a calibrated ED-XRF (Energy dispersive X-ray fluorescence) instrument of type SPECTRO XEPOS.

Glow discharge optical emission spectroscopy (GDOES) using a Spectruma GDA 650 HR analyzer is applied for qualitative and quantitative analysis of thin film materials. In addition, GDOES can also investigate the depth profiles of the distribution of the elemental compositions. However, unlike the XRF measurement, the GDOES measurement will destroy the sample. The sample's surface is ablated plane-parallelly during the GDOES measurement.

3.4 Scanning electron microscopy (SEM)

Scanning electron microscopy (SEM) technique is utilized for the morphology characterization of CISSe and CIGSSe devices in our research. When the focused electron

beam interacts with the surface of the sample, various signals of the interactions between electrons and matter are detected. Backscattered electrons and secondary electrons can be observed and used to generate SEM images. The contrast in a backscattered electron image reveals the compositional difference in a specimen (difference in the average atomic number). However, the spatial resolution of the backscattered electron image is low in comparison with that of the secondary electron image because the backscattering electrons are emitted by elastic scattering of the incident electrons. However, the secondary electrons are emitted from a few nanometers of the sample surface owing to the low energy of these secondary electrons (the order of 50 eV). Therefore, the secondary electron signals are very sensitive to the surface structure and provide surface topographic information. A JEOL JSM-7500F SEM equipment is employed for morphology observation in this thesis.

3.5 UV-Vis-NIR photospectrometry

A LAMBDA 1050+ UV/Vis/NIR Spectrophotometer from Perkin Elmer is used to measure optical transmission and reflection. The measured wavelength ranges from 250 nm to 2500 nm because the light sources and detectors of the instrument cover the ultraviolet-visible-near-infrared range. This measurement system can rapidly collect the results without the reduction in data quality due to its high sensitivity. We use this equipment to measure the optical properties of the thin film.

3.6 Current density-voltage characteristics

Figure 3.2 shows the typical light and dark *J-V* characterization results for a CISSe solar cell. The illuminated *J-V* curve is obtained for the standard conditions (AM1.5G corresponding to 100 mW/cm^2; 25°C) under a sun-simulator system, which is utilized to identify the power conversion efficiency of a solar cell. We can directly extract V_{oc} and J_{sc} from the *J-V* curve under illumination, and then we can calculate the *FF* and efficiency.

The short-circuit current density J_{sc} is the photocurrent density of the solar cell, which can be extracted from the illumination *J-V* curve at $V = 0$ V. The short circuit current (I_{sc}) is divided by the area to express the J_{sc}, and the unit of the J_{sc} is mA/cm^2. It is the maximum current density that can be achieved in a solar cell. The J_{sc} shall be equal to the photocurrent density (J_{ph}) in an ideal solar cell. However, the J_{sc} is smaller than the J_{ph} in a practical solar cell. The J_{sc} loss originates from recombinations (radiative recombination and non-radiative recombination), incomplete charge collection, and optical losses (including reflection of the illumination light, parasitic light absorption, and transmission through the back contact).

The open-circuit voltage V_{oc} is the maximum voltage obtained from the illuminated *J-V* curve when J_{sc} is 0. Theoretically, V_{oc} improvement can be achieved in the CISe absorber by S doping or Ga doping when the CISSe and CIGSe absorbers have similar crystallinity to the CISe absorber. However, in practice, non-radiative recombination is the main limitation of high V_{oc} achievement.

The fill factor *FF* is the ratio of maximum power delivered by the device to the product of J_{sc} and V_{oc} (Figure 3.2). In practice, the *FF* is affected by series resistance, shunt resistance, recombination loss, and collection loss.

Efficiency η is calculated from the obtained V_{oc}, J_{sc}, and *FF*:

$$\eta = \frac{P_{max}}{P_{in}} = \frac{V_{mpp}J_{mpp}}{P_{in}} = \frac{V_{oc}\times J_{sc}\times FF}{P_{in}} \tag{3.3}$$

where P_{max} is the maximum generated power of the solar cell, P_{in} the incident power (from the light source), V_{mpp} and J_{mpp} the voltage and current density at the maximum power point, respectively. A single-diode equivalent circuit model is commonly used to analyze the p-n junction solar cells (Figure 3.3).[72] An outstanding p-n junction solar cell has a small series resistance (R_s) and a large shunt resistance (R_{sh}).[72-73] A general single exponential diode equation can describe the *J-V* behavior of a thin film solar cell:[72]

$$J(V) = J_0 exp\left[\frac{q}{AkT}(V - JR_s)\right] + G_{sh}V - J_{ph} \tag{3.4}$$

where q is the elementary charge, k Boltzmann's constant, T temperature, J_0 diode current density, A the diode quality factor, G_{sh} conductance ($1/R_{sh}$), J_{ph} the light-generated current density ($\approx J_{sc}$).

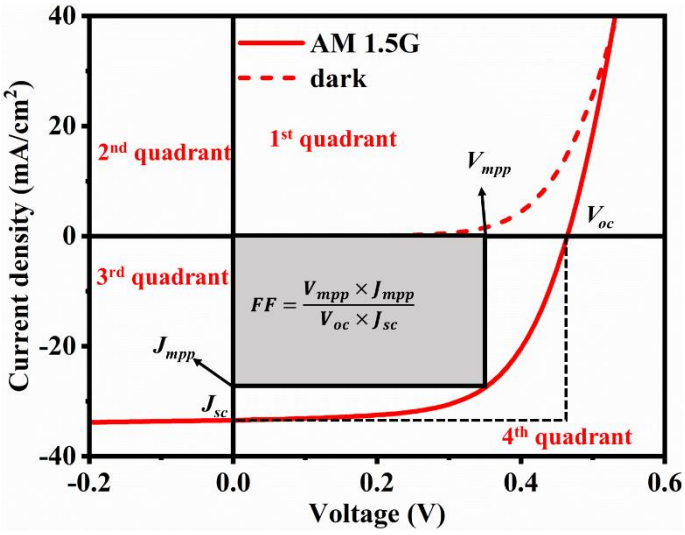

Figure 3.2: A typical *J-V* characterization result of CISSe solar cell under illumination and dark conditions.

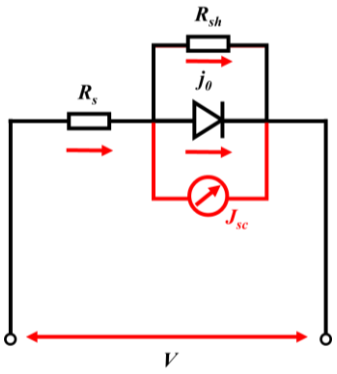

Figure 3.3: Structure of CISSe solar cells for *J-V* measurement and its equivalent circuit.

The *J-V* curves of CISSe solar cells are collected under the standard illuminating condition (AM1.5G; 100 mW/cm^2; 25℃) and dark condition (Figure 3.4a). To extract the electrical parameters of the CISSe solar cell, the *J-V* curves should provide sufficient data in the first and third quadrants.

The shunt conductance G_{sh} can be extracted from equation 3.4 by fitting the plot of the derivative *dJ/dV* against *V* across the reverse bias region. In the reverse bias region, $J_0 exp\left[\frac{q}{AkT}(V - JR_s)\right]$ approaches 0, the plot of *dJ/dV vs. V* will become flat (dark condition) or fit by *dJ/dV* as a constant linear fitting (light condition) (Figure 3.4b). Therefore, the value in reverse bias will equal G_{sh}. Some noise of the plot of *dJ/dV vs. V* may come from calculating the derivative, especially the plot extracted from illumination *J-V* data. R_{sh} can be obtained from the reciprocal of G_{sh}.

The derivative *dV/dJ vs.* $(J+J_{sc}-G_{sh}V)^{-1}$ is utilized for the calculation of R_s and *A*. The resultant equation will be:[72]

$$\frac{dV}{dJ} = R_s + \frac{AkT}{q}(J + J_L - G_{sh}V)^{-1} \tag{3.5}$$

When J_L is independent of the voltage ($J_L = J_{sc}$), R_s can be obtained from the intercept of *dV/dJ vs.* $(J+J_L-G_{sh}V)^{-1}$ linear fitting and *A* can be calculated from the slope of this fit (Figure 3.4c). When the dark *J-V* curve is utilized for analysis, it follows that $J_{sc} = J_L = 0$.[72]

$$\ln(J + J_L - G_{sh}V) = \ln J_0 + \frac{q}{AkT}(V - R_s J) \tag{3.6}$$

A semi-logarithmic plot of the $(J+J_{sc}-G_{sh}V)$ *vs.* $(V-R_sJ)$ plot is applied to calculate J_0 and *A*. From equation 3.6, we can get their relationship from the *J-V* curves (Figure 3.4d). The intercept of this plot gives J_0 and the slope q/AkT of this plot yields *A*. However, when equation 3.6 is used for calculation of *A*, the G_{sh} and R_s are used as parameters for calculation, leading to a large mismatch to the real values. Therefore, in this thesis, we calculate the values of *A* by using equation 3.5.

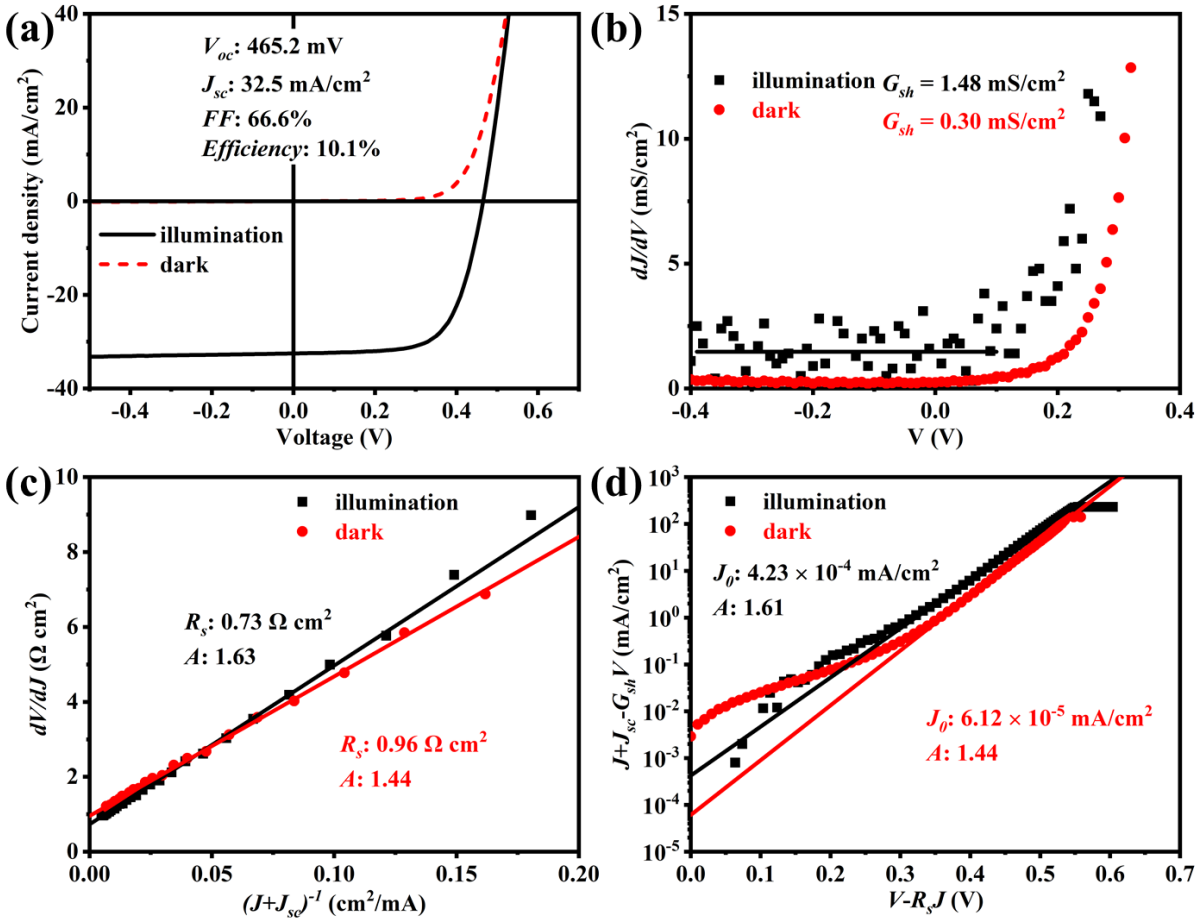

Figure 3.4: Light and dark *J-V* characteristics of a $CuIn(S,Se)_2$ solar cell: (a) Standard *J-V* curves; Plots of (b) G_{sh} *vs. V*, (c) *dV/dJ vs.* $1/(J+J_{sc}-V/R_{sh})$ for derivation of R_s and *A*, and (d) semi-logarithmic plot of $J+J_{sc}-G_{sh}V$ *vs.* $V-JR_s$ to determine *A* and J_0.

3.7 Temperature dependent current density-voltage measurement

Bulk recombination and interface recombination limit the efficiency improvement of CIGSSe-based solar cells. Understanding the dominant recombination mechanism in CIGSSe-based solar cells can guide us to optimize the fabrication conditions for efficiency improvement, such as improving the absorber growth condition or buffer layer materials selection as well as optimizing the buffer layer thickness. Therefore, it is important to identify the dominant recombination mechanism in CIGSSe-based solar cells.

Temperature-dependent current density voltage (*JVT*) measurements are used to identify the dominant recombination path of thin film solar cells. The V_{oc} can be extracted from the temperature-dependent *JV* measurement under one-sun illumination. To identify the dominant recombination path in CIGSSe-based solar cells, the V_{oc} values are plotted as a function of temperature. The relationship between V_{oc} and temperature follows the formula:[43, 55]

$$qV_{oc} = E_a - AkT \ln\left(\frac{J_{00}}{J_{sc}}\right) \quad (3.7)$$

where E_a is the activation energy, A is the diode ideality factor, k the Boltzmann constant, J_{00} the reverse saturation current density, and J_{sc} the short circuit current density. The activation energy can be extracted from the *JVT* profile by linear extrapolation of V_{oc} to $T = 0$ K (Figure 3.5). When the activation energy is very close to the band gap of the absorber, the dominant recombination occurs in the bulk of the absorber. However, if the activation energy is significantly lower than the band gap of the absorber, the dominant recombination will occur at interfaces.

The interface recombination includes the absorber/buffer layer interface and the back contact interface. The ideality factor reflects the severity of the recombination at the front surface (depletion region).[72, 74] The ideality factor of the solution-processed CIGSSe solar cell is close to 2. A large ideality factor value indicates that the recombination at the depletion region increases. An Ohmic-type contact can be formed by a thin $MoSe_2$ interlayer at the CIGSSe/Mo interface, which can reduce the back barrier height.[66, 75-76] The back contact barrier height can also be extracted from the temperature-dependent open-circuit voltage plotting (V_{oc}-T). The V_{oc} values increase rapidly with decreasing temperature, and the V_{oc} values will saturate at a temperature of around 200 K. When the measurement temperature further decreases, the V_{oc} values slowly decrease.[67] Therefore, the V_{oc}-T plotting presents two slopes and two intercepts (Figure 3.5a). E_{a1} (activation energy at temperature above 200 K) and E_{a2} (activation energy at temperature below 200 K) are extracted from the V_{oc}-T profiles at high-temperature and low-temperature ranges. When the absorbers are deposited on Mo back contacts, the dominant recombination in CIGSSe-based solar cells is the bulk recombination ($E_g \approx E_{a1}$). Therefore, the height of the back contact barrier (Φ_B) can be calculated as the difference between the E_{a1} and the E_{a2} values: $\Phi_B = E_{a1} - E_{a2}$.[67]

If the V_{oc}-T profile shows one slope in some CIGSSe-based solar cells (a very thin $MoSe_2$ layer for a Mo back contact or without GaO_x layer for an ITO back contact), indicating that E_{a1} is equal to E_{a2}. However, the back barrier exists obviously and cannot be zero. Therefore, the back barrier height should be calculated by other methods (Figure 3.5b). The band gap is the intrinsic property of absorber materials, it is a low temperature-dependent value.

Therefore, $E_g - \Phi_B$ should be considered in equation 3.7 rather than E_a, and the back barrier height can be extracted as $\Phi_B = E_g - E_a$.[77] The temperature-dependent V_{oc}-T equation can then be written:[43, 55]

$$V_{oc} = \frac{E_g - \Phi_B}{q} - \frac{kT}{q} \ln\left(\frac{J_{00}}{J_{sc}}\right) \quad (3.8)$$

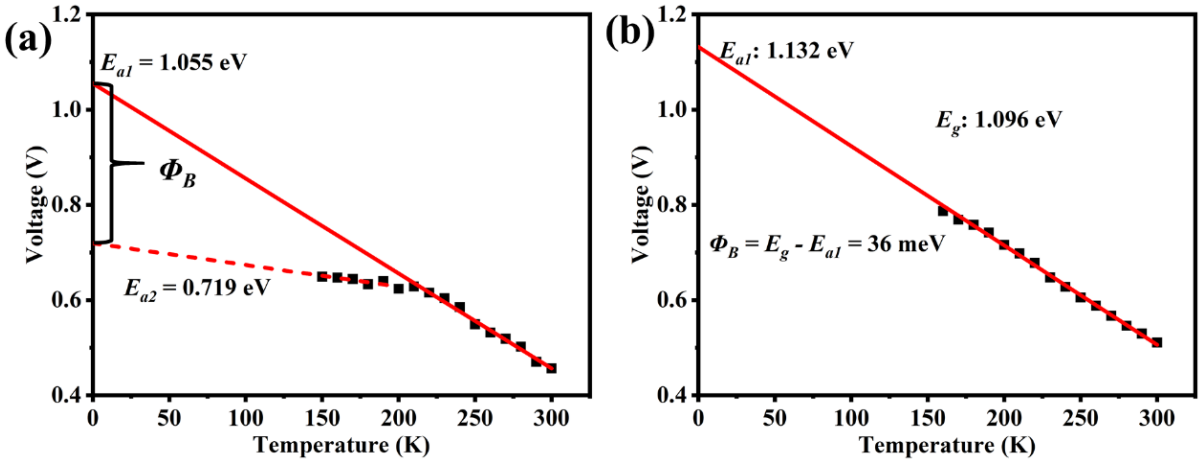

Figure 3.5: Temperature dependent open-circuit voltage profiles.

3.8 Quantum efficiency measurement

Quantum efficiency measurement is a valuable technique to characterize the photoresponse and photocurrent.[72] The quantum efficiency reflects the photoelectric conversion efficiency of solar cells at various wavelengths.[72]

$$EQE = \frac{n_e}{n_{ph}} = \frac{J_{EQE}/q}{P_L\lambda/hc} = \frac{J_{EQE}}{P_L} \times \frac{1}{\lambda} \times \frac{hc}{q} \tag{3.9}$$

where n_e is the number of generated electrons and n_{ph} the number of incident photons. J_{EQE} is the integrated current density, P_L is the power of the input light source, h is the Planck constant, c is the speed of light in vacuum, and λ is the photon's wavelength. The energy of the photons is written as hc/λ.

When the incident photons' energy is higher than or equal to the band gap energy of a semiconductor absorber material, the incident photons can excite the carrier from the valence band to the conduction band and generate electron-hole pairs. For example, if all the incident photons' energy above or equal to the semiconductor band gap is absorbed and the overall generated carriers are collected, the EQE is equal to 100%. On the contrary, the energy of photons below the band gap energy will be lost, therefore, the incident light cannot generate electrons and the corresponding EQE is equal to 0.

The typical EQE spectrum of CISSe solar cells is shown in Figure 3.6a. The band gap (E_g) can be calculated from the EQE spectrum by two different methods (Figure 3.6b and 3.6c). The same E_g value is obtained from both extraction methods. The Urbach energy (E_U) can also be calculated from the EQE spectrum in the long-wavelength tail by the following equation:[78-79]

$$\ln(EQE) = U_c + \frac{h\upsilon}{E_U} \tag{3.7}$$

where U_c is a constant and $h\upsilon$ is photon energy, respectively.

V_{oc} loss and E_U of the band tails present an empirical linear relationship in the literature, namely V_{oc} loss reduces with reducing E_U.[78-79] Band tails are defined as the density of states which extends from the valence or conduction band into the band gap of a semiconductor. In other words, the band tails are caused by structural and thermal disorders.

In most solar cells, the band tails act as one of the main factors in V_{oc} limitation, indicating that the band tails play acrucial role in the activity of carrier recombination. Therefore, the E_U reflects the performance of carrier transport and recombination. A high-quality semiconductor material has a small E_U value (7-15 meV), which is smaller than kT (~26 meV at $T \approx 298$ K).[80] Therefore, the E_U value can be reduced by improving semiconductor quality due to the reduction of structural and thermal disorder.

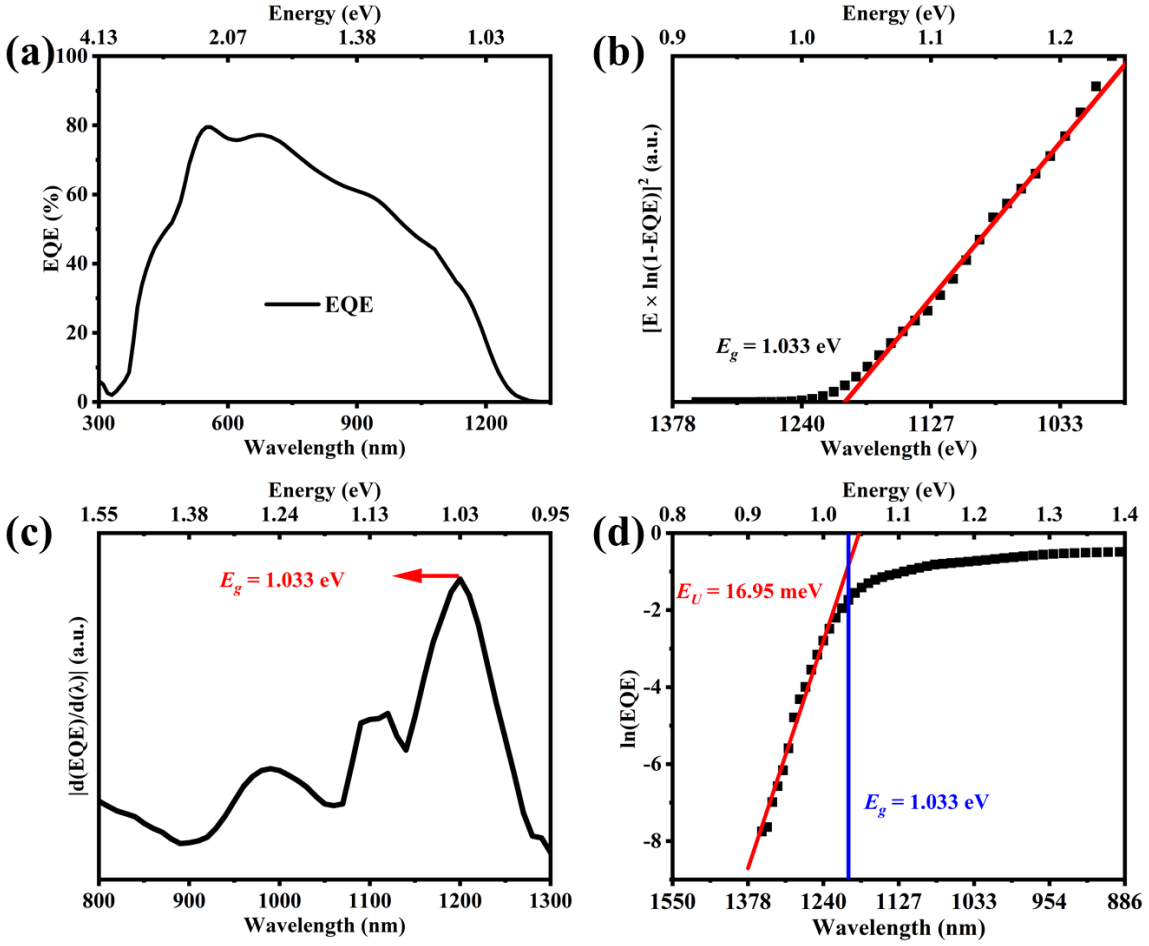

Figure 3.6: (a) EQE spectrum, (b) band gap extracted from $[E \times \ln(1\text{-}EQE)]^2$ *vs.* Energy, (c) band gap extracted from $|d(EQE)/d(\lambda)|$ *vs.* Energy, and (d) ln(EQE) as a function of photon energy at the long-wavelength edge to determine the Urbach energy E_U.

3.9 Capacitance-Voltage (C-V) measurement

A CIGSSe-based solar cell is a device that consists of semiconductor materials. The doping of the n-side (donor from the n-type window layers: intrinsic ZnO and Al-doped ZnO) is significantly higher than that of the p-side (acceptors from the p-type CIGSSe absorber). In other words, a narrow space of the n-side can provide a high carrier concentration. However, the p-type CIGSSe absorber should be thick enough to provide the same carrier concentration as the n-side to achieve carrier balance. Absorber composition, absorber quality, and material of the buffer layer will change the carrier concentration of the pn junction. Fabrication conditions of absorber (sulfur doping or sodium doping) and buffer layer selection affect the pn junction quality, impacting the CIGSSe solar cell efficiency. Therefore, it is crucial to characterize carrier concentration and the width of the depletion region of the CIGSSe-based solar cell.

The *C-V* technique has been utilized for characterizing semiconductor materials and devices, where the capacitance is measured and plotted as a function of voltage or frequency at room temperature. A classic model was exploited by Kimerling in 1974 based on a one-sided p^+n junction.[81] For CISSe thin film solar cells, the p-side is the absorber and the n-side is the window layer. The p-n junction includes the transition, and space charge regions (Figure 3.7). The space charge regions (or depletion regions) consist of the p-side (x_p) and n-side (x_n).[73]

$$W_d = x_p + x_n = \sqrt{\frac{2\varepsilon_0 \varepsilon_R V_{bi}}{q} \frac{N_A + N_D}{N_A N_D}} \tag{3.11}$$

where W_d is the width of the depletion region, q is the elementary charge, ε_0 is the vacuum permittivity, ε_R is the semiconductor dielectric constant, N_A is the doping density of acceptors, N_D is the doping density of donors, and V_{bi} is the built-in voltage. The doping of the n-side (donor from the n-type window layers) of the CIGSe-based solar cell is remarkably higher than that of the p-side (acceptors from the p-type absorber), $N_D >> N_A$. The depletion region is in a state of charge balance. No free carriers are inside the depletion region because the free carriers are totally depleted. The width of the n-side can be neglected, therefore, the W_d is mainly determined by the p-side of the space charge region, and it can be written as:[73, 82]

$$W_d \approx x_p, \qquad x_n \approx 0 \tag{3.12}$$

The majority carriers spill from the quasi-neutral region, simultaneously, these carriers present a Gaussian-shaped ‘Debye tail’ in the transition region.

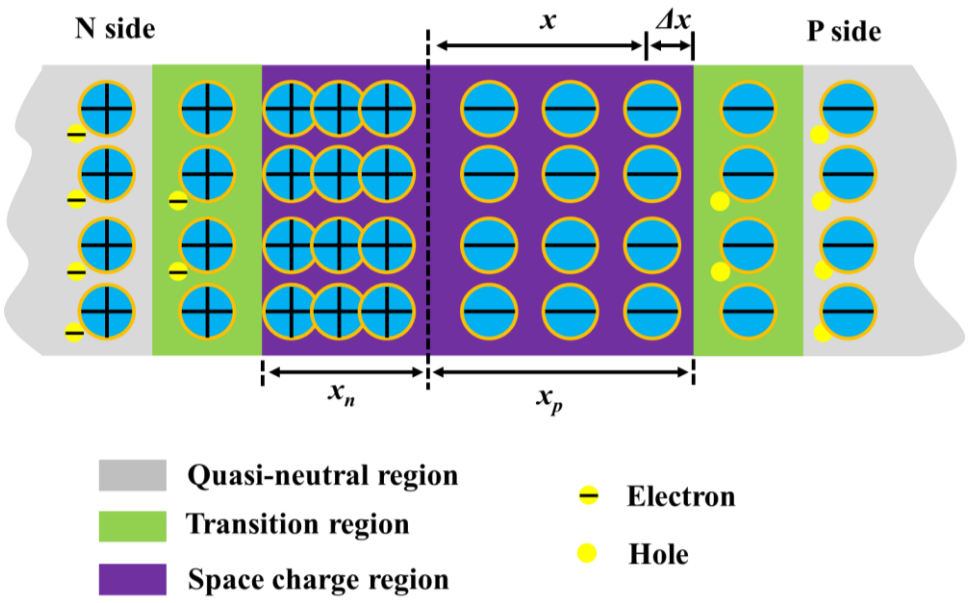

Figure 3.7: Schematic diagram of a pn juncrion. x_n and x_p are the width of space charge region (SCR) in the n-type and p-type semiconductor, respectively.

In addition, the 'Debye tail' of the majority carriers can be further extended into the space charge region (or depletion region). When a bias voltage increment ΔV is applied, the depletion width is increased by an amount Δx.[81] Then Gauss's law of carrier distribution can be written as:[81]

$$\Delta E = \frac{\Delta V}{x} = \frac{q}{\varepsilon_0 \varepsilon_R} N_{cv}(x) \Delta x \tag{3.13}$$

where x is the depletion width, ΔE is the electrical field flux, Δx is the independend variable, and $N_{cv}(x)$ is the fixed charge concentration. Therefore, the spatial distribution of free carriers on CIGSe-based can be determined from the CV results of the junction.[73, 82]

$$N_{cv}(x) = \frac{\varepsilon_0 \varepsilon_R}{q} \frac{\Delta V}{x \Delta x} \tag{3.14}$$

Solar cells' multi-layer structure can be considered as a parallel-plate capacitor with a unit area. We can obtain $x = \varepsilon_0 \varepsilon_R / C$ and $\Delta x = \varepsilon_0 \varepsilon_R \Delta C / C^2$. Then, equation 3.14 can be written as:[82]

$$N_{cv}(x) = \frac{C^3}{q \varepsilon_0 \varepsilon_R} \frac{\Delta V}{\Delta C} \tag{3.15}$$

$$x = W_d = \frac{\varepsilon_0 \varepsilon_R A}{C} \tag{3.16}$$

The CV measurement is performed as a function of both applied voltage and frequency at room temperature. The N_{cv} distribution in the depletion region can be extracted by adjusting the applied voltage range. The capacitance is a function of voltage at a specified frequency. Therefore, the measurement frequency plays a crucial role in identifying the real doping. There

are (still) traps and defects in the absorber, which will significantly affect the measurement results. Therefore, the frequency should be high enough to avoid the effects of traps and defects because they are unable to follow the high frequency of the measurement. In this thesis, we calculate the N_{cv} from the CV curve, which is measured at 100 kHz (Figure 3.8).

Figure 3.8 shows the doping profile extracted from the CV curve measured at 100 kHz. Generally, the minimum N_{cv} value is observed at 0 V bias voltage. In the literature, researchers will select the N_{cv} value at 0 V bias voltage for the carrier concentration of the p-n junction of CIGSSe-based solar cells.

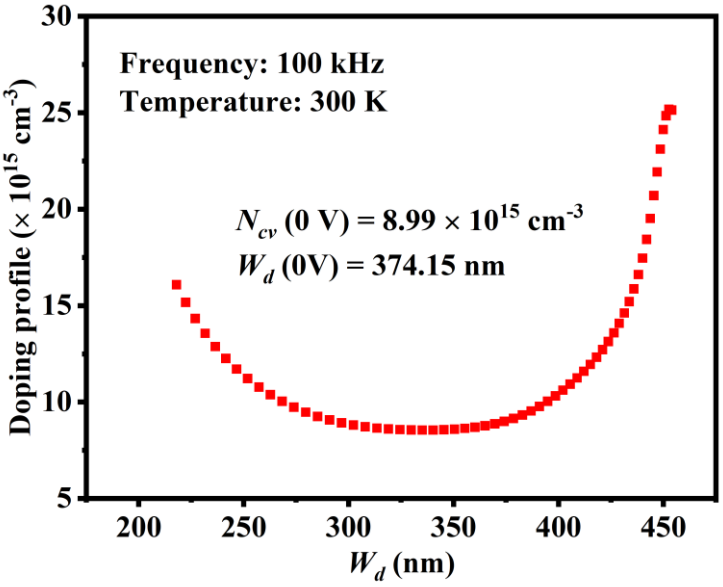

Figure 3.8: N_{cv} vs. W_d profile of submicron CISSe solar cells measured at 300 K with 100 kHz frequency.

4 S and Se co-annealing strategy for submicron $CuIn(S,Se)_2$ solar cells

This chapter is in part based on the following publication:

Yao Gao, Guanchao Yin, Yong Li, Tristan Köhler, Ihab Kardosh, Martina Schmid. An efficient S and Se co-annealing strategy for performance enhancement of solution-processed submicron $CuIn(S,Se)_2$ solar cells. ***IEEE Journal of Photovoltaics***. 2023, (DOI: 10.1109/JPHOTOV.2023.3334479). As the first author of this manuscript, I conceived the idea and fabricated all the devices, conducted the measurements, performed the data analysis and prepared the manuscript.

4.1 Motivation

The precursor film selenization is crucial in obtaining high-quality absorbers for thin film solar cell applications.[36-37] When the precursor selenization is carried out annealing in the low content of chalcogens atmosphere, it is not beneficial for forming a high-quality absorber consisting of large grains. Carrying out annealing in a high content of chalcogens atmosphere can provide a high pressure, which promotes the transformation of fine grains of the precursor film to large grains, leading to high efficiency.[37] However, films prepared with a high content of Se require a subsequent long KCN etching process to remove excessive Se and $Cu_{2-x}Se$. The highest-quality solution-processed CIGSe solar cell with 17.3% certified efficiency was achieved by annealing the hydrazine-based precursor film in nitrogen (without any additional Se) rather than subjecting it to conventional selenization.[29] However, the highly toxic hydrazine solvent hinders the further development of this method. Therefore, annealing the precursor films in a low content of Se may be an alternative strategy for CIGSe absorber fabrication, which can reduce the consumption of KCN by shortening the etching time. Optimization of the chalcogen content for selenization and shortening the KCN etching time should be balanced to obtain high-efficiency CISSe solar cells.

Interface recombination is observed in solution-processed CIGSSe films owing to a large number of Se vacancies (V_{Se}) and the Se-Cu di-vacancy complex (V_{Se}-V_{Cu}).[15, 49, 51, 83] Surface defects, copper and selenium vacancies, can be effectively passivated via a surface sulfurization of CIGSSe films.[22, 31, 49] Generally, surface sulfurization is carried out in an H_2S atmosphere. The valence band maximum (VBM) at the surface of the absorber can be lowered, leading to an increase in the band gap and the formation of a hole-recombination barrier.[49, 51] The S incorporation can improve the open-circuit voltage (V_{oc}) of the CIGSSe solar cells due

to a wider band gap. However, H_2S gas comes with the challenge of toxicity, and alternatives for S incorporation into the CIGSSe absorbers have attracted considerable interest.

This chapter compares different contents of chalcogens for precursor annealing to obtain submicron CISSe absorbers, including pure Se annealing atmosphere and Se and S co-annealing atmosphere. The Se pellet or the Se and S pellets provide the chalcogens' atmospheres. We deposited the Cu-In-TU-DMF precursor film on Mo back contact by spin-coating. The as-deposited precursor films are then annealed in different chalcogens atmospheres. We can obtain the optimum annealing atmosphere for our submicron CISSe absorber by comparing the corresponding materials measurement and the characterization of the devices. This annealing condition will be applied for our further research in this thesis.

4.2. Results and discussion

The GIXRD patterns of CISSe absorbers annealed in various atmospheres are presented in Figure 4.1a. The strongest Bragg reflection at 40.5º can be indexed to the (110) plane of the Mo back contact.[36-37] The positions of Bragg reflections at 26.9º, 44.7 º, and 53.1º correspond to the (112)/(103), (204)/(220), and (116)/(312) planes of chalcopyrite, respectively.[36-37, 84] The positions of these planes display slightly right-shifted compared to the positions of chalcopyrite $CuInSe_2$ (JCPDS: 40-1487) since all our absorbers include a small content of S (from the TU of the precursor), resulting in $CuIn(S,Se)_2$ (CISSe). A high Se vapor pressure is achieved during the annealing process, thus, a large amount of liquid Se will penetrate from the film surface into the whole film.[36] A pronounced shift of the (112) peak to larger angles is observed for the HS-CISSe absorber due to the higher concentration of smaller element S (Figure 4.1b). The H-CISSe absorber presents the strongest intensity of the (112) Bragg reflection and the smallest full width at half maximum (FWHM: 0.26º for L-CISSe, 0.23º for H-CISSe, and 0.39º for HS-CISSe), indicating that the H-CISSe has the best crystallinity in these absorbers.[31, 36, 84] The H-CISSe presents the $Mo(S,Se)_2$ Bragg reflections, whereas HS-CISSe and L-CISSe do not (Figure 4.1c).

The strong Raman peaks of the CISSe absorbers corresponding to the A_1 mode are observed at 177-184 cm^{-1} (Figure 4.1d). The shift to higher wavenumbers of this Raman peak compared to pure $CuInSe_2$ is in analogy to the XRD results attributed to the incorporation of S into the absorber layer.[36-37] For the same reasons, the Raman peak of HS-CISSe shows a more pronounced right shift than the L-CISSe and the H-CISSe. A shoulder peak is observed at 154 cm^{-1} in HS-CISSe, which is assigned to the ordered vacancy compound (OVC).[37] Equally, the shoulder peak displays a slight right shift, confirming the formation of the $CuIn_3(S,Se)_5$ OVC rather than pure $CuIn_3Se_5$ (152 cm^{-1}).

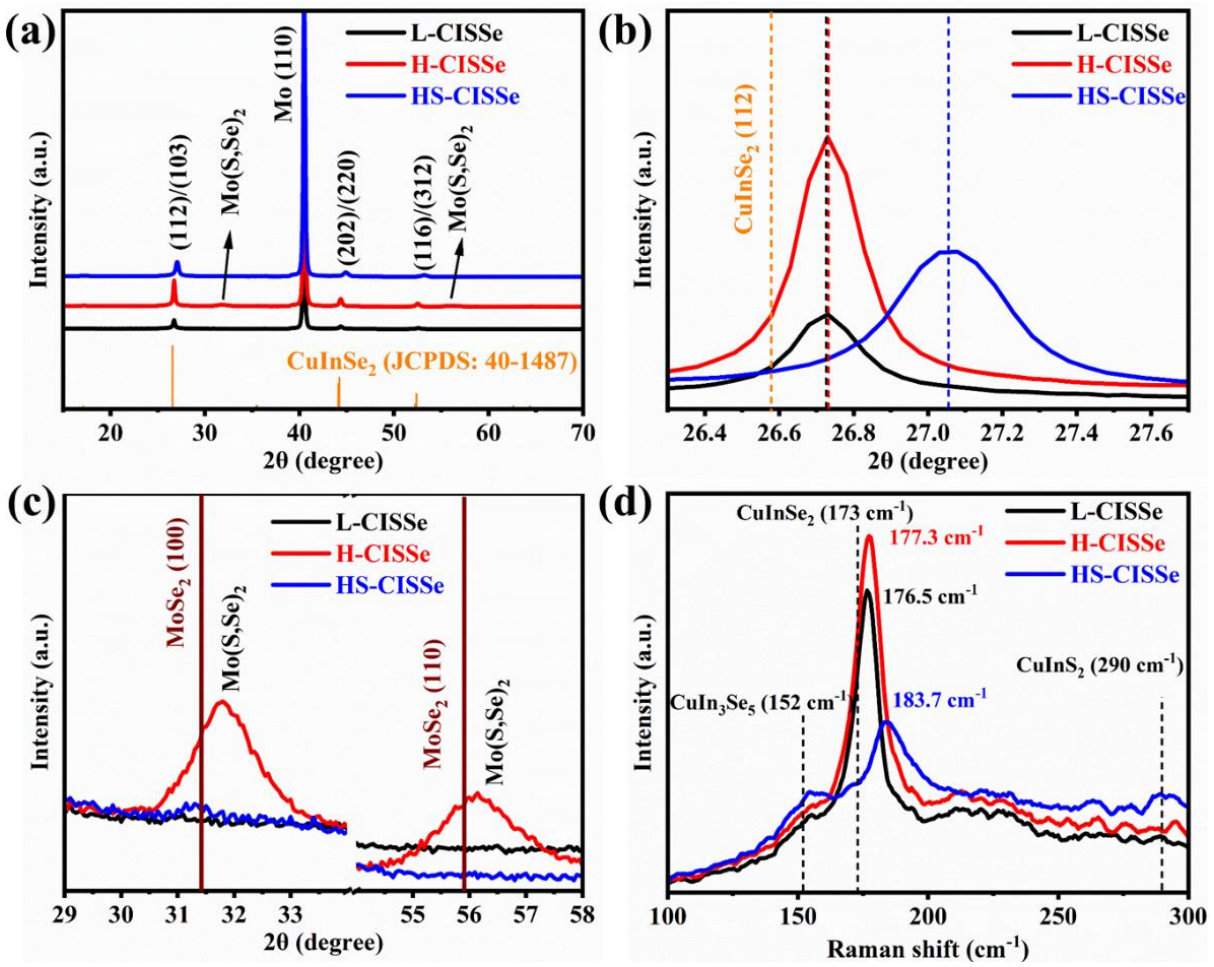

Figure 4.1: (a) XRD patterns, (b) the enlarged (112) diffraction peaks, and (c) Raman spectra of the CISSe absorbers annealed in various atmospheres. L-CISSe: low content of Se for annealing, H-CISSe: high content of Se for annealing, HS-CISSe: high content of Se and S for annealing.

The elemental distributions of the CISSe absorbers annealed in various conditions are shown in Figure 4.2. Compared to L-CISSe and H-CISSe absorbers, the HS-CISSe absorber reveals a notable enhancement in the S concentration and a simultaneous reduction in Se concentration (Figure 4.2a and 4.2b). A slight increase in the S concentration near the front surface of the HS-CISSe absorber can be attributed to the formation of an electrically benign $CuIn_3(Se,S)_5$ layer, which is in agreement with the Raman results (Figure 4.1d).

The surface defects are passivated by S atoms, simultaneously, absorbers with a S-rich surface have a wider band gap and a lower VBM (valence band maximum) leading to the formation of a hole-recombination barrier.[51, 85] Therefore, carrier recombination can be reduced, and carrier separation becomes more efficient.[22, 31, 49] Compared to the HS-CISSe absorber, the L-CISSe and the H-CISSe exhibit a higher Na concentration near the front surface (Figure 4.2c). Furthermore, the Na concentration of the L-CISSe absorber is significantly higher than that of the H-CISSe absorber.

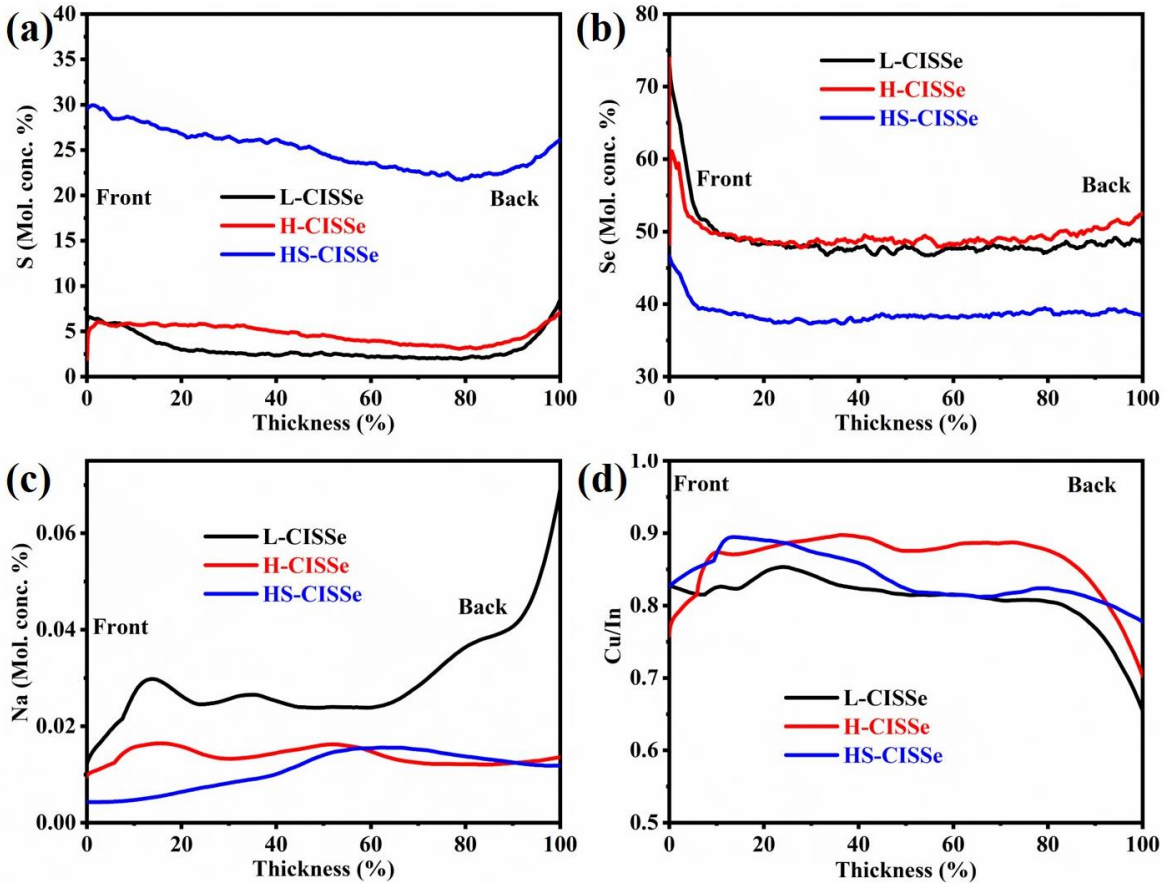

Figure 4.2: Concentration profiles of (a) S, (b) Se, (c) Na, and (d) Cu/In ratio of CISSe absorbers (after treatment with 10% HCl for removing CdS/i-ZnO/AZO top layers) measured by GDOES. The x-axis is normalized to 100% absorber thickness.

It is reported that Na can stay at grain boundaries and in the grain interior.[36, 83] These results confirm that the diffusion of Na from soda lime glass (SLG) is suppressed when the CISSe absorbers are sulfoselenized at a high chalcogen pressure. No matter if the CISSe absorbers are fabricated in pure Se or in Se and S conditions, they exhibit a Cu-poor surface (Cu/In < 1) (Figure 4.2d). The Cu/In ratios at the rear interface of the CISSe absorbers are higher for annealing in a high rather than in a low content of chalcogens. The decrease in the Cu/In ratio near the front surface can be ascribed to the formation of a Cu-poor surface.[36, 41, 86]

Cross-sectional scanning electron microscopy (SEM) images of CISSe solar cells fabricated under different annealing conditions are shown in Figure 4.3. When the precursor films are subject to annealing in pure Se, a large grain size (200 nm) is observed for the L-CISSe absorber (Figure 4.3a). However, some cracks (penetrating the absorber layer) are observed in the L-CISSe.

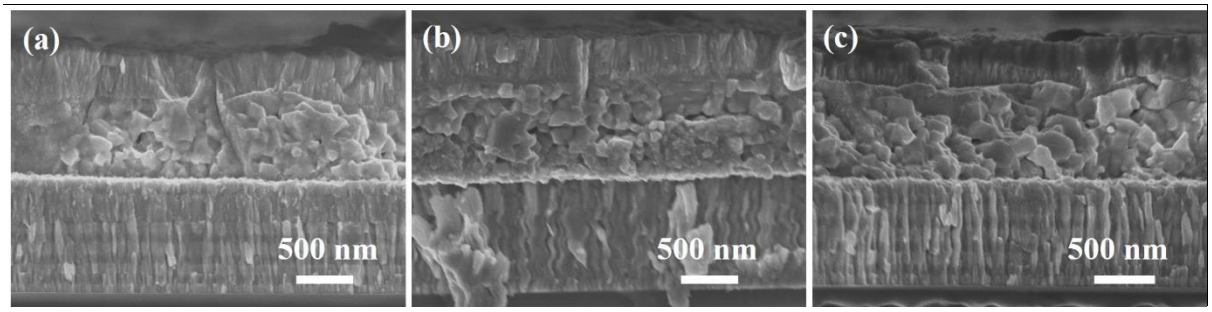

Figure 4.3: Cross-sectional SEM images of CISSe devices with absorbers annealed in different conditions: (a) L-CISSe, (b) H-CISSe, and (c) HS-CISSe.

Compared to the L-CISSe absorber, the H-CISSe absorber appears less dense with voids and consists of a large-grained (with 150 nm of grain size) top layer and a fine grained (50 nm grains) at the bottom layer (Figure 4.3b. It is reported that the incorporation of alkali elements is beneficial for forming large CIGSe grains.[49, 83] Smaller CISSe grains in the H-CISSe absorber may be explained by a lower amount of Na diffusing from the SLG substrate owing to the high selenium pressure (Figure 4.2c). The HS-CISSe absorber consists of large grains (larger than the L-CISSe and the H-CISSe). The S will diffuse fast along the grain boundaries and promote the formation of large grains towards the rear side.[54] These results reveal that an appropriate content of (Se and S) is required to promote the growth of CISSe with large grains, which is often correlated with high material quality.

Figure 4.4a presents the current-voltage (*J*-*V*) curves of the best CISSe solar cells from various annealing conditions, and the corresponding photovoltaic (PV) parameters are summarized in Table 3.1. The highest efficiencies of the submicron L-CISSe and H-CISSe devices are 7.53% and 8.57%, respectively. It is indicated that increasing the Se content is beneficial for efficiency improvement. S incorporation is beneficial to further improve the PV performance, and the highest efficiency of the HS-CISSe device is 10.44%. The efficiency improvement by incorporation of S during the annealing is mainly a result of enhanced open circuit voltage (V_{oc}) and fill factor (*FF*) (Table 4.1, and Figure 4.4d and 4.4f).[47, 51, 85, 87]

The V_{oc} values of HS-CISSe increase by 141.2 mV compared to those of H-CISSe. Furthermore, the HS-CISSe devices show an improvement in *FF* by 3.8%. The improvement in V_{oc} and *FF* can be attributed to two possible reasons: 1) a high S concentration in the absorber (Figure 4.2a) resulting in a wider band gap; 2) a related better crystallinity characterized by large CISSe grains (Figure 4.3). However, the values of short circuit current density J_{sc} for the HS-CISSe device decreases by 3.5 mA/cm^2 compared to the H-CISSe device, which is caused by a wider band gap owing to a higher S concentration in the absorbers (Figure 4.2a).[49, 85]

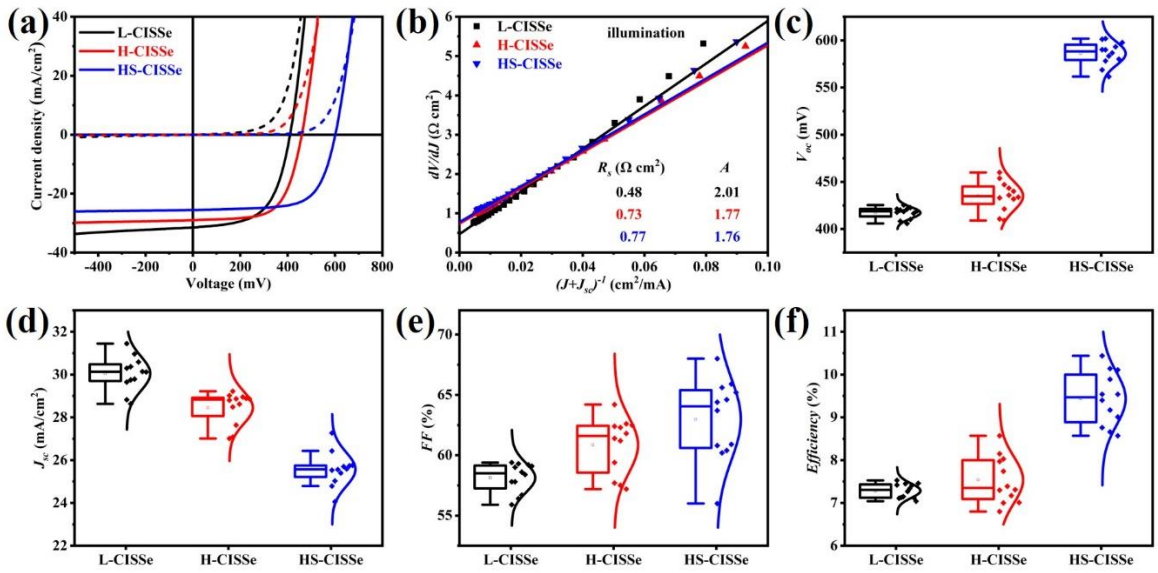

Figure 4.4: (a) *J-V* curves, (b) *dV/dJ* as a function of $1/(J + J_{sc})$ with a linear fit to extract R_s from the y-intercept and *A* from the slope; taken of the best CISSe solar cell from different annealing conditions. Statistical distribution of (c) open circuit voltage V_{oc}, (d) short circuit current density J_{sc}, (e) fill factor *FF*, and (f) efficiency derived from 12 devices for each annealing condition.

The plots of *dV/dJ vs.* $1/(J+J_{sc})$ are used to calculate the series resistance R_s and the ideality factor *A* of the CISSe devices (Figure 4.4b and Table 4.1). The H-CISSe device exhibits a larger R_s (0.73 Ω cm^2) value than the L-CISSe one (0.48 Ω cm^2), and then R_s further increases to 0.77 Ω cm^2 for the HS-CISSe. The shunt resistance (R_{sh}) shows a similar trend with R_s and the maximum R_{sh} is obtained for HS-CISSe (Table 3.1), indicating that the shunt path is passivated and the bulk recombination is reduced.[51] A possible reason may be a passivated shunt path by S incorporation so that a higher *FF* is achieved for the HS-CISSe rather than the L-CISSe and the H-CISSe.[41, 50-51] The ideality factor (*A*) and the saturation current density (J_0) present an opposite trend to R_s and R_{sh}. The smallest *A* and J_0 are observed for the HS-CISSe (Figure 4.4b), indicating that HS-CISSe has the best p-n junction quality and the smallest bulk recombination amongst these devices. Compared to L-CISSe, the smaller *A* value of the H-CISSe and HS-CISSe can be attributed to two reasons: 1) an electrically benign OVC layer is formed at the surface of Se and S-annealed CISSe absorbers (Figure 4.1);[36-37] 2) a low content of Na on the surface of Se and S-annealed CISSe absorbers, which promotes the formation of beneficial Cd_{Cu} donor defects during the CdS CBD process.[83] These results prove that the S incorporation has significant positive effects on the CISSe solar cells.

Table 4.1: Photovoltaic performance parameters of the best CISSe solar cells from different annealing conditions.

Sample*	Efficiency (%)	V_{oc} (mV)	J_{sc} (mA/cm^2)	FF (%)	R_s (Ω cm^2)	R_{sh} (Ω cm^2)	A	J_0 (mA/cm^2)
L-CISSe	7.3±0.2 7.53	417.2±6.0 410.1	30.1±0.8 31.4	58.1±1.2 58.4	0.48	240.96	2.01	1.58×10^{-2}
H-CISSe	7.5±0.5 8.57	434.9±15.6 460.0	28.5±0.8 29.0	60.9±2.3 64.2	0.73	507.61	1.77	1.09×10^{-3}
HS-CISSe	9.4±0.6 10.44	586.1±12.4 601.2	25.6±0.8 25.5	63.1±3.3 68.0	0.77	657.89	1.76	6.77×10^{-5}

* Efficiency, V_{oc}, J_{sc}, and FF are presented with (average ± standard deviation) calculated from 12 devices.

Figure 4.4c-f shows the statistical distributions of the PV parameters for the CISSe solar cells (12 CISSe sub-cells) with the absorbers obtained from different annealing conditions. An improvement of V_{oc}, FF, and efficiency is observed for the CISSe absorbers with increasing Se content or incorporating of S in the annealing process. On the contrary, J_{sc} presents an opposite trend. As discussed above, both the increase of the Se content and the introduction of S during the high-temperature annealing process will enhance the S content of the CISSe absorbers (Figure 4.2a). A high Se content can increase the S content because the higher annealing pressure suppresses the S volatilization (from the precursor solution). Additionally, when annealed in a Se and S environment, the CISSe solar cells exhibit higher V_{oc}, FF, and efficiency compared to the pure Se condition. Therefore, it is demonstrated that S incorporation is an effective strategy for improving the properties of CISSe solar cells.

The external quantum efficiency (EQE) spectra shown in Figure 4.5a are used to research the optical response of the CISSe solar cells fabricated under various annealing conditions. The EQE curves of these solar cells are highly similar at short wavelengths (300-500 nm), originating from the identical CdS/i-ZnO/AZO top layers of the CISSe solar cells. The L-CISSe solar cells have a higher EQE response than the H-CISSe and the HS-CISSe solar cells, which can be attributed to the lower S content of the L-CISSe. Compared to the H-CISSe, an increase in the EQE curves is observed in the range of 410 to 870 nm for HS-CISSe. These higher spectral responses can be attributed to a decrease in recombination caused by the passivation of shunt paths after increasing the S concentration and related higher collection efficiency (larger R_{sh} and smaller J_0, see Table 4.1).[41, 49]

However, the HS-CISSe solar cell has a lower EQE in the long-wavelength region (above 870 nm) than the H-CISSe solar cell, which can be attributed to the larger band gap (E_g) of the CISSe absorber with a higher S content. This is confirmed in Figure 4.5b, where the E_g values are calculated from the EQE curves (Table 4.2). Among these CISSe absorbers, the widest E_g (1.161 eV) is observed for the HS-CISSe film owing to the highest S concentration in the absorber (Figure 4.2).

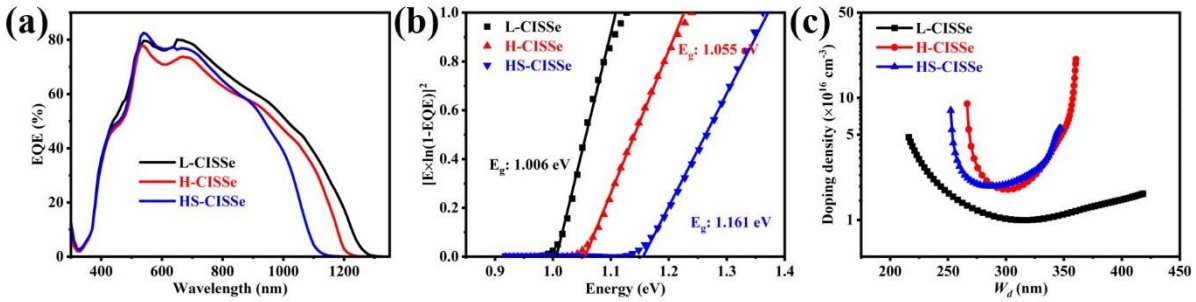

Figure 4.5: (a) External quantum efficiency, (b) extracted bandgaps, and (c) charge carrier concentration versus depletion region width for CISSe solar cells from different annealing conditions.

The charge carrier density (N_{cv}) and the depletion region width (W_d) can be extracted from the capacitance-voltage (*C-V*) profiles at 0 V bias voltage at room temperature and are presented in Figure 4.5c. N_{cv} rises with increasing Se content during annealing, and further with incorporating S. In close correlation, the W_d values present a reverse trend to N_{cv}. Therefore, the best efficient HS-CISSe device displays the largest N_{cv} (1.87×10^{16} cm^{-3}) and the smallest W_d (283.3 nm) (Figure 4.5 and Table 4.2). Compared to the H-CISSe absorber, the HS-CISSe absorber consists of large grains with fewer grain boundaries (Figure 4.3). Simultaneously, the grain boundaries of HS-CISSe are passivated by S (Figure 4.2), leading to the reduction of the bulk recombination in the HS-CISSe (larger R_{sh} and smaller J_0, see Table 4.1). Additionally, the Cd^{2+} will bond with S^{2-} to form CdS owing to the low solubility product ($K_{sp} = 10^{-27.94}$), indicating that the Cd^{2+} is depleted by S^{2-} during the CBD process, leading to a narrower W_d and a larger N_{cv} in HS-CISSe solar cells.[21, 47, 56, 88]

Looking at the V_{oc} deficit ($V_{oc,def}$) calculated from $V_{oc,def} = E_g/q - V_{oc}$, where q is the elementary charge, we can observe that the H-CISSe devices present a higher $V_{oc,def}$ than the L-CISSe and the HS-CISSe devices (Figure 4.6a), which can be attributed to the voids in the H-CISSe absorber (Figure 4.2). Bulk absorber quality and interface losses are the main factors of influence for $V_{oc,def}$ in CIGSSe-based solar cells. The significantly higher Na content in the L-CISSe compared to the H-CISSe absorber (Figure 4.2) can passivate the grain boundaries and reduce the density of interface-related shallow defects.[78-80] Even though the HS-CISSe absorber exhibits a smaller Na than the H-CISSe absorber (Figure 4.2), a higher S content in HS-CISSe cannot only passivate the grain boundaries but also minimize the interface recombination by forming an n-type conversion layer on the surface.[30, 89] Simultaneously, the smaller Na content on the surface of the HS-CISSe absorber is beneficial for the formation of a higher quality p-n junction (see also the smaller ideality factor, Table 4.1).[83]

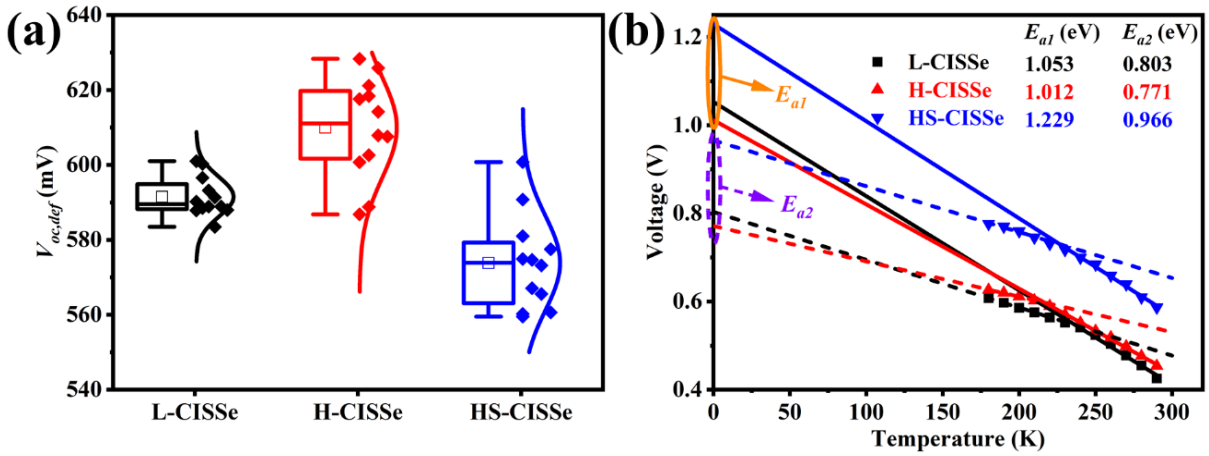

Figure 4.6: (a) Statistical distribution of V_{oc} deficit $V_{oc,def}$ derived from measurements of 12 CISSe devices. (b) Temperature dependent open circuit voltage of the CISSe solar cells from different annealing conditions.

There are two recombination paths in any solar cell: interface recombination and bulk recombination.[31] Temperature-dependent open-circuit voltage (*JVT*) profiling is an important electrical characterization method for thin-film solar cell research in order to determine the dominant recombination mechanism. The relationship between V_{oc} and temperature (T) is expressed by the following formula:[43, 50, 86]

$$V_{oc} = \frac{E_a}{q} - \frac{AkT}{q}\ln\left(\frac{J_{00}}{J_{SC}}\right) \tag{4.1}$$

where E_a is the activation energy of the dominant recombination mechanism, A is the diode ideality factor, k is the Boltzmann constant, J_{00} is the reverse saturation current density, and J_{sc} is the short circuit current density.

The activation energy can be extracted from the *JVT* profile by linear extrapolition of V_{oc} to 0 K. The interpolated $V(T)$ curves and extracted E_{a1} values from fitting in the high temperature regime of 230-300 K are given in Figure 4.6. Subtraction from the band gaps obtained from the EQE curves shown in Figure 4.5b, results in 0.047, 0.043, and 0.068 eV for L-CISSe, H-CISSe and HS-CISSe, respectively.

Table 4.2: Electrical parameters extracted from EQE and CV measurements of the best CISSe solar cells fabricated from various annealing conditions.

Sample	E_g (eV)	N_{cv} (cm^{-3})	W_d (nm)	$V_{oc,def}$ (mV)	E_{a1} (eV)	E_{a2} (eV)	Φ_B (eV)
L-CISSe	1.006	9.96×10^{15}	314.0	595.9	1.053	0.803	250
H-CISSe	1.055	1.80×10^{16}	306.5	595.0	1.012	0.771	241
HS-CISSe	1.161	1.87×10^{16}	283.3	559.8	1.229	0.966	263

These results of E_g - E_{a1} being very small indicate that the dominant recombination occurs in the absorber bulk rather than at the interface.[31, 43] Even though the bulk recombination is dominant in the HS-CISSe device, the increase in the difference between the E_g and E_{a1} values indicates that the interface recombination in HS-CISSe is slightly more serious than for the other cases. An explanation may be found in the significantly higher S concentration at the rear interface, leading to a slightly higher back barrier height (slight increase in R_s).

The activation energy values extrapolated in the low-temperature range (E_{a2}) are extracted from the *JVT* profiles between 180-210 K. The height of the back contact barrier (Φ_B) can be calculated as the difference between the E_{a1} and the E_{a2} values: $\Phi_B = E_{a1} - E_{a2}$.[67, 77, 90] The smallest Φ_B is observed for the H-CISSe device (0.241 eV) compared to L-CISSe (0.250 eV) and HS-CISSe (0.263 eV), which can be attributed to the formation of an electrical beneficial $Mo(S,Se)_2$ layer (Figure 4.1).[21] The slight increase in Φ_B of HS-CISSe does not significantly affect the PV performance. All in all, the Se and S co-annealing presents positive effects on the CISSe solar cell performance.

5 Na incorporation for Submicron $CuIn(S,Se)_2$

This chapter is in part based on the following publication:

Yao Gao, Guanchao Yin, Martina Schmid. Sodium Incorporation for Performance Improvement of Solution-Processed Submicron $CuIn(S,Se)_2$ Thin Film Solar Cells. ***Small***, 2023, 2302581 (DOI: 10.1002/smll.202302581). As the first author of this manuscript, I conceived the idea and fabricated all the devices, conducted the measurements, performed the data analysis and prepared the manuscript.

5.1 Motivation

Thining the absorber thickness can decrease the consumption of scarce indium, reducing manufacturing costs.[5, 43, 91-92] However, when the absorber layer thickness drops below 1 µm (submicron), the efficiency of the device degrades severely and the risk of shunt paths increases remarkably.[5, 41] Passivation of shunt paths will improve the device performance of submicron CIGSSe solar cells which can e.g. be achieved by alkali element post-deposition treatment.[18, 58, 93-95] Alkali incorporation can reduce the defect density and improve the absorber quality, which will enhance the open circuit voltage (V_{oc}) and fill factor (*FF*), resulting in efficiency improvement.[18, 58, 94-95] Furthermore, carrier recombination and the open circuit voltage deficit ($V_{oc,def}$) can be reduced by the incorporation of alkali elements into CIGSSe absorbers.[78] However, excessive alkali incorporation will deteriorate the absorber morphology (formation of pinholes and decrease in grain size), leading to inferior PV performance.[56] Therefore, it is crucial to control the alkali content to obtain highly efficient CIGSSe solar cells.

Sodium has been widely applied for alkali incorporation, affecting the grain size, crystal orientation, p-type conductivity, V_{oc}, *FF*.[19, 55, 96] The most common path for sodium incorporation is the post-deposition treatment (PDT), i.e. depositing a thin NaF layer after CIGSSe absorber growth by the co-evaporation process. NaF PDT can passivate the grain boundaries and form a Cu-poor surface, leading to PV performance improvement.[94, 97-98] Compared to absorber fabrication by co-evaporation, Na atoms can be introduced at different steps of CIGSSe growth from the precursor solution. For example, Na ions can be added into the precursor solution, prior to the precursor deposition, before or after selenization. Compared to NaF, NaCl offers low cost, benign nature, and good solubility in water.[56] The typical strategy for sodium incorporation into solution-processed CIGSSe solar cells is, therefore, soaking the precursor thin film in NaCl solution.[59-60] However, there is rare comparative research on Na incorporation using different strategies for solution-processed CIGSe. Therefore, corresponding research will be of great interest.

In this work, we focus on submicron (here 820 nm absorber layer thickness) solution-processed $CuIn(S,Se)_2$ (CISSe) solar cells and aim at performance enhancement by Na

incorporation. Sodium chloride aqueous-ethanol with 1 mol/L (1 M NaCl) is applied for sodium incorporation by using pre-deposition treatment (Pre-DT), pre-selenization treatment (Pre-ST), and post-selenization treatment (PST). The PV characteristics of the Pre-ST solar cells are better than those of the reference CISSe solar cells (without sodium treatment) and those processed by Pre-DT or PST. The soaking times (5 min, 10 min, and 15 min) and the NaCl concentration (0.2-1.2 M with a step of 0.2 M) of the Pre-ST are also studied. When the precursor films soak in 1 M NaCl for 10 min, CISSe solar cells achieve an efficiency of 9.6%. Compared to the reference CISSe, the open-circuit voltage (V_{oc}), short-circuit current density (J_{sc}), fill factor (FF), and efficiency of champion Pre-ST CISSe device are improved absolutely by 61.0 mV, 6.5 mA/cm^2, 9%, and 3.8%, respectively. Simultaneously, the open circuit voltage deficit ($V_{oc,def}$) and back barrier height values are remarkably reduced after NaCl treatment.

5.2 Results and discussion

5.2.1 Effects of Na treatment strategies

A 1M NaCl aqueous-ethanol solution (volume ratio of ultra-pure water to ethanol is 1:1) is used to investigate the effect of Na incorporation strategies. NaCl was introduced in various experiment stages (Figure 5.1): either prior to absorber deposition (pre-deposition treatment, Pre-DT), before selenization (pre-selenization treatment, Pre-ST), or after selenization (post-selenization treatment, PST).

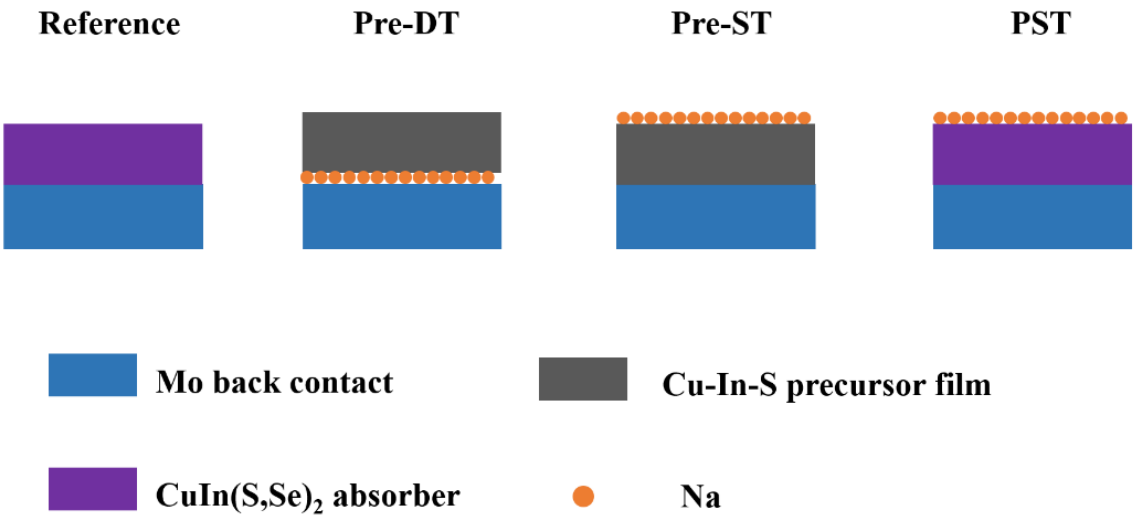

Figure 5.1: Schematic diagram of sodium treatment.

Raman spectroscopy measurements are utilized to identify the purity of CISSe thin films (Figure 5.2). All absorbers show a strong peak at short wavenumbers related to the A_1 vibration mode.[37, 99-100] The $CuInSe_2$ and $CuInS_2$ A_1 vibration mode peaks locate at 172 cm^{-1} and 290 cm^{-1}, respectively.[101-102] For our samples, we find a peak at 184 cm^{-1} for the reference, and at 179 cm^{-1} for the Na-treated absorbers. The right-shifted of the Raman peak compared to the A_1 mode of pure $CuInSe_2$ is attributed to the incorporation of S in the absorber layer.[100-102] The more pronounced right-shifted of the Raman peak of the reference sample points to a higher S concentration in the absorber than Na incorporation CISSe (Figure 5.4c). Previous literature has proven that the sharp Raman peak with a small full width at half maximum (FWHM) reflects better CISSe absorber quality.[100] The FWHM of the A_1 mode peak becomes smaller after Na incorporation (14.8 cm^{-1} for the reference, 11.5 cm^{-1} for Pre-DT, 9.9 cm^{-1} for Pre-ST, and 10.8 cm^{-1} for PST), indicating that Na incorporation is beneficial to improve the absorber quality. All these CISSe absorbers show a shoulder peak (c.a. 155 cm^{-1}) belonging to the $CuIn_3(S,Se)_5$ ordered vacancy compound layer.[37, 99] No impure compound characteristic peaks are observed in the CISSe absorber.

We carry out GDOES measurements on absorbers after electrical characterization and removal of the CdS/i-ZnO/AZO top layer. These CISSe absorbers (without/with Na treatment) show a Cu-poor composition (Figure 5.3). The reference CISSe absorber presents a lower Se and a higher S concentration than the Na-treated CISSe absorbers, indicating that the Se substitutes more S in Na-treated CISSe than the reference CISSe. The Na will bond with Se to form the Na_2Se_x (x >1) phase during the selenization, which is beneficial for the Se migration toward the rear side of absorbers.[36, 58]

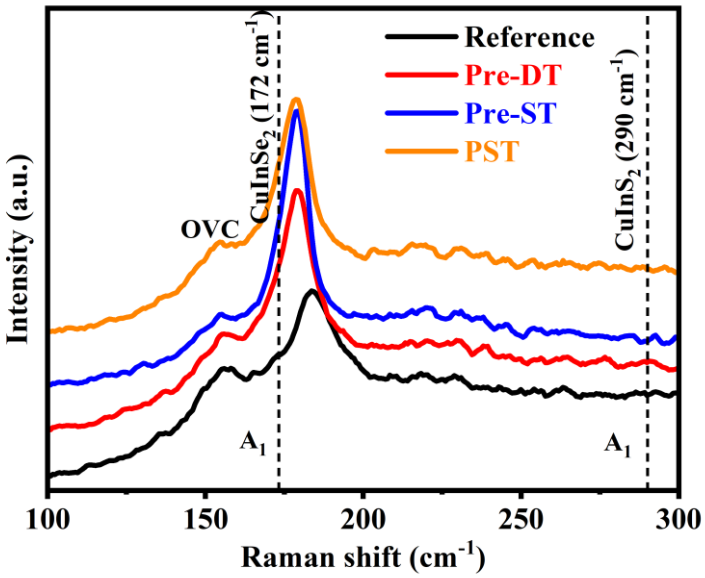

Figure 5.2: Raman spectra of CISSe absorbers without/with NaCl treatment.

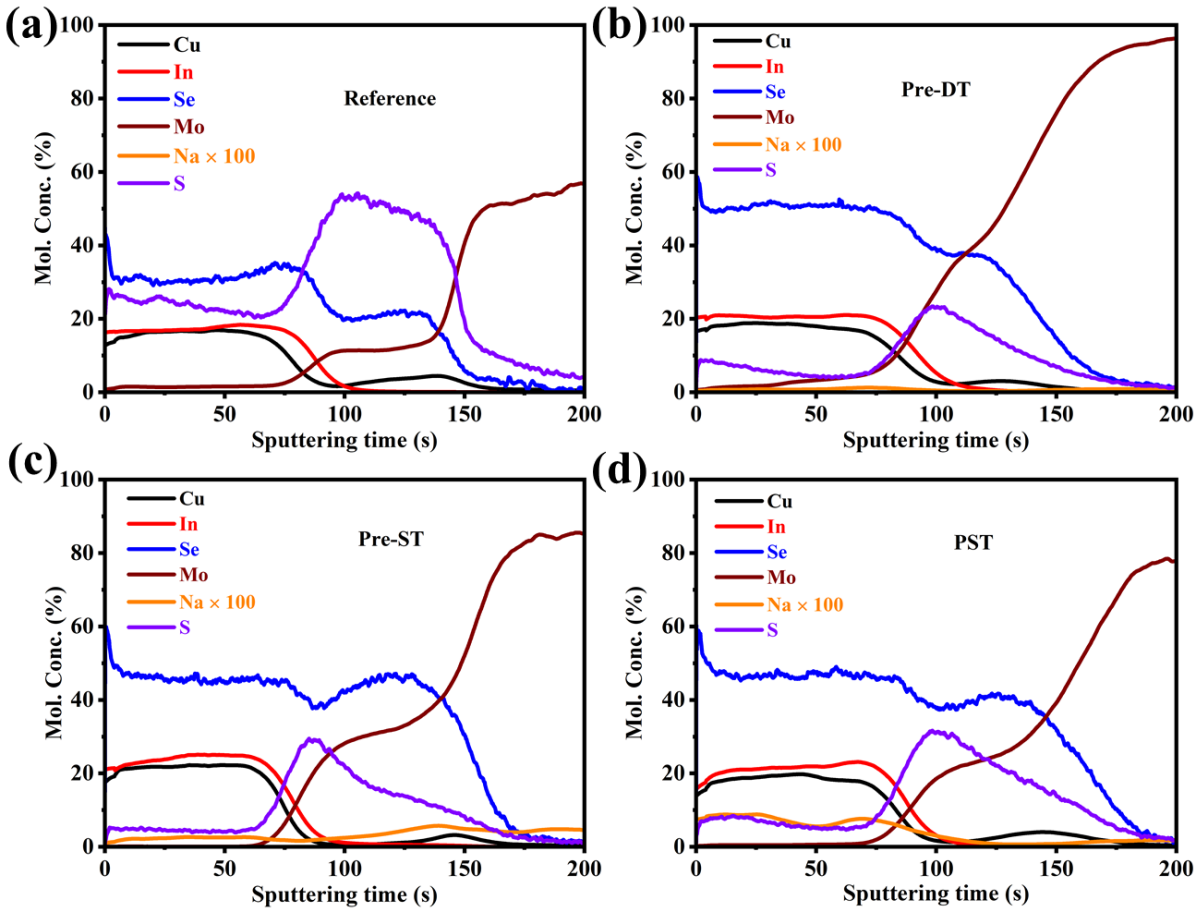

Figure 5.3: The elemental distributions of CISSe absorbers without/with Na treatment.

All these CISSe absorbers exhibit the maximum S concentration at the rear interface, implying that a thin S-rich $Mo(S,Se)_2$ is formed at the CISSe/Mo interface. The Pre-DT CISSe presents a thinner $Mo(S,Se)_2$ layer than the Pre-ST and PST CISSe. The Na-treated CISSe absorbers display a Na signal which is decreasing in sequence of PST > Pre-ST > Pre-DT.

The resulting concentration of Na, as well as Cu/In and S/(Se+S) ratios of CISSe without/with Na incorporation are shown in Figure 5.4. As expected, the Na-doped CISSe absorbers display higher Na concentrations than the reference (Na_{PST} > $Na_{Pre\text{-}ST}$ > $Na_{Pre\text{-}DT}$ > $Na_{reference}$, Figure 5.4a). It is reported that Na can occupy the grain boundaries and the grain interior.[36, 94] The post-selenization Na treatment does not further modify the microstructure of the as-selenized CISSe absorber, resulting in a large number of grain boundaries remaining in the absorber.[18, 56] Therefore, the high Na concentration in PST CISSe can be attributed to a great number of Na occupying the grain boundaries (Figure 5.4a). The Pre-DT and Pre-ST absorbers display a lower Na concentration at the front surface than in the bulk. A high Na concentration near the front surface of the absorber hinders the Cd_{Cu} donor defect formation during the CdS CBD process, leading to a lower quality of the p-n junction.[21, 103]

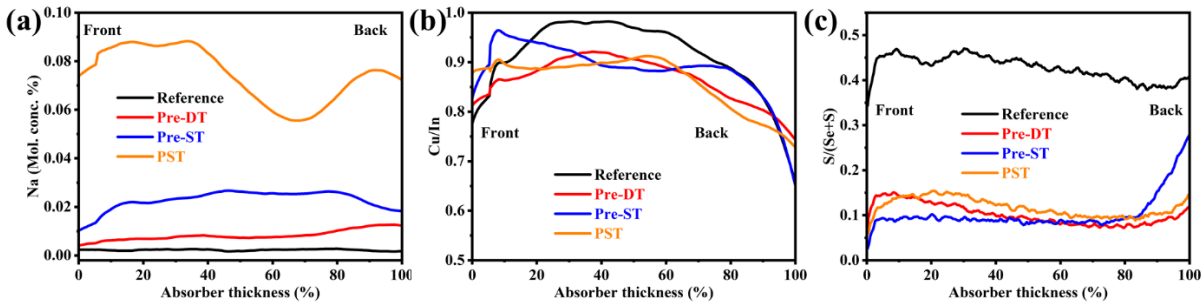

Figure 5.4: (a) Na concentration profiles, (b) Cu/In, and (c) S/(Se+S) ratios of absorbers measured by GDOES.

These CISSe absorbers without/with Na treatment exhibit a Cu-poor composition (Cu/In < 1, Figure 5.4b). Cu/In ratios towards the front surface first increase and then decrease. Compared to the bulk of absorbers, these CISSe absorbers present smaller Cu/In ratios at the front surface. The smaller Cu/In ratios at the front surface of CISSe can be explained by the formation of the $CuIn_3(S,Se)_5$ OVC layer, as also the Raman measurements revealed (Figure 5.2).[19, 104] The strongest Raman peak related to the OVC is found for the reference sample.

Na-treated CISSe absorbers exhibit a similar concentration of S/(S+Se) ratios, which are lower than for the reference CISSe absorber (Figure 5.4c). A higher Se concentration can be correlated to Na assisting the Se diffusion into the absorber via the formation of Na_2Se_x (x >1) phase during the high-temperature selenization.[36, 58] Thus, Na is beneficial to promote the substitution of S by Se during the high-temperature selenization.

To characterize the microstructure of CISSe absorbers without/with Na incorporation, the cross-sectional SEM images of CISSe devices are measured by A JEOL JSM-7500F SEM equipment and shown in Figure 5.5. The absorber thickness of these CISSe devices is approximately 820 nm. The reference CISSe, the Pre-ST, and the PST CISSe absorbers present a double-layer structure with a fine-grained layer on the bottom and a large-grained layer on top. The Pre-DT CISSe absorber exhibits a triple-layer structure: a dense fine-grained layer on the bottom, a thick large-grained layer on top of the absorber, and an assembly of loosely connected grains in between.[105] These loose grains may be attributed to the residual chlorine ion (Cl^-).[56] Similarly to the formation of SeF_6 when using NaF for Na incorporation, the chlorine ion (Cl^-) can be removed by forming $SeCl_4$ due to the reaction between Cl^- and Se vapor.[16-17, 56] The possible chemical equation between NaCl and Se vapor is shown below:

$$4NaCl + (2x+1)Se \rightarrow 2Na_2Se_x + SeCl_4 \uparrow \quad (5.1)$$

Large CISSe grains are firstly formed on top of the absorber during the high-temperature selenization.[37, 105] This large-grained CISSe top layer will hinder the volatilization of $SeCl_4$ coming from the rear in the case of Pre-DT, leading to the residual Cl^- inside CISSe absorber.[56] The remarkably large grains at the top of the Pre-ST CISSe absorber are formed owing to the Na_2Se_x-assisted (x >1) crystallization during the selenization.[36, 94, 106]

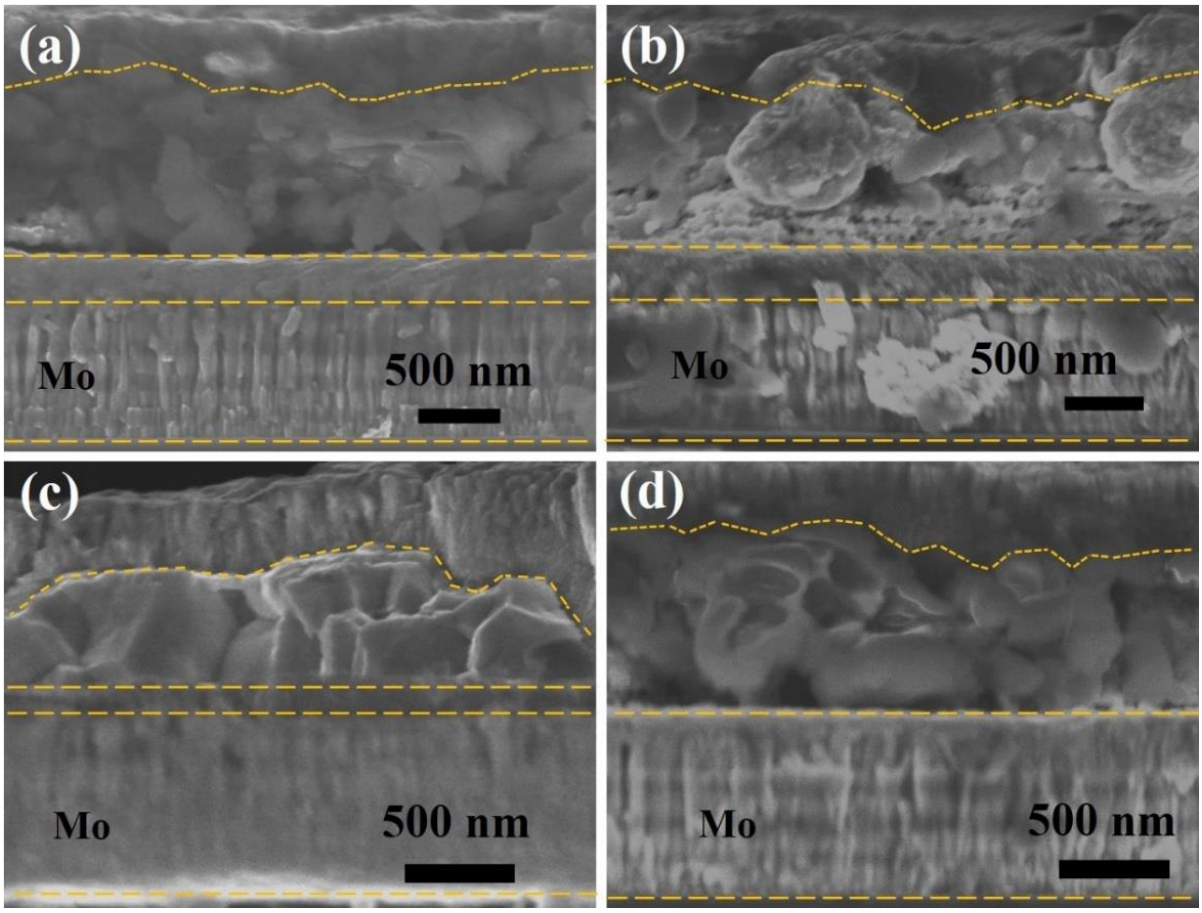

Figure 5.5: Cross-section SEM images of Reference device (a), Pre-DT device (b), Pre-ST device (c), and PST device (d).

Both the reference CISSe and the PST CISSe show a similar morphology. However, larger grains are observed in PST CISSe rather than in the reference CISSe, indicating that grains can further grow by the second high-temperature step after PST.[107-108] Simultaneously, the thickness of the fine-grained layer in the PST CISSe is obviously reduced compared to the reference CISSe.

The current density-voltage (*J-V*) characteristics of CISSe solar cells without/with NaCl incorporation are shown in Figure 5.6, and the corresponding device parameters are summarized in Table 5.1. After Na incorporation, the J_{sc} and efficiency of the best CISSe solar cells are improved owing to an increased conductivity (Figure 5.6a).[56] The highest efficiency achieved for the reference, Pre-DT, Pre-ST, and PST CISSe devices is 5.8%, 6.2%, 9.6%, and 7.4%, respectively. Comparing the best CISSe devices, the *FF* increases for Pre-ST and PST CISSe but decreases for Pre-DT CISSe compared to the reference. The decreased *FF* of the Pre-DT device can be attributed to the degraded microstructure of the absorber (Figure 5.5b).[58] V_{oc}, J_{sc}, and *FF* of the highest efficient (9.6%) Pre-ST CISSe device achieve 464.5 mV, 33.4 mA/cm^2, and 62.0%. These improvements in PV parameters are related to the uniform Na distribution (Figure 5.4) as well as the better absorber morphology (Figure 5.5).

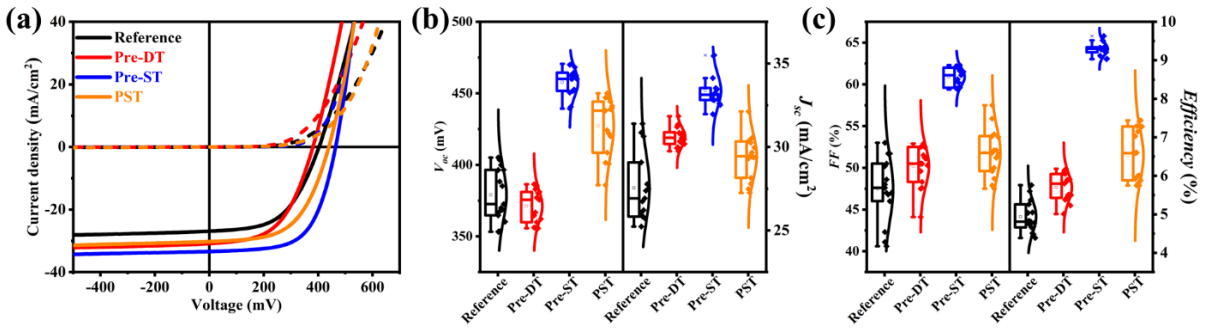

Figure 5.6: (a) *J-V* curves of the best CISSe solar cells without/with NaCl treatment; Statistical distribution of (b) open circuit voltage V_{oc} and short circuit current density J_{sc}, (c) fill factor *FF* and efficiency derived from 15 devices for without/with NaCl treatment.

The statistical distributions of PV parameters for 15 CISSe sub-cells for each recipe are shown in Figure 5.6b-c. The trends are similar to those of the corresponding highest-efficiency CISSe devices. Na-treated CISSe solar cells present an efficiency improvement, which is mainly attributed to the enhancement of J_{sc} and *FF*.[58, 107-108] The Pre-ST and the PST solar cells display an increase in V_{oc}, however, a degraded V_{oc} is observed in the Pre-DT solar cells owing to the deteriorated microstructure.[56, 58]

The average values of V_{oc}, J_{sc}, *FF*, and efficiency are respectively 379.0 mV, 27.5 mA/cm^2, 47.5%, and 4.9% for the reference CISSe. When the Pre-ST strategy is utilized for Na incorporation, these parameters are relatively increased by 15.1%, 24.2%, 20.0%, and 65.5%, respectively (Table 5.1). Simultaneously, the PV parameters of Pre-ST CISSe solar cells are more uniform than for the other types, indicating that the Pre-ST is an effective strategy for PV performance improvement.

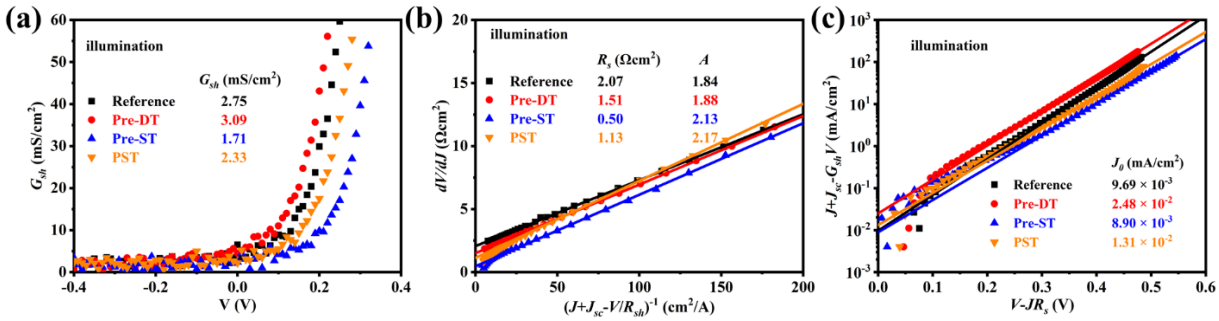

Figure 5.7: Plots of (a) G_{sh} *vs. V*, (b) *dV/dJ vs.* $1/(J+J_{sc}-V/R_{sh})$ for derivation of R_s and *A*, and (c) semi-logarithmic plot of $J+J_{sc}-G_{sh}V$ *vs.* $V-JR_s$ to determine J_0.

Table 5.1: Photovoltaic performance parameters of CISSe solar cells subject to various Na incorporation strategies.

Sample*	V_{oc} (mV)	J_{sc} (mA/cm^2)	*FF* (%)	*Efficiency* (%)	G_{sh} (mS/cm^2)	R_{sh} (Ω cm^2)	R_s (Ω cm^2)	*A*	$J_0 \times 10^{-3}$ (mA/cm^2)
Reference	380±18 403.5	27.5±2 26.9	47.5±3.8 53.0	4.9±0.4 5.8	3.6±1.3 2.75	300.1±61.6 363.64	2.6±0.3 2.07	1.9±0.1 1.84	33.8±28.3 9.69
Pre-DT	371±11 381.0	30.6±0.6 30.9	50.2±2.4 52.5	5.7±0.4 6.2	3.9±1.4 3.09	282.8±77.1 323.62	1.8±0.3 1.51	2.0±0.1 1.88	60.3±30.0 24.85
Pre-ST	458±10 464.5	33.4±1.0 33.4	60.9±1.1 62.0	9.3±0.2 9.6	2.1±0.4 1.71	484.5±76.2 584.79	0.7±0.1 0.50	2.17±0.1 2.13	4.3±1.8 8.90
PST	430±20 439.9	29.4±1.3 30.3	51.8±2.8 55.9	6.5±0.7 7.4	2.6±0.4 2.33	390.4±52.5 429.18	1.8±0.5 1.13	2.3±0.2 2.17	19.6±11.5 13.12

* Efficiency, V_{oc}, J_{sc}, and *FF* are presented with (average ± standard deviation) calculated from 15 devices.

The external quantum efficiency (EQE) spectra of these CISSe devices without/with Na incorporation are shown in Figure 5.8a. The EQE curves are highly similar below the wavelength of 390 nm due to the identical CdS/i-ZnO/AZO top layers.[87] Obvious improvements of EQE responses at the wavelength above 930 nm are observed in CISSe absorbers with Na incorporation. The improvement in EQE above 930 nm wavelength can be attributed to the higher Se and lower S concentration in the Na-treated CISSe absorbers (Figure 5.4), resulting in a smaller band gap as detailed below. The Pre-ST CISSe solar cell exhibits on average a 20% higher EQE (400-1100 nm) response with a maximum value of 86% at 550 nm, which can be attributed to the more uniform Na concentration in the bulk as well as the better microstructure compared to the other absorbers.

The band gaps (E_g) of these CISSe absorbers are extracted from the analysis of the EQE derivative ($|d(EQE)/d\lambda|$).[108] The reference CISSe absorber has the largest E_g (1.127 eV), which can be explained by the notably high S concentration (Figure 5.4c). The CISSe absorbers with Na incorporation show similar S and Se concentrations, leading to similar E_g values, 1.046 eV for Pre-DT, 1.029 eV for Pre-ST, and 1.042 eV for PST, respectively.

Alkali treatment can significantly reduce the open circuit-voltage deficit $V_{oc,def}$ owing to the improvement in absorber quality and the decrease in the carrier recombination.[78-79] $V_{oc,def}$ is defined as $E_g/q - V_{oc}$, where the q is the elementary charge.[78, 105] After Na incorporation, the $V_{oc,def}$ can be significantly reduced (Figure 5.8c). Thanks to the uniform E_g and V_{oc} values, the Pre-ST CISSe solar cells present the uniform $V_{oc,def}$ distribution (Table 5.1 and Table 5.2).

The Urbach energy (E_U) is a further indicator of the semiconductor quality, which has been used to evaluate the performance of the solar cell.[79, 109] After Na incorporation, E_U reduces from 21.67 meV for the reference CISSe to 17.19 meV for the Pre-DT CISSe, 16.20 meV for the Pre-ST CISSe, and 14.86 meV for the PST CISSe (Figure 5.8c). The reduced E_U reflects better carrier transport and less carrier recombination in the Na-treated CISSe solar cells.[78-79]

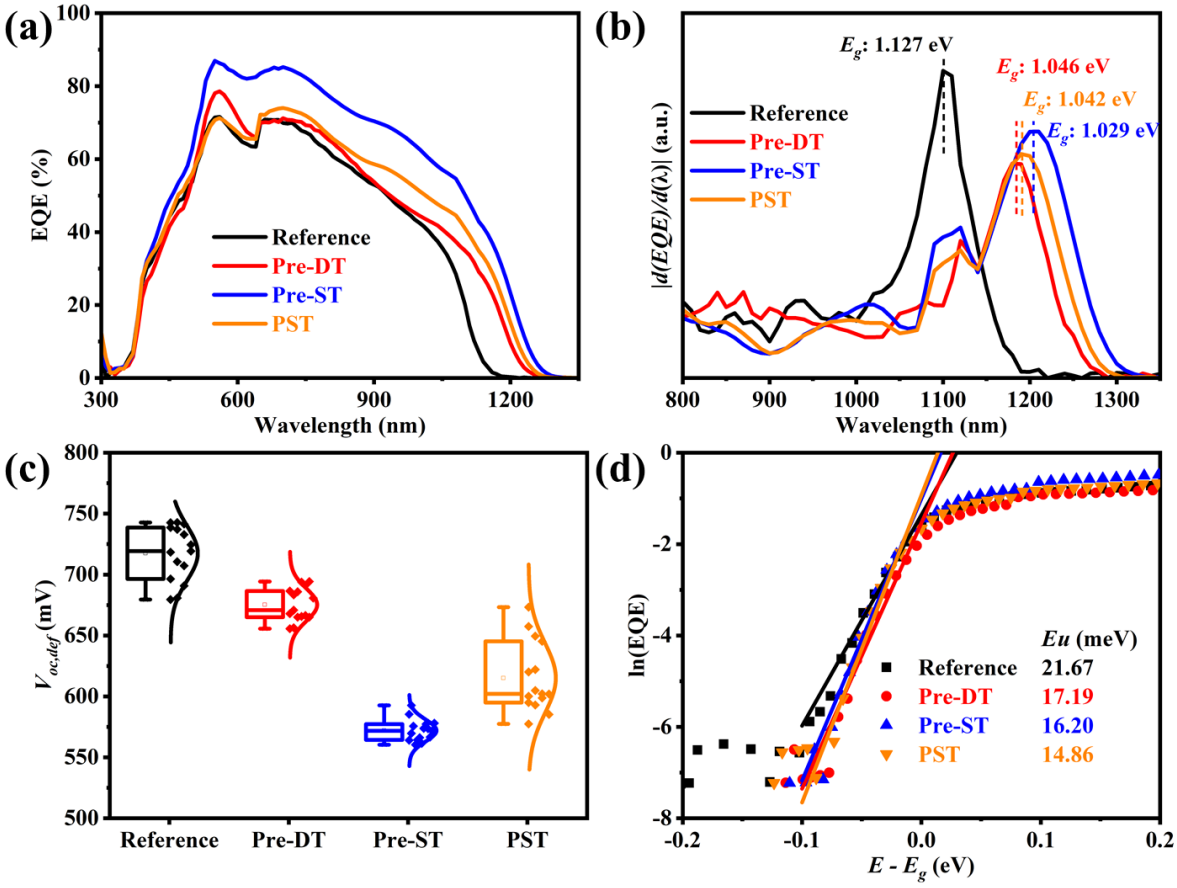

Figure 5.8: (a) External quantum efficiency curves, (b) band gaps, (c) $V_{oc,def}$, and (d) Urbach energy of CISSe solar cells without/with Na incorporation.

The acceptor doping density (N_A) and the width of the depletion region (W_d) of the highest efficient CISSe solar cells of each type are extracted from the room temperature *C-V* profiles (Figure 5.9a) by the following equations:[31]

$$\frac{1}{C^2} = \frac{2}{q\varepsilon_0\varepsilon_R N_A} V = \frac{2}{q\varepsilon_0\varepsilon_R N_A}(V_{bi} - V_{app}) \tag{5.2}$$

$$W_d = \frac{\varepsilon_0\varepsilon_R A}{C} \tag{5.3}$$

where C and A stand for the measured capacitance and the active area of the device, q, ε_0, ε_R, V_{bi}, and V_{app} represent the elementary charge, permittivity in the vacuum, the dielectric constant of CIGSe, built-in voltage, and applied voltage. The N_A and W_d are extracted from the forward bias voltage and at 0 bias voltage, respectively.

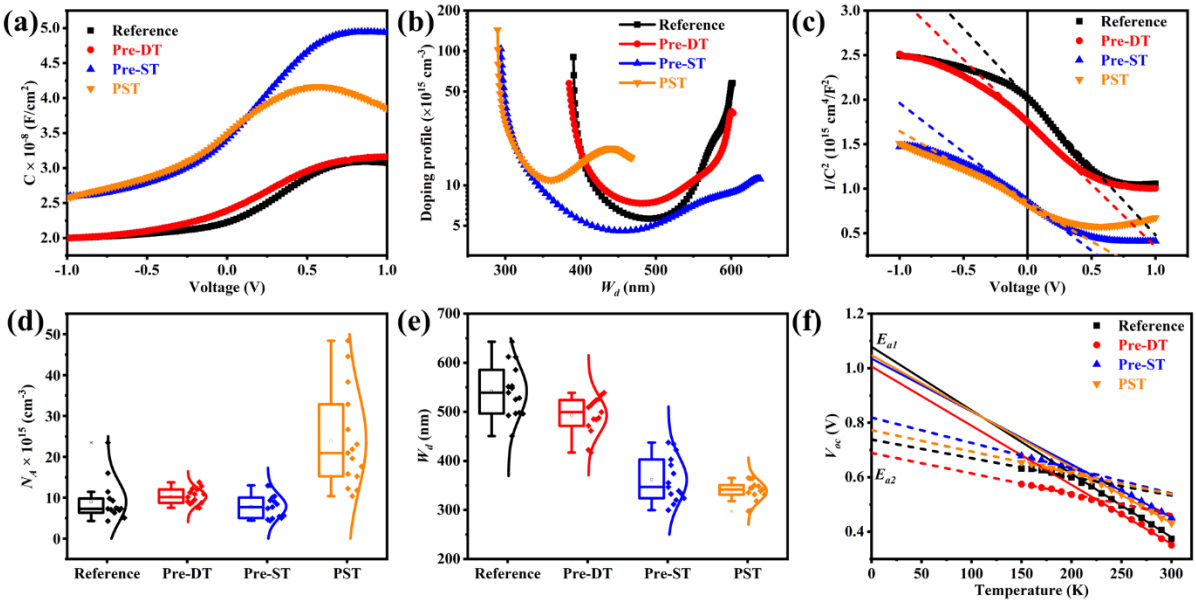

Figure 5.9: (a) *C-V* curves, (b) doping profiles, and (c) Mott-Schottky plot $1/C^2$ vs. V. Statistical distribution of (d) N_A, and (e) W_d derived from measurements of 15 CISSe sub-cells. (f) temperature-dependent V_{oc} of CISSe solar cells without/with NaCl incorporation.

For the reference CISSe solar cell, an N_A of 6.3×10^{15} cm^{-3} and a W_d of 522.4 nm are found (Figure 5.9b). These results indicate that N_A is affected by the defect concentration owing to a great number of Cu vacancies (Cu-poor absorber, Figure 5.4b). In other words, the N_A value is influenced by the Na-doping level and defect concentration. The Pre-DT CISSe and PST CISSe present an increase in N_A, whereas a smaller value of N_A is observed from the Pre-ST CISSe device (Figure 5.9c and Table 5.2). The microstructure of the absorber can also affect the result of CV measurement.[56] The pronounced low value of N_A of Pre-ST CISSe can be attributed to the large-grained absorber with a small number of grain boundaries. With Na incorporation, the Na_{Cu} defect will form on the surface of CISSe absorbers, hindering the Cd^{2+} diffusion during the CdS CBD process (Figure 5.4a).[21, 56] Therefore, with increasing the Na concentration, the W_d values of the corresponding solar cells decrease (Figure 5.9b and Table 5.2). This is most pronounced for Na addition on the top of the precursor/absorber layer.

The statistical distributions of N_A and W_d are shown in Figure 5.9d-e. The reference CISSe, Pre-DT CISSe, and Pre-ST CISSe exhibit similar uniform N_A values. However, the PST CISSe devices display larger N_A values than other Na incorporation strategies, which can be ascribed to the high concentration of Na in the PST CISSe absorbers. After Na incorporation, CISSe devices present smaller W_d values than the reference CISSe devices (Figure 5.9e).

Table 5.2: The electrical parameters of the best efficiencies CISSe devices without/with Na incorporation.

Sample*	E_g (eV)	$V_{oc,def}$ (mV)	$N_A \times 10^{15}$ (cm^{-3})	W_d (nm)	E_{a1} (eV)	E_{a2} (eV)	Φ_B (eV)
Reference	1.09±0.04 1.127	717.5±22.5 723.5	9.0±4.9 6.3	542.1±53.1 552.4	1.079	0.738	0.341
Pre-DT	1.05±0.01 1.046	675.2±13.3 665.0	10.3±1.9 7.5	493.1±37.5 499.5	1.007	0.689	0.318
Pre-ST	1.03±0.01 1.029	572.2±8.8 564.5	7.9±2.9 4.6	361.6±45.9 437.5	1.036	0.819	0.217
PST	1.04±0.01 1.042	615.1±28.6 602.1	24.0±11.9 11.9	338.4±21.0 341.7	1.048	0.773	0.275

* E_g, $V_{oc,def}$, N_A, and W_d are presented with (average ± standard deviation) calculated from 15 devices.

Temperature-dependent open-circuit voltage (*JVT*) measurement is an effective technique to evaluate the dominant recombination mechanism. The activation energy (E_a) is extracted from the *JVT* profile by linear extrapolation at $T = 0$ K via the following formula:[31]

$$V_{oc} = \frac{E_a}{q} - \frac{AkT}{q}\ln\left(\frac{J_{00}}{J_{SC}}\right) \quad (5.4)$$

where E_a, A, k, and J_{00} are the activation energy of the dominant recombination mechanism, the diode ideality factor, the Boltzmann constant, and the reverse saturation current density, respectively.

Two extrapolated values are obtained from slope fitting in the high and the low temperature regime: E_{a1} (230-300 K) and E_{a2} (150-200 K) (Figure 5.9f). The small differences between E_g and E_{a1} are 0.048, 0.039, 0.007, and 0.006 eV, for reference, Pre-DT, Pre-ST, and PST CISSe, respectively. These small values indicate that the dominant recombination occurs in the absorber bulk.[31] The back barrier height (Φ_B) can be calculated as the difference between E_{a1} and E_{a2}, and Φ_B drops from > 0.3 eV for the reference to close to 0.2 eV only for the Pre-ST CISSe (Table 5.2). [67, 90] Na will also incorporate into the Mo back contact, which is beneficial for $Mo(S,Se)_2$ layer formation, resulting in the reduction of the Φ_B.[56, 67]

5.2.2 The effect of pre-selenization treatment times

The soaking times of the precursor films in 1 M NaCl aqueous-ethanol solution can change the Na content in the final CISSe absorbers.[16, 19, 55-56, 58, 96] Based on the above discussion (Figure 5.6 and Figure 5.9), the Pre-ST for Na incorporation is the most promising strategy for performance improvement. Therefore, Pre-ST is utilized for investigating the effect of various soaking times in 1 M NaCl solution.

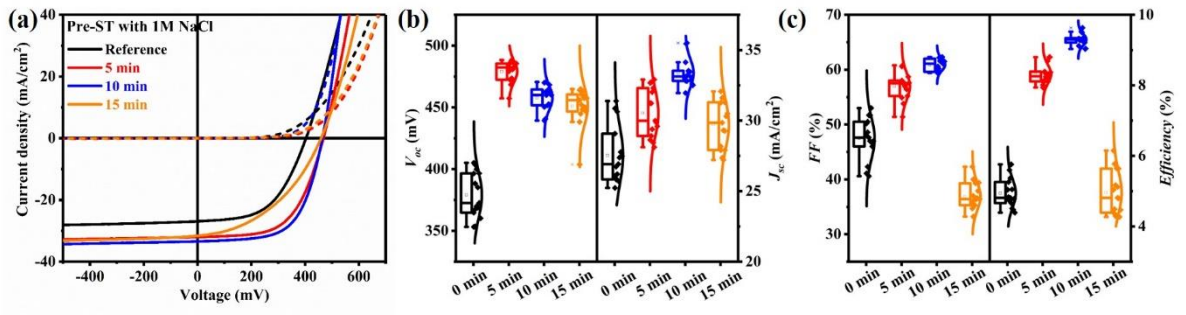

Figure 5.10: (a) *J-V* curves, Statistical distribution of (b) V_{oc} and J_{sc}, (c) *FF* and efficiency of CISSe with various times pre-selenization treatment in 1 M NaCl solution.

The *J-V* curves of CISSe solar cells with 1 M NaCl pre-selenization treatment for various times are shown in Figure 5.10a and the corresponding PV parameters are detailed in Table 5.3. For all investigated soaking times, both J_{sc} and V_{oc} increase significantly. When the CISSe precursor films are subject to 1 M NaCl for 5 min, the highest average V_{oc} values are obtained amongst these CISSe solar cells without/with NaCl treatment, indicating that a short NaCl treatment time is beneficial for V_{oc} improvement. With prolonging the soaking time, J_{sc} firstly increases and then decreases with the maximum reached for 10 min (33.4 mA/cm^2 for average). *FF* and J_{sc} show a similar tendency, with an initial increase towards the maximum for 10 min NaCl treatment and a subsequent decrease. Significantly low *FF* values (32.9% on average) are observed for the CISSe solar cells with 15 min NaCl treatment, leading to the remarkably low efficiencies obtained. The low efficiencies are attributed to the degradation of the CISSe grain size owing to the high concentration of Cl^- ions.[56] The Se content is crucial for removing Cl^- ions by the formation of $SeCl_4$, similar to removing the F^- ions (from NaF) by forming SeF_6 vapor.[16-17, 103] In our research, an equal content of Se is utilized for all selenization processes. For precursor films with longer NaCl soaking times, the Se content cannot support the full removal of the Cl^- ions. The residual Cl^- will form holes and electrons recombination centers, leading to serious recombination. This reason can also explain that the highest V_{oc} values are obtained from the precursor films for short NaCl treatment time (Se excessive). After optimization of the soaking time of the precursor films (1 M NaCl for 10 min), the best CISSe device achieves 9.6% with a V_{oc} of 464.5 mV, a J_{sc} of 33.4 mA/cm^2, and a *FF* of 62.0%.

After Na incorporation, the CISSe absorbers present a significant improvement in photoelectric response intensity in the visible and infrared wavelength ranges ($\lambda > 450$ nm) (Figure 5.11). The improvement implies better collection capability of the photo-generated carriers, which is caused by a better absorber quality with fewer defects. Simultaneously, NaCl-treated CISSe absorbers have a smaller E_g value than the reference CISSe due to the smaller S content (Figure 5.11b).

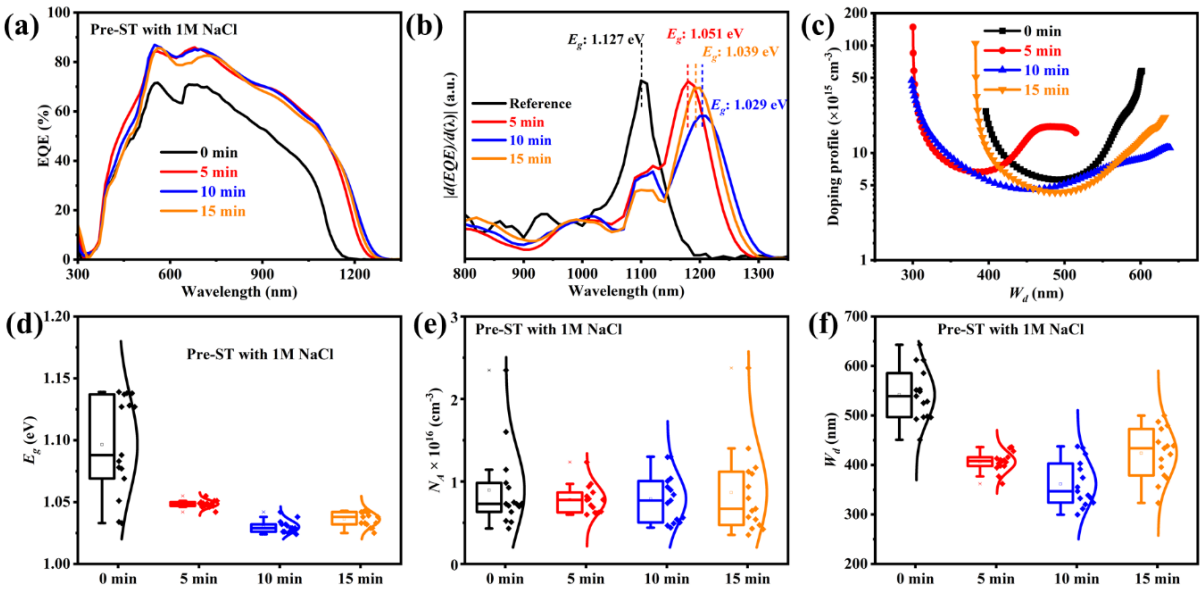

Figure 5.11: (a) EQE curves, (b) band gaps, and N_A-W_d profiles of the best efficient CISSe with various times pre-selenization treatment in 1 M NaCl solution. Statistical distribution of (d) E_g, (e) N_A, and (f) W_d derived from 15 CISSe devices with various times pre-selenization treatment in 1 M NaCl aqueous-ethanol solution.

The Na^+ will bond with Se vapor to form a Na_2Se_x (x >1) compound, which can assist the Se diffusion during the high-temperature selenization.[18, 36] Therefore, the substitution of S by Se in Na-treated CISSe absorber is higher than in the reference CISSe, leading to better CISSe absorber quality and better EQE response. Furthermore, smaller values of W_d arise in the NaCl treatment because the Na_{Cu} defect formations at the CISSe surface hinders the Cd^{2+} diffusion, reducing the width of the space charge region (Figure 5.11c).[21, 56, 103] N_A is affected by the amount of Na in the absorber and by its morphology.[56] With prolonging the precursor soaking time, N_A firstly increases then decreases, in accordance with literature results for solution-processed chalcopyrite solar cells.[32, 56]

The statistics E_g, N_A, and W_d are presented in Figure 5.11 and summarized in Table 5.3 and Table 5.4. After Na incorporation, all these electrical parameters (average values) are decreased. As above discussion, Na-treated CISSe have large CISSe grains and Se-rich composition, leading to fewer grain boundaries. In addition, the Na_{Cu} defects will form on the surface of absorbers. Therefore, all these electrical parameters in Na-treated CISSe are reduced.

Table 5.3: Photovoltaic performance parameters of CISSe solar cells with 1 M NaCl solution pre-selenization treatment for various times (15 sub-cells for each recipe).

Treatment time*	V_{oc} (mV)	J_{sc} (mA/cm^2)	*FF* (%)	*Efficiency* (%)	$N_A \times 10^{15}$ (cm^{-3})	W_d (nm)
Reference	379.0±18.3 403.5	27.5±2.0 26.9	47.5±3.8 53.0	4.9±0.4 5.8	9.0±4.9 6.3	542.1±53.1 552.4
5 min	479.1±8.6 468.4	30.5±1.7 32.0	57.0±2.4 58.7	8.3±0.3 8.8	7.8±1.7 9.7	406.2±19.7 434.4
10 min	457.7±9.7 464.5	33.4±1.0 33.4	60.9±1.1 62.0	9.3±0.2 9.6	7.9±2.9 4.6	361.6±45.9 437.5
15 min	451.1±15.2 459.9	29.7±1.7 31.6	36.9±2.5 42.3	5.0±0.6 6.2	8.7±5.3 4.3	423.7±51.2 487.4

* V_{oc}, J_{sc}, *FF*, *Efficiency*, N_A, and W_d are presented with (average ± standard deviation) calculated from 15 devices.

Alkali treatment can improve absorber quality and decrease carrier recombination, so that $V_{oc,def}$ is reduced significantly. Thanks to the increase in V_{oc} and the reduction of E_g after Na incorporation, the $V_{oc,def}$ values are remarkably reduced (Figure 5.12a). When the precursor films are subject to 10 min NaCl treatment, the average $V_{oc,def}$ values are more uniform than other treatment times. Based on these results, the CISSe solar cell can achieve the best efficiency by subjecting to 10 min Pre-ST. Without/with NaCl treatment CISSe solar cells present two slopes fitting in the high and low-temperature region (Figure 5.12). The difference between E_g and E_{a1} firstly decreases towards the minimum for 10 min NaCl treatment (0.007 eV) and subsequently increases (Table 5.4).

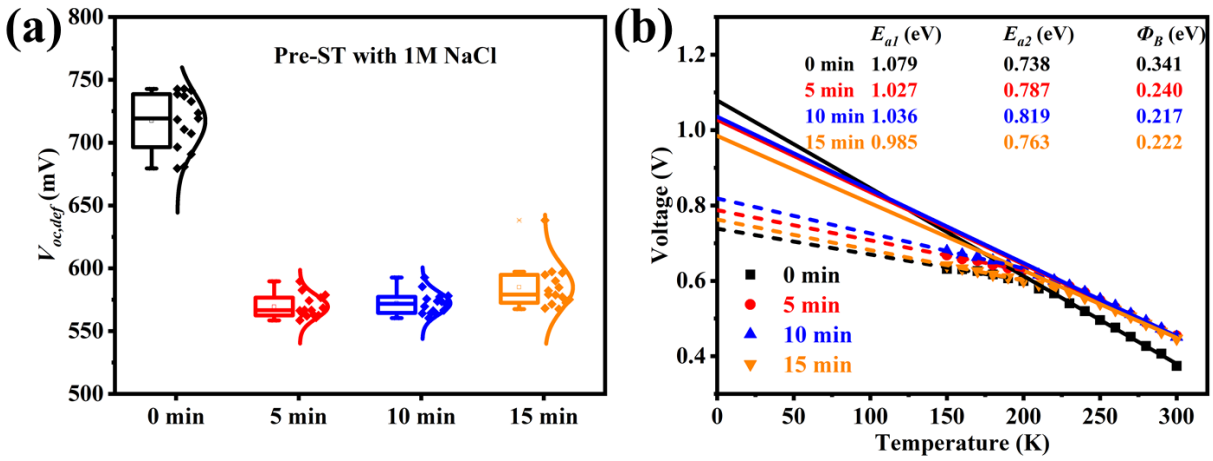

Figure 5.12: (a) The statistical distributions of $V_{oc,def}$, (b) Temperature-dependent open-circuit voltage of CISSe with various times pre-selenization treatment in 1 M NaCl solution.

Table 5.4: The electrical papameters of CISSe with various times pre-selenization treatment in 1 M NaCl solution.

Treatment time*	E_g (eV)	$V_{oc,def}$ (mV)	E_{a1} (eV)	E_{a2} (eV)	$\|E_g - E_{a1}\|$ (eV)	Φ_B (eV)
Reference	1.10±0.04 1.127	717.5±22.5 723.5	1.079	0.738	0.048	0.341
5 min	1.05±0.01 1.051	569.4±9.0 582.6	1.027	0.787	0.024	0.240
10 min	1.03±0.01 1.029	572.2±8.8 564.5	1.036	0.819	0.007	0.217
15 min	1.04±0.01 1.039	584.9±17.7 579.1	0.985	0.763	0.054	0.222

* E_g and $V_{oc,def}$ are presented with (average ± standard deviation) calculated from 15 devices.

These small differences between E_g and E_{a1} indicate that the dominant recombination occurs in the absorber bulk rather than the interface. The short soaking time can reduce the interface recombination significantly (5 min and 10 min), whereas the interface recombination becomes serious by further prolonging the soaking time (15 min). The back barrier height (Φ_B) is extracted from the difference between E_{a1} and E_{a2}. Compared to the reference CISSe, the Φ_B of the Na-treated CISSe can be significantly reduced, which is in good agreement with the results from the literature.[56] With prolonging the soaking time, the Φ_B initially decreases and then increases with the minimum for 10 min (217 meV) (Table 5.4). The *J-V*, *C-V*, and *JVT* results demonstrate that the best CISSe solar cell is obtained from 10 min soaking time.

5.2.3 The effect of NaCl concentrations

The concentration of the NaCl solution can strongly affect the CISSe solar cells properties.[58] The *J-V* curves of the best CISSe solar cells subject to Pre-ST in various concentrations of NaCl for 10 min are shown in Figure 5.13 and Table 5.5. Na incorporation can obviously improve the V_{oc}, J_{sc}, and *FF*, therefore, the efficiency is improved. The highest V_{oc} value is observed for 0.8 M NaCl, and the highest J_{sc} and *FF* for 1 M NaCl (Table 5.5), leading to the improvement in efficiencies. Therefore, the champion efficiency of 9.6% with a V_{oc} of 464.5 mV, a J_{sc} of 33.4 mA/cm^2, and a *FF* of 62.0% remains at 1 M NaCl Pre-ST for 10 min. With further increasing the NaCl concentration to 1.2 M, CISSe solar cells present lower V_{oc}, J_{sc}, *FF*, and efficiency than 1 M NaCl treatment (Figure 5.13a).

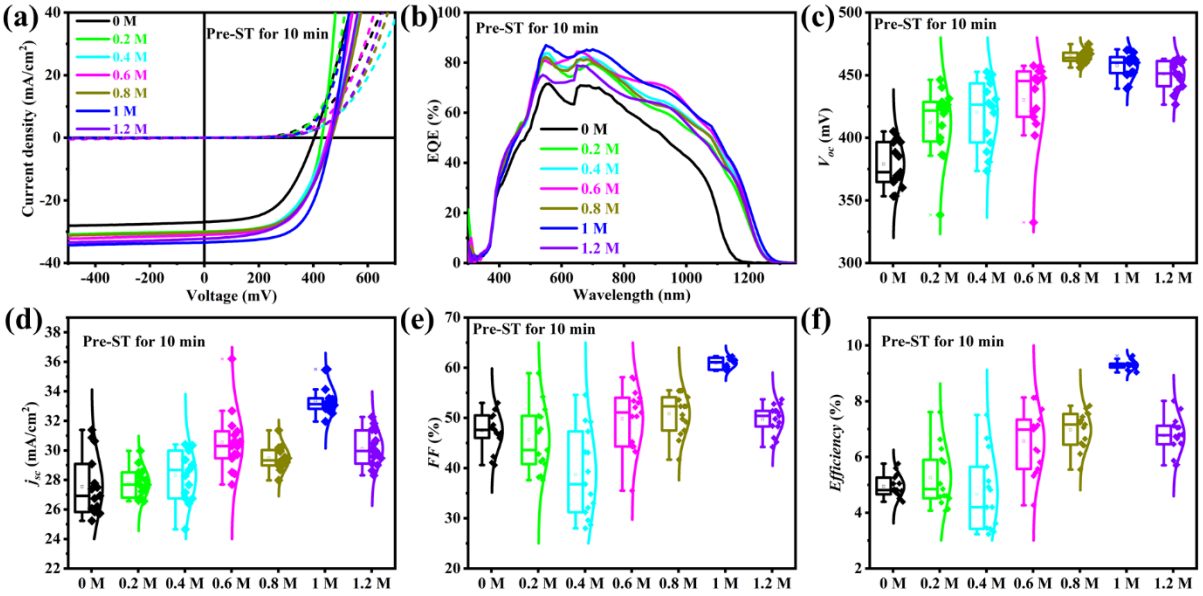

Figure 5.13: (a) *J-V* curves, (b) EQE curves. Statistical distribution of (c) V_{oc}, (d) J_{sc}, (e) *FF*, and (f) efficiency of CISSe with various NaCl concentrations for 10 min pre-selenization treatment.

The EQE curves of these CISSe solar cells with various concentrations of NaCl for 10 min Pre-ST significantly improve in the wavelength range above 400 nm compared to the Na-free reference (Figure 5.13b). A possible reason may be a better CISSe absorber quality with fewer defects after Na incorporation, leading to better photoelectric response and the separation of photo-generated hole-electron pairs.[56, 58] It is one of the explanations for J_{sc} improvement obtained from the *J-V* measurement.

Compared to the reference CISSe solar cells, Na-treated CISSe solar cells present higher EQE responses and narrower E_g values (Figure 5.14a and Table 5.5). These results are similar to the results of precursor films with various soaking times in 1 M NaCl solution (Figure 5.11). The solar cell with 1 M NaCl treatment exhibits over 20% (on average) higher EQE (400-1000 nm) and the maximum EQE value achieves 88.7% at 550 nm wavelength. Simultaneously, the Na-treated CISSe absorbers have higher EQE responses at wavelengths above 1020 nm than the reference CISSe (Figure 5.13b). These results are in good agreement with the outstanding J_{sc} of 1 M NaCl Pre-ST CISSe solar cells (Table 5.5).

The statistics of the PV parameters of these CISSe solar cells are shown in Figure 5.13c-f. They exhibit similar trends with the corresponding best solar cells. The V_{oc}, J_{sc}, *FF*, and efficiency are significantly improved for the Na-treated CISSe. The maximum average J_{sc}, *FF*, and efficiency are obtained for the CISSe with 1 M NaCl for Pre-ST. These results are in good agreement with the literature report.[56]

Na-treated CISSe solar cells present narrower E_g values than the reference CISSe owing to the Na_2Se_x-assisted (x >1) crystallization during the selenization (Figure 5.14a). Compared to the reference CISSe solar cells, the average values of N_A firstly increase until the NaCl concentration reaches 0.2 M and then decrease for higher NaCl concentration (Figure 5.14b and Table 5.5). On the contrary, once Na is applied in the CISSe absorber, the W_d values are remarkably reduced. These results can be explained by the formation of Na_{Cu} defect on the surface, which will reduce the Cu vacancies and limit the Cd_{Cu} defect formation during the CdS layer deposition.

Na incorporation is beneficial for the Se diffusion owing to the formation of Na_2Se_x (x >1) compound. Additionally, the Na-treated CISSe can obtain better absorber quality. Therefore, the average E_g values of Na-treated CISSe become more uniform and are smaller than the reference CISSe (Figure 5.14c). Compared to the reference CISSe solar cells, the average values of N_A firstly increase until the NaCl concentration reaches 0.2 M and then decrease with increasing the NaCl concentration (Figure 5.14d). In contrast, NaCl-treated CISSe solar cells have a narrower W_d than the reference CISSe solar cells (Figure 5.14e and Table 5.5). After Na incorporation, the $V_{oc,def}$ values are in general significantly reduced owing to better CISSe absorber quality (Figure 5.14f and Table 5.5). These smaller $V_{oc,def}$ values in the Na-treated can be attributed to the narrower E_g and larger V_{oc} values in the Na-treated CISSe rather than in the reference CISSe. In sum, the highest efficient CISSe solar cells are fabricated from the solution-processed precursor films with 1M NaCl aqueous-ethanol solution Pre-ST for 10 min.

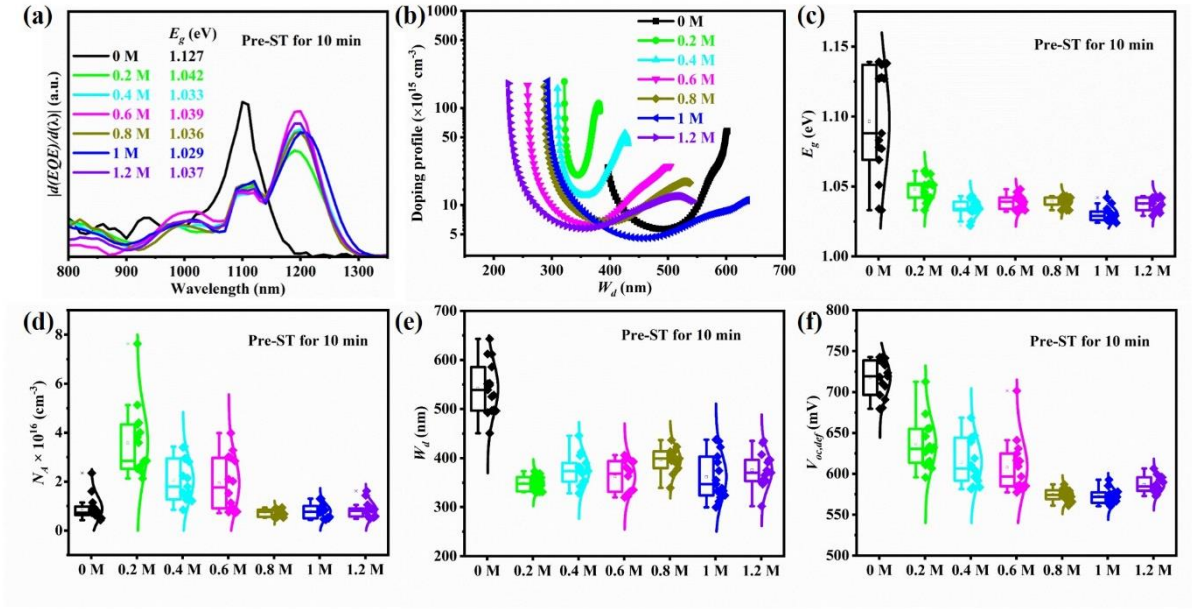

Figure 5.14: (a) E_g and (b) C-V characterization of the best CISSe solar cells with various concentration NaCl treatment. Statistical distribution of (c) E_g, (d) N_A, (e) W_d, and (f) $V_{oc,def}$ of CISSe with various NaCl concentrations for 10 min pre-selenization treatment.

Table 5.5: Photovoltaic performance parameters of CISSe solar cells with various concentration of NaCl solution pre-selenization treatment for various times (15 sub-cells for each recipe).

NaCl concentration	V_{oc} (mV)	J_{sc} (mA/cm^2)	*FF* (%)	*Efficiency* (%)	E_g (eV)	$V_{oc,def}$ (mV)	$N_A \times 10^{15}$ (cm^{-3})	W_d (nm)
Reference	379.0±18.3 403.5	27.5±2.0 26.9	47.5±3.8 53.0	4.9±0.4 5.8	1.10±0.04 1.127	717.5±22.5 723.5	9.0±4.9 6.3	542.1±53.1 552.4
0.2 M	412.2±27.4 431.3	27.8±1.0 30.0	45.7±6.4 58.9	5.3±1.0 7.6	1.05±0.01 1.042	596.3±29.4 610.7	35.8±14.6 28.5	349.8±14.6 360.2
0.4 M	420.3±25.9 452.6	28.3±1.7 30.4	38.7±8.6 54.6	4.7±1.4 7.5	1.03±0.01 1.034	580.0±27.7 581.4	20.6±8.6 15.6	374.8±30.3 380.9
0.6 M	430.3±32.4 453.0	30.5±2.0 31.1	49.8±6.2 57.8	6.6±1.1 8.1	1.04±0.01 1.039	570.1±32.9 586.0	19.3±11.2 7.13	352.8±48.6 393.6
0.8 M	464.8±4.9 467.1	29.5±0.8 30.3	50.8±4.0 55.5	7.0±0.7 7.8	1.04±0.01 1.036	538.7±7.1 568.9	7.3±1.5 6.7	396.6±24.2 399.1
1 M	457.7±9.7 464.5	33.4±1.0 33.4	60.9±1.1 62.0	9.3±0.2 9.6	1.03±0.01 1.029	572.2±8.8 564.5	7.9±2.9 4.6	361.6±45.9 437.5
1.2 M	450.8±11.5 462.3	30.1±1.2 32.3	49.7±2.9 53.7	6.8±0.7 8.0	1.04±0.01 1.037	586.7±9.7 574.7	8.5±3.2 5.8	375.2±34.9 370.2

* All the parameters are presented with (average ± standard deviation) calculated from 15 devices.

6 Fabrication of $CuIn(S,Se)_2$ solar cells on ITO back contact

This chapter is in part based on the following publication:

Yao Gao, Guanchao Yin, Yong Li, Tristan Köhler, Jan Lucaßen, Martina Schmid. 8.0% Efficient Submicron $CuIn(S,Se)_2$ Solar Cells on $Sn:In_2O_3$ Back Contact via a Facile Solution Process. ***ACS Applied Energy Materials***, 2022, 5, 12252-12260 (DOI: 10.1021/acsaem.2c01764). As the first author of this manuscript, I conceived the idea and fabricated all the devices, conducted the measurements, performed the data analysis and prepared the manuscript.

6.1 Motivation

Generally, molybdenum (Mo) is employed as a back contact of high-efficiency CIGSe solar cells because a $MoSe_2$ interlayer between Mo back contact and CIGSe absorber will form during the absorber growth process and lead to a quasi-Ohmic contact.[37] However, due to the poor back reflectivity of the CIGSe/Mo interface, ultra-thin (around 500 nm) CIGSe solar cells suffer from dramatic optical losses. In addition, the opacity of the Mo back-contact limits their application in bifacial and semi-transparent structures.[13] Therefore, replacing opaque Mo with a transparent conductive oxide (TCO) as the back electrode is a promising research topic. In previous reports, Al:ZnO (AZO) and $Sn:In_2O_3$ (ITO) have been used to replace the Mo back contact of CIGSe solar cells fabricated via a high vacuum co-evaporation process.[14, 43, 55, 110] However, co-evaporation deposition is an expensive fabrication technique requiring a high vacuum environment. Therefore, the exploitation of a cost-effective and convenient process for CIGSe solar cell fabrication is crucial.

Jiang et al. generated solar cells with *PCEs* of 14.5 % for $CuInSe_2$ and 15.2 % for $Cu(In,Ga)Se_2$ solar cells with 1.2 µm absorbers.[36] These were obtained via a solution-based spin-coating process with metal-chloride DMF precursor, indicating that metal-chloride DMF as precursor solution shows high potential in CIGSe-based solar cell fabrication.[36-39, 100] A CIGSe device with an efficiency of 13.8% was achieved successfully via an all solution-processed fabrication (except the Mo back contact).[106] Barange et al. reported 5.68% efficiency of $Cu(In,Ga)S_2$ on ITO back contact via a sol-gel solution spin-coating process.[111] Sousa et al. reported 6.1 % efficiency for $Cu(In,Ga)Se_2$ on FTO back contact via a screen-printing process. However, the solar cells properties exhibited poor homogeneity.[12]

6.2 Results

6.2.1 Effect of selenization temperature on solar cell performance

It is reported that the electrical and optical performance of ITO back contacts can be improved by annealing. The ITO back contacts are subject to a heating treatment at 350℃ for 10 min in the air before spin-coating the precursor solution. The sheet resistances and optical properties are shown in Figure 6.1. When the ITO back contact is subject to annealing, the sheet resistance of the 400 nm-thick ITO firstly increases and then decreases (Figure 6.1a). Lower sheet resistances of the annealed ITO back contacts can be attributed to the improvement of carrier mobility. Annealing in air can improve the crystallization of ITO thin films, leading to the improvement of the free carrier mobility. Simultaneously, the annealing treatment can reduce the disordered grain boundaries, resulting in the reduction of the electron scattering. ITO thin films have a large number of oxygen vacancies, which can be passivated by the incorporation of oxygen during the annealing in air.

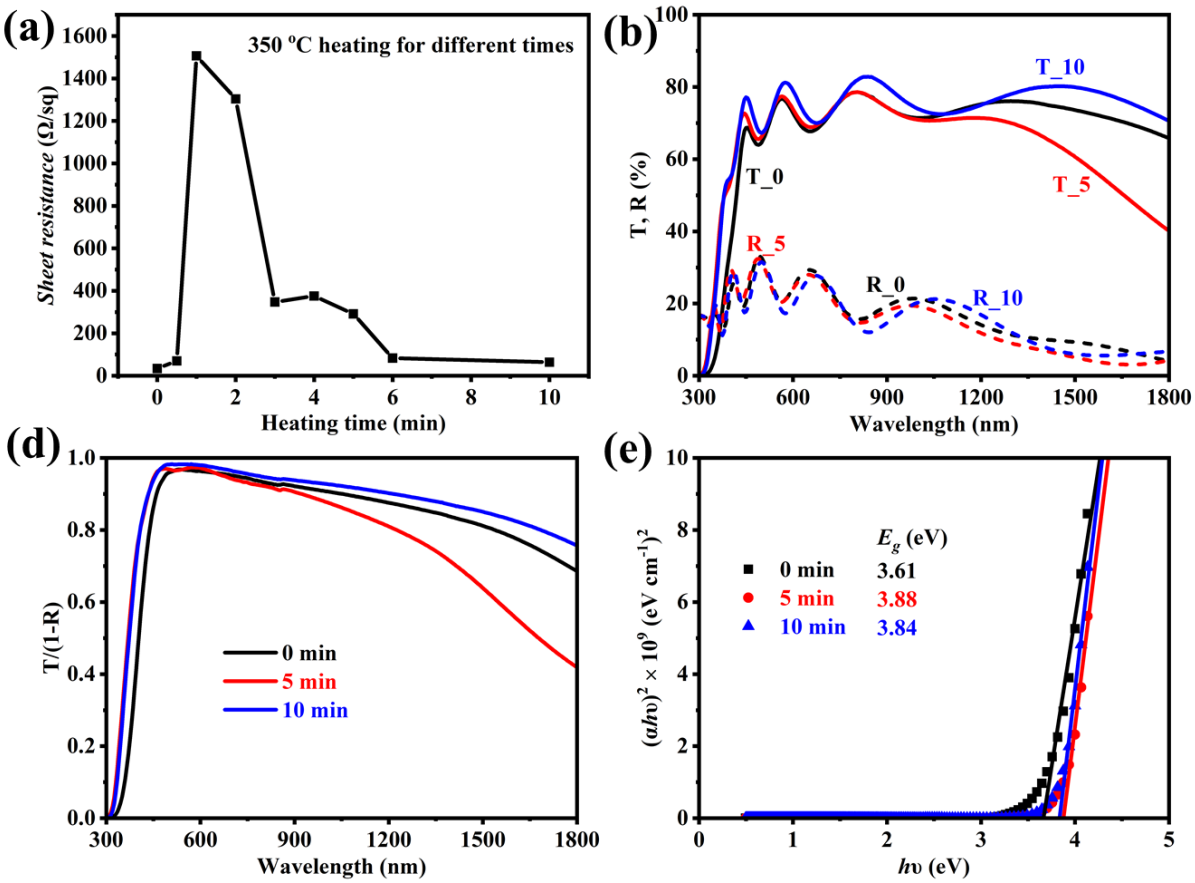

Figure 6.1: (a) sheet resistance, (b) transmission and reflection properties, (c) T/(1-R) ratios, and (d) band gap of ITO back contact with annealing at 350℃ for various times.

The optical properties of ITO thin films with various annealing times are shown in Figure 6.1b-d. After 10 min annealing treatment, an increase in the transmission of 400 nm-thick ITO thin films is observed. Simultaneously, the free-carrier absorption can be significantly reduced after 10 min annealing. This result originates from the annihilation of defects in the ITO thin film during a 10 min annealing. The T/(1-R) ratio of 10 min annealing ITO in the sub-bandgap energy range is smaller than the reference and after 5 min annealing ITO, indicating that the thin ITO film after 10 min annealing has a lower density of defects due to a high crystallinity. Additionally, the band gaps (E_g) of annealed ITO thin films are larger than the reference thin films.

Figure 6.2a shows the GIXRD patterns of ultra-thin CISSe thin film solar cells with the absorber layers selenized at different temperatures. The positions of Bragg reflections at 26.9°, 44.7°, and 53.1° correspond to the (112)/(103), (204)/(220), and (116)/(312) planes of chalcopyrite, respectively.[36-37] Since the radius of the selenium atom is larger than that of sulfur, the positions of these Bragg reflections are right shifted compared to pure $CuInSe_2$ and left-shifted compared to pure $CuInS_2$. Bragg reflections located at 30.5º and 50.9º are attributed to the ITO back contact. Additionally, the Bragg reflections pointing to the ZnO window layer are observed at 34.4º, 36.2º and 47.6º. When the selenization is carried out at T = 500°C, additional Bragg reflections of ITO at 35.4º and 60.7º appear.

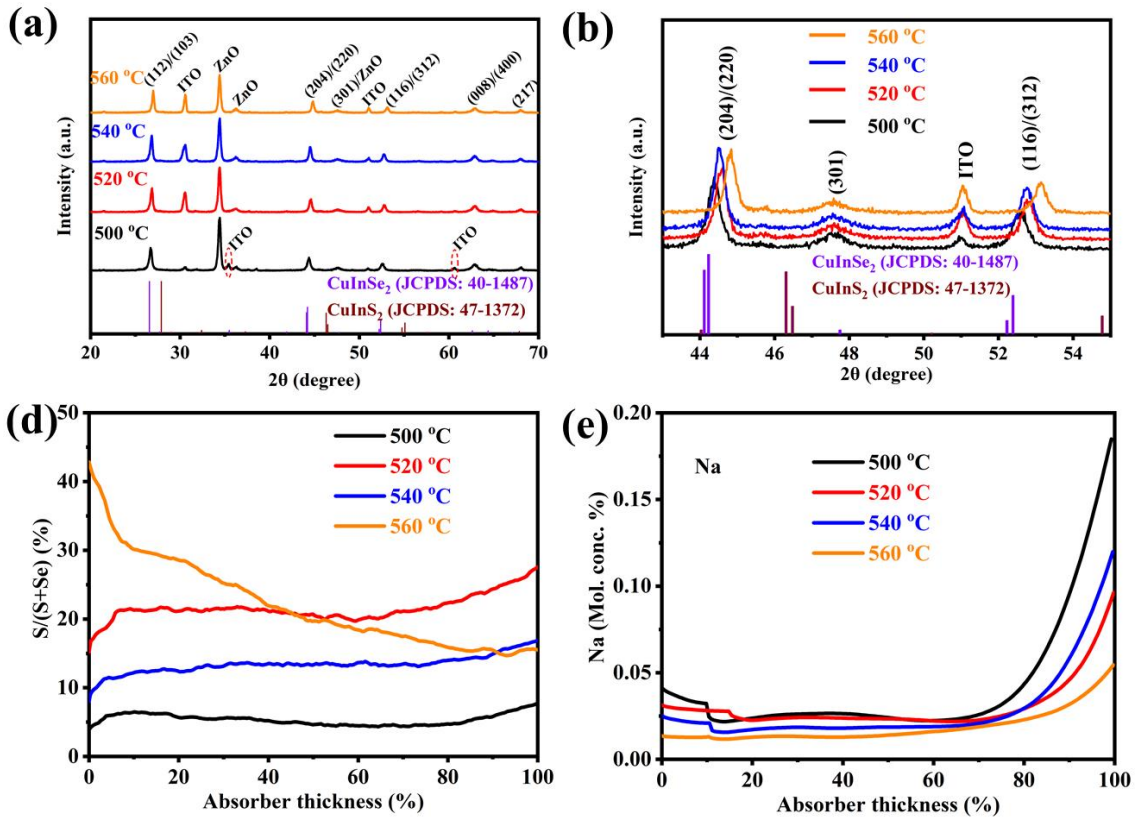

Figure 6.2: (a) and (b) XRD pattern of the CISSe solar cell devices selenized at different temperatures; (c) S/(S+Se) ratios and (d) Na content of absorber layers measured by GDOES.

Compared to T = 500°C, the XRD diffraction patterns for absorbers selenized at $T \geq$ 520°C show a slight right shift (Figure 6.2b), especially at high diffraction angles where the shift of the Bragg reflections is more pronounced. These results indicate that the as-prepared absorber layers at $T \geq$ 520°C have a higher S/(S+Se) ratio, which is confirmed by XRF measurement and shown in Table 6.1. However, for the CISSe absorber obtained at 540°C, the shift of XRD patterns is not as obvious as for the absorbers at T = 520°C and T = 560°C. This observation is also in agreement with a lower S/(S+Se) ratio, see Table 6.1.

The S/(S+Se) depth profiles of the CISSe absorbers are measured via GDOES and are shown in Figure 6.2c. With increasing the selenization temperature above 500°C, the content of S increases. It is indicated that the process of selenization suppresses the evaporation of S at higher temperatures with increasing Se pressure, inhibiting the replacement of Se by S. When $T \leq$ 540°C, the S content at the CISSe back interface is higher than at the front surface. In addition, when T = 540°C, the content of S is lower than for T = 520 and T = 560°C, which is in agreement with the position of the XRD peaks (Figure 6.2b). However, when increasing the temperature to T = 560°C, the opposite dependency is observed regarding the S/(S+Se) ratio. There is a factor of two higher S content at the front compared to the back interface. This observation may be explained by large grains in the CISSe layer forming rapidly under high Se pressure at high temperatures. However, the S of the precursor film will be removed by migration toward the front surface along the grain boundary of this large-grained layer, leading to inhomogeneous grains at the front interface of the CISSe absorber (Figure 6.3d). The near front surface consists of large CISSe grains and an aggregation of small CISSe grains. Large CISSe grains form at the rear interface of the CISSe absorber. In general, the grain size of CISSe with a Se-rich composition is larger than the S-rich CISSe.[37] Therefore, a higher S/(S+Se) ratio is observed at the front surface decreasing towards the rear interface. The GDOES results are in good agreement with XRD and XRF measurements (Table 6.1).

The Na concentration profile exhibits a similar trend for these solar cells (Figure 6.2d). A high Na content exists near the back interface, then it decreases towards the front surface. A high selenization temperature can promote the diffusion of Na from the substrate to the absorber layer. However, with increasing selenization temperature, the Na content of the absorber decreases in our experiments (Figure 6.2d).

Table 6.1: Composition of ultra-thin absorbers obtained for different selenization temperatures measured by XRF.

	Cu (at%)	In (at%)	Se (at%)	S (at%)	Cu/In	S/(S+Se)
500°C	21.63	28.52	47.36	2.12	0.76	0.04
520°C	19.50	25.32	35.23	19.62	0.77	0.36
540°C	20.60	26.08	39.74	13.19	0.79	0.25
560°C	18.04	23.83	25.86	31.92	0.76	0.55

The reason may be the removal of Na near the surface during the KCN etching and the CdS deposition process. Sodium can stay at the grain boundary and in the grain interior.[112] The higher Na content for 500℃ selenization temperature is attributed to its significantly smaller grains and higher density of grain boundaries.[36]

The cross-section scanning electron microscopy (SEM) images of the CISSe devices with varied selenization temperatures are shown in Figure 6.3. For T = 500℃, the CISSe absorber shows a double-layer structure with a thick sub-layer of fine grains at the bottom and a very thin layer with large columnar grains on top, implying that the low selenization temperature is disadvantageous to CISSe grain growth. When the selenization temperature increases to T = 520℃, larger grains of around 300 - 500 nm in size are observed. However, voids still exist in the absorber layer and at the back contact interface.

The largest CISSe grains with diameters around 500 - 650 nm form when the precursor film selenization is carried out at 540℃. In this case, the large grains of the absorber layer are densely packed, almost absent of voids. When the selenization temperature increases to 560℃, a CISSe absorber layer with a triple-layer structure is observed: large grains at the bottom and on top, and fine grains in the middle.

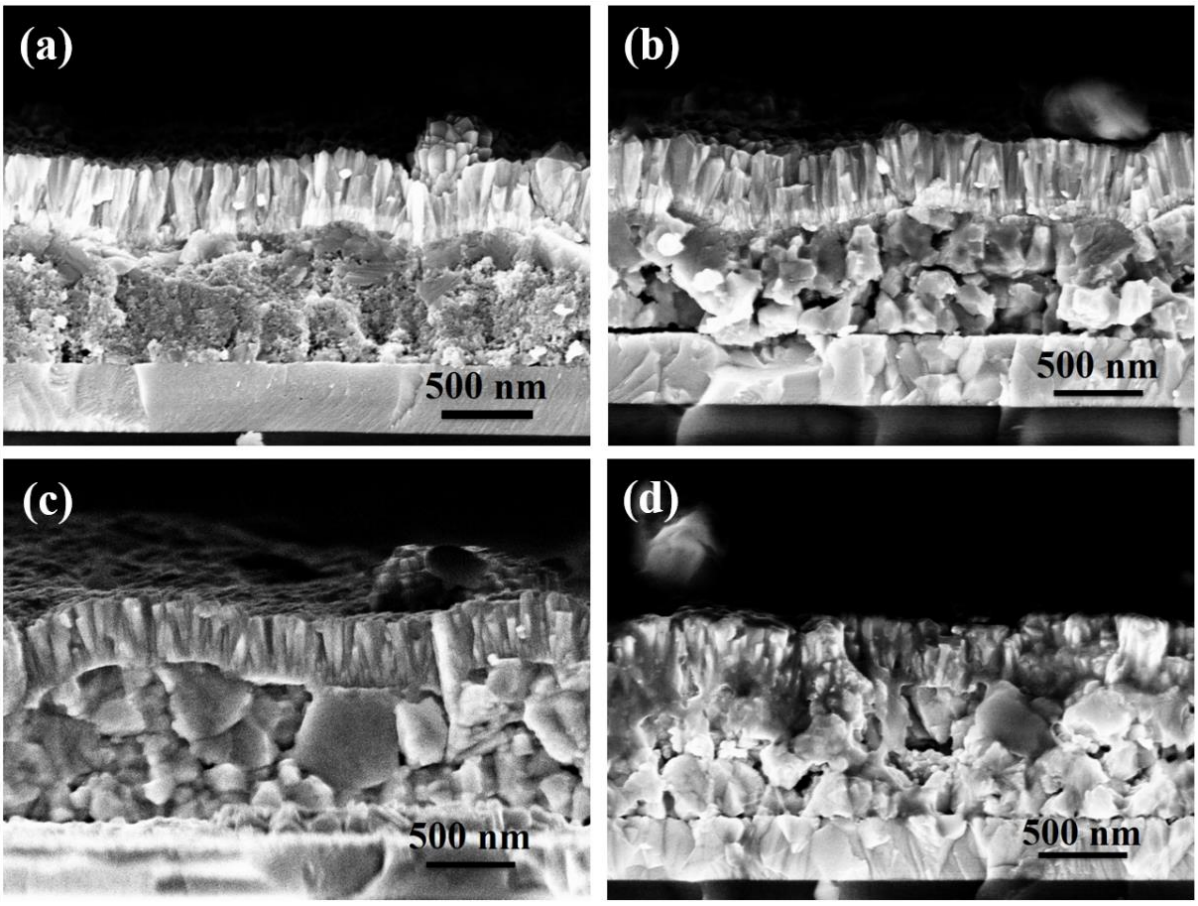

Figure 6.3: SEM images of as-prepared CISSe devices under different selenization temperatures, (a) 500℃, (b) 520℃, (c) 540℃, and (d) 560℃.

However, the top layer consists of large CISSe grains and an aggregation of small CISSe grains (Figure 6.3d). This inhomogeneous microstructure can be ascribed to the inhomogeneity in element distribution. A large amount of liquid Se penetrates the whole film under high Se vapor pressure, and Se bonds with Cu to form $Cu_{2-x}Se$, which facilitates the formation of large grains and denser films.[36, 56]

Figure 6.4a shows the *J-V* curves of the best CISSe solar cells under AM 1.5G illumination, and the corresponding PV parameters are summarized in Table 6.2. When the selenization is carried out at T = 500℃, the CISSe solar cell is achieved a maximum power conversion efficiency (*PCE*) of 4.8% with a short-circuit current density J_{sc} of 24.8 mA/cm^2, an open-circuit voltage V_{oc} of 384.1 mV, and a fill factor (*FF*) of 50.3% is achieved. The *PCE* at T = 520℃ is remarkably increased to 7.5%. The efficiency improvement can be explained by the better crystallinity at high temperatures. However, when the selenization temperature increases to T = 540℃ and T = 560℃, the *PCEs* decrease to 6.6%, and 5.9%, respectively. The same trend can also be observed in J_{sc} and *FF*, the highest J_{sc} of 27.6 mA/cm^2 and *FF* of 56.1% are obtained at 520℃. However, the highest V_{oc} value of 492.2 mV is achieved when the selenization temperature increases to 560℃. The higher V_{oc} can be attributed to a better crystallinity and a higher content of S observed at higher selenization temperatures. Simultaneously, due to the wider band gap of the CISSe absorber with higher S content, J_{sc} is lowered.[29, 37]

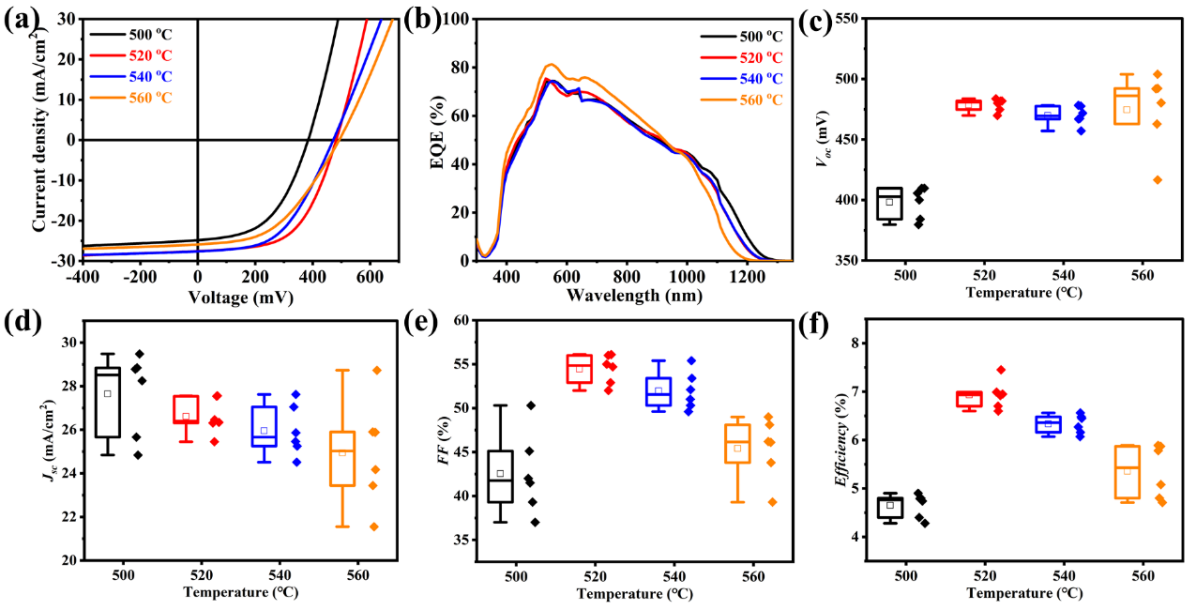

Figure 6.4: (a) *J-V* curves of the best CISSe devices with different selenization temperature. The distribution (each sample contained 6 cells) of (b) V_{oc}, (c) J_{sc}, (d) *FF*, and (e) *PCE*. (f) EQE of the best CISSe devices.

The PV parameters of CISSe solar cells are summarized in Table 5.2. As shown in Figure 6.4c, the V_{oc} of the solar cells increases with increasing selenization temperature. However, when the precursor films are selenized at T = 540°C, the V_{oc} of the corresponding solar cells slightly decreases (Table 6.2). This variation tendency of V_{oc} can be related to the content of S in the CISSe absorbers (Table 6.1). Increasing the selenization temperature results in the decrease of J_{sc} (Figure 6.4d) because the CISSe absorber has a wider band gap at high selenization temperatures due to the increase of S content (Table 6.1). Both *FF* and *PCE* increase with increasing selenization temperature to T = 520°C and then decrease with further increasing selenization temperature (Figure 6.4e and 6.4f). These results indicate that 520°C selenization temperature is favourable for fabricating high-quality CISSe absorbers on ITO back contacts for semi-transparent CISSe solar cells applications.

The series resistance (R_s) values of the samples are calculated from the plots of dV/dJ *vs.* $(J+J_{sc})^{-1}$ (Figure 6.5 and Table 6.2). With increasing selenization temperature, R_s increases from 1.7 Ω cm^2 (for 500°C) to 2.2 Ω cm^2 (for 520°C), 4.3 Ω cm^2 (for 540°C), and 5.8 Ω cm^2 (for 560°C), respectively. The enhancement of R_s with increasing absorber selenization temperature ascribes to the formation of a thin In_2O_3 layer at the CISSe/ITO interface during the high-temperature selenization owing to the low standard molar enthalpy of In_2O_3.[113] This high-resistance layer will limit the fast separation and transportation of photo-generation carriers, which is not beneficial to achieve high-efficient CISSe solar cells.

Table 6.2: Corresponding photovoltaic characteristics of average and the best solar cell parameters of CISSe grown on ITO back contact at various selenization temperatures.

Temperature*	V_{oc} (mV)	J_{sc} (mA/cm^2)	*FF* (%)	*PCE* (%)	R_s (Ω cm^2)
500°C	398.1±13.1 384.1	27.6±1.9 24.8	42.5±4.7 50.3	4.7±0.2 4.8	1.7
520°C	478.6±5.3 481.7	26.6±0.8 27.6	54.5±1.7 56.1	6.9±0.3 7.5	2.2
540°C	469.8±7.9 471.7	26.0±1.2 27.6	52.0±2.2 50.3	6.3±0.2 6.6	4.3
560°C	474.6±31.6 492.2	24.9±2.5 25.9	45.4±3.5 46.1	5.4±0.6 5.9	5.8

* Efficiency, V_{oc}, J_{sc}, and *FF* are presented with (average ± standard deviation) calculated from 6 devices.

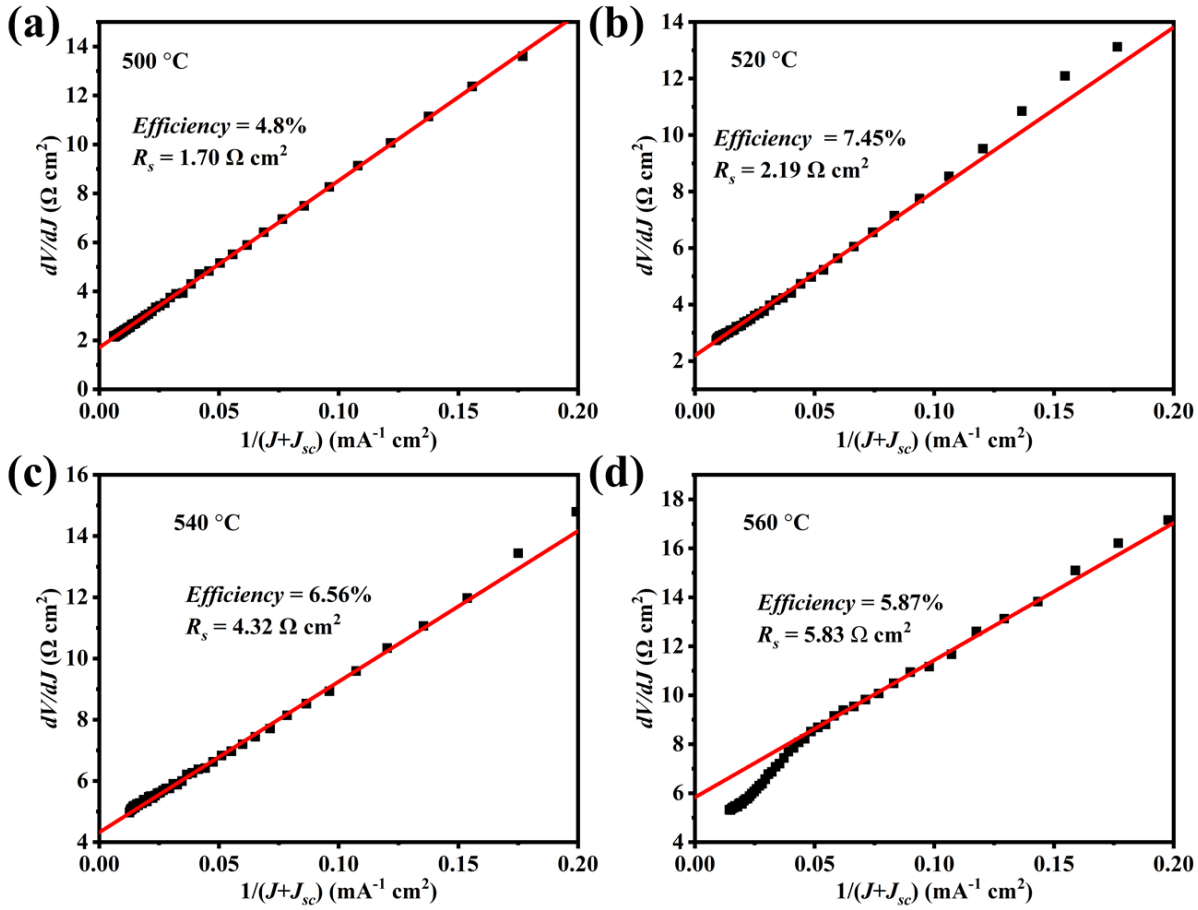

Figure 6.5: The series resistances of CISSe solar cells with absorbers selenized at various temperatures.

The external quantum efficiency (EQE) spectra of the best devices are shown in Figure 6.4b. These EQEs are higher than 65% in the visible wavelength range and the intensity of the EQE response surpasses 75%. However, the EQE results are relatively low because of the thin absorber layer (550 nm). The device obtained with the absorber selenized at T = 560°C shows a higher EQE in the range of 380 - 950 nm wavelength compared to the samples of other annealing temperatures. However, the EQE drops rapidly when the wavelength is longer than 1000 nm, owing to a higher content of S in the absorber (Table 6.1). The EQE spectra of all devices are overlapping in the range of 300 - 380 nm, which can be explained by the absorption of the CdS/i-ZnO/AZO layers.[55]

The band gaps of these CISSe devices are extracted from the $[E\times\ln(1\text{-}EQE)]^2$ *vs.* energy plots and are shown in Figure 6.6a. With increasing selenization temperature, wider band gaps are observed. When T = 500°C, a 1.04 eV of band gap is obtained. With increasing selenization temperature to T = 520°C and T = 540°C, similar band gap values (1.07 eV for 520°C and 1.08 eV for 540°C) are observed from EQE calculation results. The widest band gap of 1.11 eV for these samples is achieved for T = 560°C. These results are in good agreement with the V_{oc} improvement at higher selenization temperatures as compared to T = 500°C.

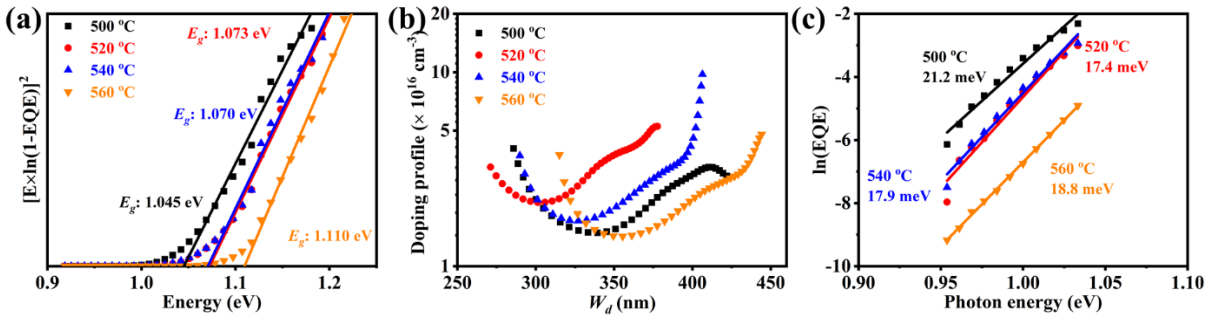

Figure 6.6: (a) Band gaps of the devices calculated from EQE data. (b) charge carrier density and depletion width derived from *C-V* curves. (c) ln(EQE) *vs.* photon energy at the long-wavelength edge to determine the E_U values for CISSe devices with different selenization temperatures.

The carrier concentration (N_A) *vs.* depletion width (W_d) profiles are calculated from *C-V* curves (Figure 6.6).[55] N_A of 1.5×10^{16} cm^{-3} and W_d of 345.3 nm are obtained from the CISSe absorber selenized at 500°C. When the selenization temperature increases to 520°C, the N_A increases to 2.3×10^{16} cm^{-3} and the W_d decreases to 323.1 nm, respectively. However, with further increasing selenization temperature, the N_A decreases from 2.3×10^{16} cm^{-3} (T = 520°C) to 1.9×10^{16} cm^{-3} (T = 540°C) and 1.6×10^{16} cm^{-3} (T = 560°C). Correspondingly, W_d increases from 323.1 nm (T = 520°C) to 347.1 nm (T = 540°C) and 377.5 nm (T = 560°C), respectively. It is reported that the high-quality CIGSe-based solar cells have a high carrier concentration and a related narrow depletion width.[56, 75] Correspondingly, the highest values of performance parameters are obtained for devices selenized at 520°C.

The Urbach energy (E_U) can affect the carrier mobility and lifetime of the solar cells.[78-79] Figure 6.6c shows the relation of ln(*EQE*) *vs.* photon energy at the long-wavelength edge (1200 - 1300 nm). The E_U decreases from 20.2 meV (T = 500°C) to 17.4 meV (T = 520°C) with a related increase in *PCE* from 4.8% to 7.5%, because the enlargement of CISSe grain size is obtained at T = 520°C, leading to good absorber quality.[79] However, when the selenization temperature continues to increase, E_U increases to 17.9 meV (T = 540°C) and 18.8 meV (T = 560°C), respectively. It indicates that an even higher temperature is not beneficial for preparing high-efficiency CISSe solar cells on ITO back contact. Conclusively, the best solar cells properties are achieved for selenization at T = 520°C. Therefore, this temperature is used for further research.

6.2.2 Effect of absorber thickness

The absorber thickness can strongly affect the solar cell properties.[13] Thinner absorber layers result in low cost because they reduce materials' consumption and increase production throughput. However, the efficiency of thin absorbers is limited by electrical and optical losses,

such as increased recombination at back contact and reduced light absorption.[5, 41, 43, 91-92] As shown in the previous section, the best solar cells properties can be obtained from absorbers selenized at 520℃, thus T = 520℃ will be used for investigating the effect of absorber thickness.

Three different absorber thicknesses are investigated: 550 nm (ultra-thin absorber), 740 nm (sub-micron absorber), and 1440 nm (micron absorber). The best device with a sub-micron CISSe absorber exhibits an efficiency of 7.9%, which is 0.4% (abs.) higher than the ultra-thin CISSe device (Figure 6.7a). However, ultra-thin CISSe shows a higher V_{oc} of 481.7 mV compared to 445.6 mV for the sub-micron CISSe, whereas the opposite trend is observed for J_{sc} and FF. Previous reports have proven that the fabrication of thick absorbers via a solution process will lead to carbon residuals and voids at the rear interface between the absorber and the back contact.[31] These defects located at the rear interface will increase the recombination and result in a lower V_{oc}.

The increase in J_{sc} of sub-micron solar cells can be attributed to higher light absorption due to the thicker absorber (Figure 6.7a). CISSe solar cells with micron absorber show inferior properties and poor uniformity, the highest PCE of these devices is 1.8% (Figure 6.7f and Table 6.3). V_{oc}, J_{sc}, and FF are significantly reduced to 376.0 mV, 16.4 mA/cm^2 and 29.8%, respectively. These absorbers also easily peel off from the ITO back contact.

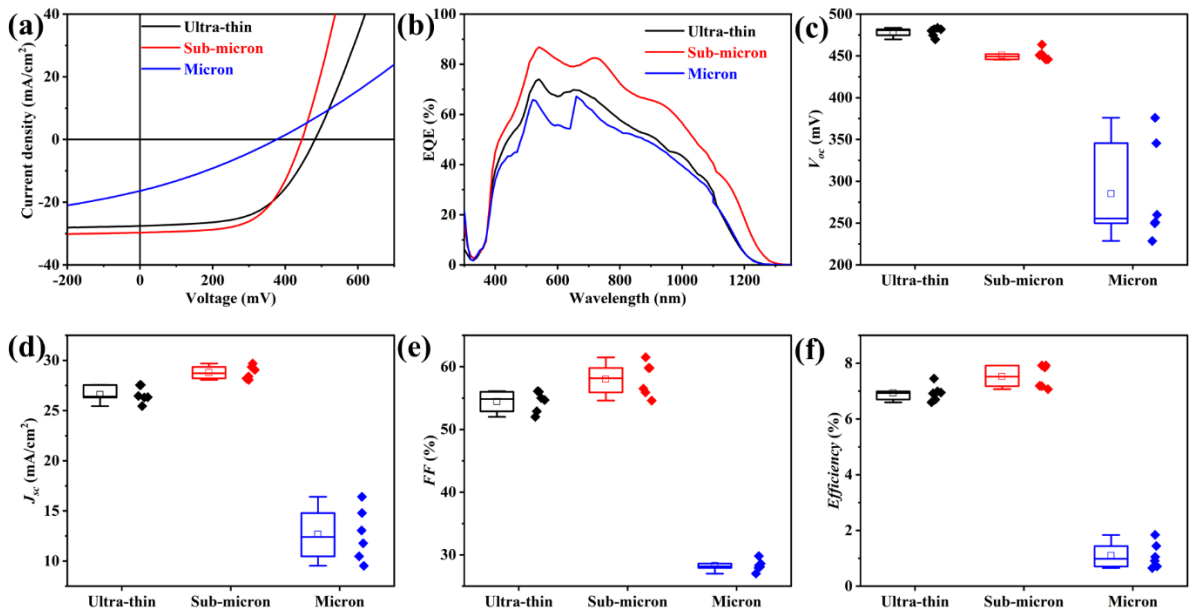

Figure 6.7: (a) J-V and (b) EQE curves of the best CISSe devices with different absorber thicknesses grown on ITO back contact. The distribution of (c) V_{oc}, (d) J_{sc}, (e) FF, and (f) PCE of the best CISSe devices.

Table 6.3: Averaged (over six devices) and the best CISSe photovoltaic device parameters for various absorber thicknesses.

Sample*	V_{oc} (mV)	J_{sc} (mA/cm^2)	*FF* (%)	*PCE* (%)	R_s (Ω cm^2)
Ultra-thin CISSe	478.6±5.3 481.7	26.6±0.8 27.6	54.5±1.7 56.1	6.9±0.3 7.5	2.2
Sub-micron CISSe	448.5±2.6 445.6	29.1±0.6 29.7	56.3±3.2 59.8	7.3±0.4 7.9	1.1
Micron CISSe	285.2±60.3 376.0	12.7±2.6 16.4	28.3±0.9 29.8	1.1±0.4 1.8	8.1

* Efficiency, V_{oc}, J_{sc}, and *FF* are presented with (average ± standard deviation) calculated from 6 devices.

With increasing absorber thickness, the EQE first increases and then decreases with the maximum EQE response observed for the sub-micron CISSe solar cells. The improvement of EQE in sub-micron CISSe device can be attributed to the increase in absorption of the incident light. However, the inferior adhesion between micron CISSe and ITO back contact results in the reduction of EQE response. The highest V_{oc} (average) is obtained from the ultra-thin CISSe solar cells (Figure 6.7c), which can be attributed to a larger band gap (Figure 6.7b). The J_{sc}, *FF*, and *PCE* present a similar tendency with the maximum average values observed for the sub-micron CISSe solar cells (Figure 6.7d-f and Table 6.3).

The series resistance decreases from 2.2 Ω cm^2 for ultra-thin absorber to 1.1 Ω cm^2 for sub-micron absorber and then increases to 8.1 Ω cm^2 for the micron absorber (Figure 6.8 and Table 6.3). As the adhesion to the ITO back contact may become a challenge for thick absorbers and the best efficiency of CISSe solar cells on ITO was obtained for sub-micron absobers, these are utilized for further research.

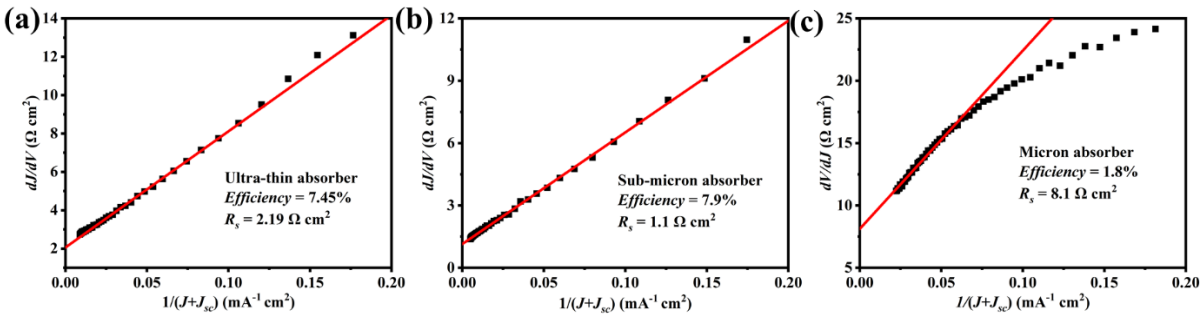

Figure 6.8: The series resistance of CISSe solar cells with various thickness of absorbers.

6.2.3 Effect of NaCl concentration for solar cell performance

Indeed, compared to the ultra-thin absorber, increasing the absorber thickness to the sub-micron level (740 nm) can improve the CISSe solar cell properties. However, a lower V_{oc} is obtained for the thicker absorber. It is known that Na incorporation can significantly increase the V_{oc} of CIGSe-based solar cells.[56, 60] Various concentrations of NaCl solution are utilized for the pre-selenization treatment of the sub-micron precursor films. When precursor films are subject to 1 M NaCl treatment, the best CISSe device presents an 8.0% efficiency (Figure 6.9a and Table 5.4). Compared to the CISSe without NaCl treatment, the V_{oc} increases to the value of 466.0 mV, however, the J_{sc} and *FF* are slightly decreased to 28.7 mA/cm^2, and 59.6%, respectively. The J_{sc} and *FF* of the best performing CISSe solar cells incorporating Na decrease with increasing the Na concentration before starting to recover (for 1 M NaCl).

For the reference sub-micron CISSe solar cell, the EQE peaks at 540 nm with a value surpassing 87%. The highest EQE is observed in the wavelength range from 380-1300 nm for sub-micron CISSe solar cells. When the precursor film is subject to 0.4 M NaCl treatment, the EQE response is better than the reference CISSe and other concentrations. There is a significant decrease in absorption in the wavelength range of 500-1300 nm for the absorber soaking in 0.8 M NaCl solution treatment. The absorption edges of EQE spectra can be used to extract the bandgap of absorbers. The absorption edges of absorbers with Na incorporation shift towards a shorter wavelength.

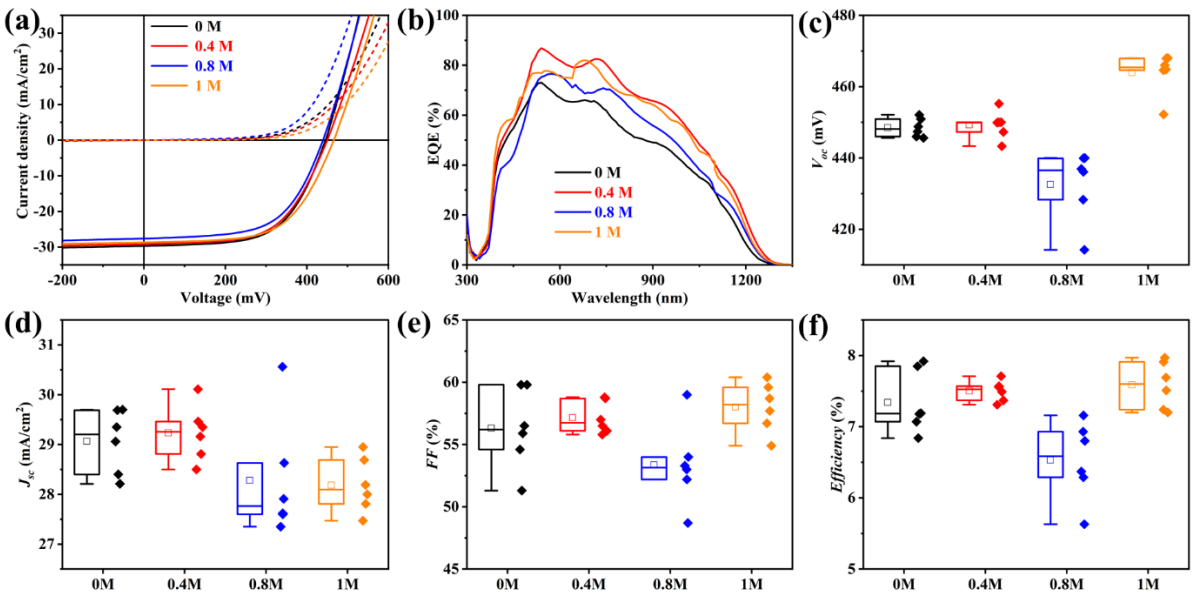

Figure 6.9: (a) *J-V* curves (f) EQE spectra of the best CISSe devices with different concentrations of NaCl for pre-selenization treatment. The distribution of (b) V_{oc}, (c) J_{sc}, (d) *FF*, and (e) *PCE*.

Table 6.4: Averaged (six devices) and best CISSe photovoltaic device parameters without and with various concentrations of NaCl treatment. The absorber thickness was 740 nm.

Smaple*	V_{oc} (mV)	J_{sc} (mA/cm^2)	*FF* (%)	*PCE* (%)
no additional NaCl	448.5±2.6 445.6	29.1±0.6 29.7	56.3±3.2 59.8	7.3±0.4 7.9
0.4 M NaCl	449.3±3.9 450.0	29.2±0.6 29.2	57.2±1.3 58.8	7.5±0.1 7.7
0.8 M NaCl	432.6±9.9 439.9	28.3±1.2 27.6	53.4±3.3 59.0	6.5±0.6 7.2
1 M NaCl	463.9±5.9 466.0	28.2±0.6 28.7	58.0±2.0 59.6	7.6±0.3 8.0

* Efficiency, V_{oc}, J_{sc}, and *FF* are presented with (average ± standard deviation) calculated from 6 devices.

The box plots of V_{oc}, *FF*, and *PCE* for devices first decrease and then increase, they are in good agreement with the co-evaporation NaCl treatment in the literature.[55, 58] However, the decrease in J_{sc} of absorbers with Na incorporation is observed.

The shunt conductance (G_{sh}), series resistance (R_s), diode ideality factor (A), and the reverse saturation current (J_0) can be calculated from the *J-V* curves as shown in Figure 6.10 and Table 6.5. G_{sh} can be extracted from the *J-V* curves of CISSe with various NaCl concentrations by plotting *dJ/dV* against *V* in the range near J_{sc} (Figure 6.10a). The G_{sh} values are calculated to be 2.54 mS/cm^2 for the reference CISSe device. The smallest G_{sh} value (1.90 mS/cm^2) is obtained from CISSe with 1 M NaCl pre-selenization treatment. The shunt resistance can be calculated from G_{sh}. The largest R_{sh} (526.32 Ω·cm^2) is observed from the CISSe with 1 M NaCl for treatment (Table 6.5).

Table 6.5: Summary of detailed electrical parameters for the best CISSe solar cells without and with various concentrations of NaCl treatment. The absorber thickness is 740 nm.

	G_{sh} (mS/cm^2)	R_{sh} (Ω·cm^2)	R_s (Ω·cm^2)	J_0 (mA/cm^2)	A	N_A (cm^{-3})	W_d (nm)
no additional NaCl	2.54	393.70	1.15	1.29×10^{-3}	2.10	1.9×10^{16}	315.0
0.4 M NaCl	2.25	444.44	1.78	1.08×10^{-3}	1.95	8.9×10^{15}	337.3
0.8 M NaCl	3.51	284.90	1.32	3.50×10^{-3}	2.15	2.2×10^{16}	325.8
1 M NaCl	1.90	526.32	1.66	5.93×10^{-4}	2.04	9.1×10^{15}	303.5

The high R_{sh} values prove that the carrier recombination and current loss in CISSe solar cells (1 M NaCl treatment) can be reduced effectively. The values for R_s and A are acquired from the intercept of the y-axis and slope (AkT/q) at dV/dJ *vs.* $(J+J_{sc})^{-1}$ curves. Figure 6.10b presents the values of R_s and A with the variation of NaCl concentration. The smallest R_s = 1.15 $\Omega \cdot cm^2$ is obtained from the reference CISSe. Na-treated CISSe solar cells display higher R_s than the reference CISSe, 1.78 $\Omega \cdot cm^2$ for 0.4 M, 1.32 $\Omega \cdot cm^2$ for 0.8 M, and 1.66 $\Omega \cdot cm^2$ for 1 M.

The y-axis intercept of $(J+J_{sc}-G_{sh}V)$ *vs.* $(V-R_sJ)$ curves can provide the saturation current density J_0. The J_0 of the CISSe absorber 1 M (5.93×10^{-4} mA/cm^2) NaCl treatment is significantly lower than other CISSe (Figure 6.10c). It is known that A and J_0 reflected the quality of the p-n junction.[33, 114] The reduction of A and J_0 suggested that 1 M NaCl treatment improved the heterojunction quality, resulting in better PV performance.

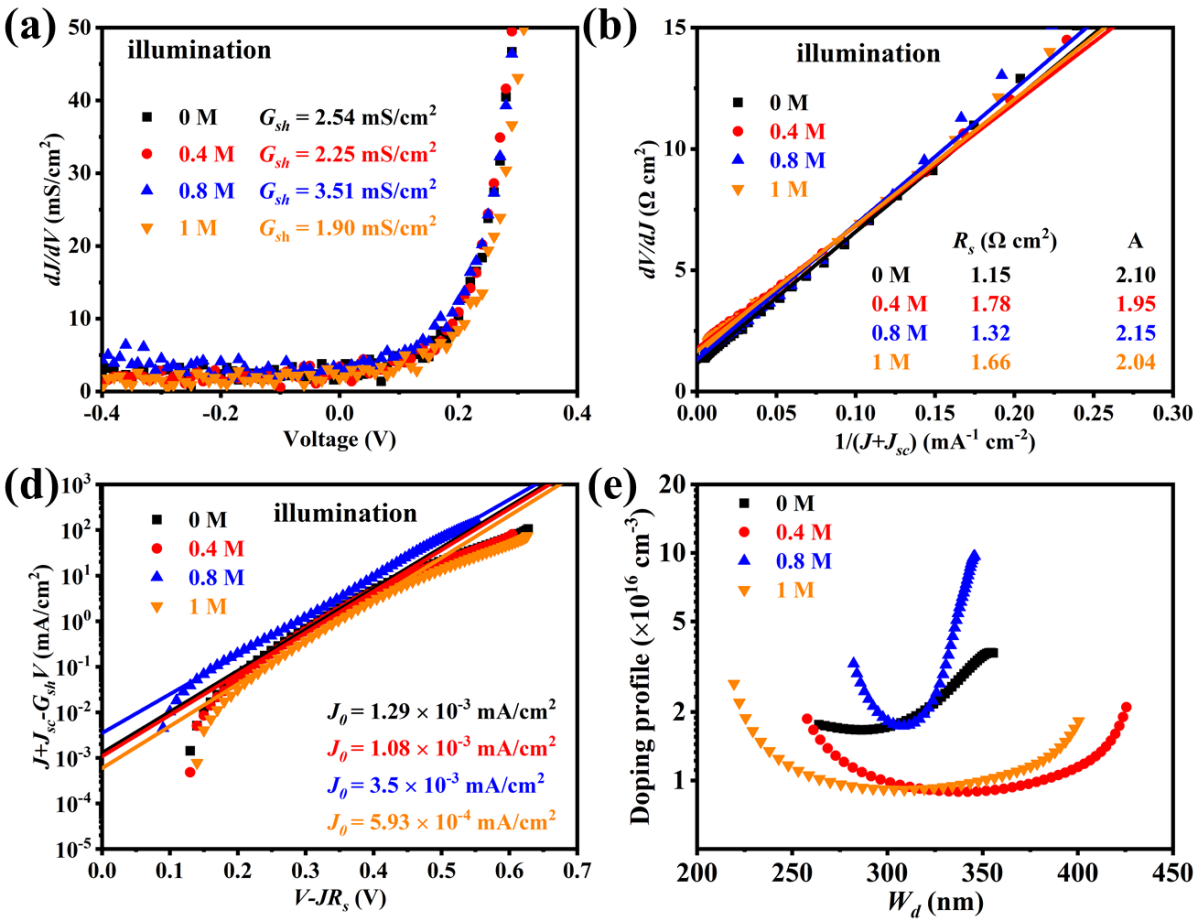

Figure 6.10: Plots of (a) dJ/dV *vs.* V for extraction of G_{sh}, (b) dV/dJ *vs.* $1/(J+J_{sc})$ for derivation of R_s and A, and (c) semi-logarithmic plot of $J+J_{sc}-G_{sh}V$ *vs.* $V-JR_s$ to determine J_0; (d) charge density and depletion width for CISSe solar cells with sub-micron absorber without NaCl and with various concentrations of NaCl for pre-selenization treatment.

Figure 6.10d shows the N_A-W_d profiles of CISSe solar cells without/with NaCl treatment. The sub-micron CISSe without NaCl treatment shows a charge carrier density of 1.9×10^{16} cm^{-3} and a W_d of 315.0 nm. The absorbers with 0.4 M and 1 M NaCl treatment exhibit a lower hole density, 8.9×10^{15} cm^{-3} for 0.4 M and 9.1×10^{15} cm^{-3} 1 M NaCl treatment, respectively. However, a high N_A (2.4×10^{16} cm^{-3}) is observed from the absorber using 0.8 M NaCl for pre-selenization treatment. The remarkable lower hole density can be attributed to a higher recombination at the rear interface.

7 Rear interface modification for semi-transparent $Cu(In,Ga)(S,Se)_2$

This chapter is in part based on the following publication:

Yao Gao, Guanchao Yin, Martina Schmid. Rear Interface Engineering in Solution-Processed Submicron $Cu(In,Ga)(S,Se)_2$ Solar Cells on Transparent Sn: In_2O_3 Back Contact. ***Advanced Materials Interfaces***, 2023, 2300566 (DOI: 10.1002/admi.202300566). As the first author of this manuscript, I conceived the idea and fabricated all the devices, conducted the measurements, performed the data analysis and prepared the manuscript.

7.1 Motivation

Typically, Molybdenum (Mo) is used as back contact material for various chalcogenide thin film solar cells due to the formation of the favorable quasi-Ohmic contact at the absorber/Mo interface. However, the Mo back contact has a strong parasitic absorption, leading to an increase in optical losses.[43, 91-92] Compared to the opaque Mo back contact, the fabrication of CIGSSe absorbers on transparent conductive oxide (TCO) back contacts can reduce the optical losses of CIGSSe solar cells and open up further application areas.[13, 65-66] Various transparent conductive oxides like tin-doped indium oxide (ITO), fluorine-doped tin oxide (FTO), and aluminum-doped zinc oxide (AZO), have been used as back contact of CIGSSe solar cells.[12, 65, 110-111] However, the highly resistive GaO_x layer forming at the CIGSSe/TCO rear interface during the CIGSSe growth (temperatures above 520°C) leads to the blocking of hole extraction from the CIGSSe absorber, resulting in high recombination.[12, 110] Therefore, the rear interface composition plays a crucial role in obtaining high-efficiency CIGSSe solar cells on TCO.

So far, there are still rare reports for the fabrication of CIGSSe on TCO back contacts utilizing the solution process since the highest efficiency is only 6%.[12] High-quality CIGSSe solar cells on TCO were fabricated at low substrate temperature by a co-evaporation process.[91-92] However, when the sequentially grown solution-processed precursor films are selenized at low temperatures, the rear side of the absorber consists of an undesired layer of fine grains, related to a high recombination rate.[111] Therefore, it is still challenging to produce high-quality CIGSSe on TCO back contacts by solution processing. Inserting a thin Mo layer between the CIGSSe and TCO back contact is a potential strategy to overcome this challenge because it allows CIGSSe absorber growth at high temperatures without the formation of GaO_x.[8, 115-116] However, the parasitic optical absorption of Mo is a challenge in improving the usage of e.g. unabsorbed light reflected back into the absorber by a reflective Ag mirror.[43-45, 116] In our previous research, an 8% CISSe (no Ga) solar cell with a sub-micron absorber has been

successfully fabricated on ITO back contact by annealing and selenizing the solution-processed metal-chloride-DMF precursor film at 520°C.[84] An electrical benign contact forms at the CISSe/ITO interface. However, open-circuit voltage (V_{oc}) and fill factor (*FF*) are still low, which limits further efficiency improvement. Therefore, CIGSSe solar cells including gallium are favorable due to the expected higher V_{oc} and efficiency compared to CISSe owing to the widened band gap with increasing Ga content.[36] Given the achieved good performance of CISSe on ITO, introducing a thin electrical beneficial CISSe layer at the CIGSSe/ITO interface is a potential strategy for achieving high-efficiency CIGSSe solar cells fabricated from the solution process without undesired optical losses.

In this work, we report on highly efficient CIGSSe solar cells deposited from metal-chloride-DMF solution on an ITO back contact. A thin Cu-In-TU-DMF layer is pre-deposited on the ITO back contact for interface modification before the Cu-In-Ga-TU-DMF precursor solution. This rear interface modification layer is applied to reduce the Ga concentration at the rear interface of the CIGSSe absorber. The lower Ga concentration at the rear interface favors obtaining a high-quality CIGSSe absorber and hinders the formation of the GaO_x interlayer.[84]

7.2 Results and discussion

Figure 7.1 shows the schematic illustration of the structure without/with a Ga-free modification layer (Cu-In-TU-DMF). In brief, the Ga-free layer is firstly spin-coated on ITO back contact. The elemental distributions of the absorbers are measured by GD-OES and are shown in Figure 7.2. Both R-CIGSSe (reference CIGSSe) and T-CIGSSe (interface modification treatment CIGSSe) show lower Na concentrations near the front surface than in the absorber bulk (Figure 7.2a).

The R-CIGSSe absorber presents a significantly higher Na concentration in the bulk of the absorber (from 15% depth towards the rear surface) than the T-CIGSSe absorber. However, a reverse trend is observed near the front surface (0-15% depth). The T-CIGSSe absorber displays a mostly uniform and low concentration of Na, which can be attributed to a small content of Na diffusing into the T-CIGSSe absorber from the SLG substrate.

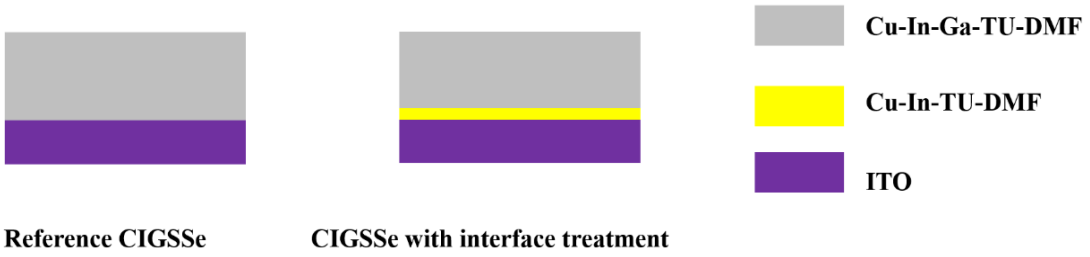

Figure 7.1: The recipe of CIGSSe absorber with or without interface treatment.

In the solution process, high-quality and dense chalcopyrite absorbers grow from the liquid-phase $Cu_{2-x}Se$ compound.[36] Compared to the lattice constant of $CuGaSe_2$ (0.560 nm), $CuInSe_2$ (0.578 nm) and $Cu_{2-x}Se$ (0.579 nm) have highly similar lattice constants, resulting in the formation of a dense layer on the bottom of the T-CIGSSe absorber.[117] From this it is concluded that the T-CIGSSe absorber contains a lower Na concentration than the R-CIGSSe absorber. A high Na content will promote GaO_x formation during the absorber growth at a high temperature.[118-119] Therefore, a thin In-rich interface modification layer in the T-CIGSSe favors the formation of a dense benign electrical rear interface, which can reduce the diffusion of Na, resulting in hindering the GaO_x formation. As can be seen in Figure 7.2b, the Cu/(Ga+In) (CGI) ratio in R-CIGSSe and T-CIGSSe absorbers increases toward the front surface, yet drops in its direct vicinity. The T-CIGSSe absorber shows a wider Cu-depletion at the front surface compared to the R-CIGSSe absorber. Na can occupy Cu vacancies of the CIGSSe absorber, leading to a low Cu concentration in the bulk of the R-CIGSSe absorber (15%-70% absorber depth) with a relatively high Na concentration.[36, 120]

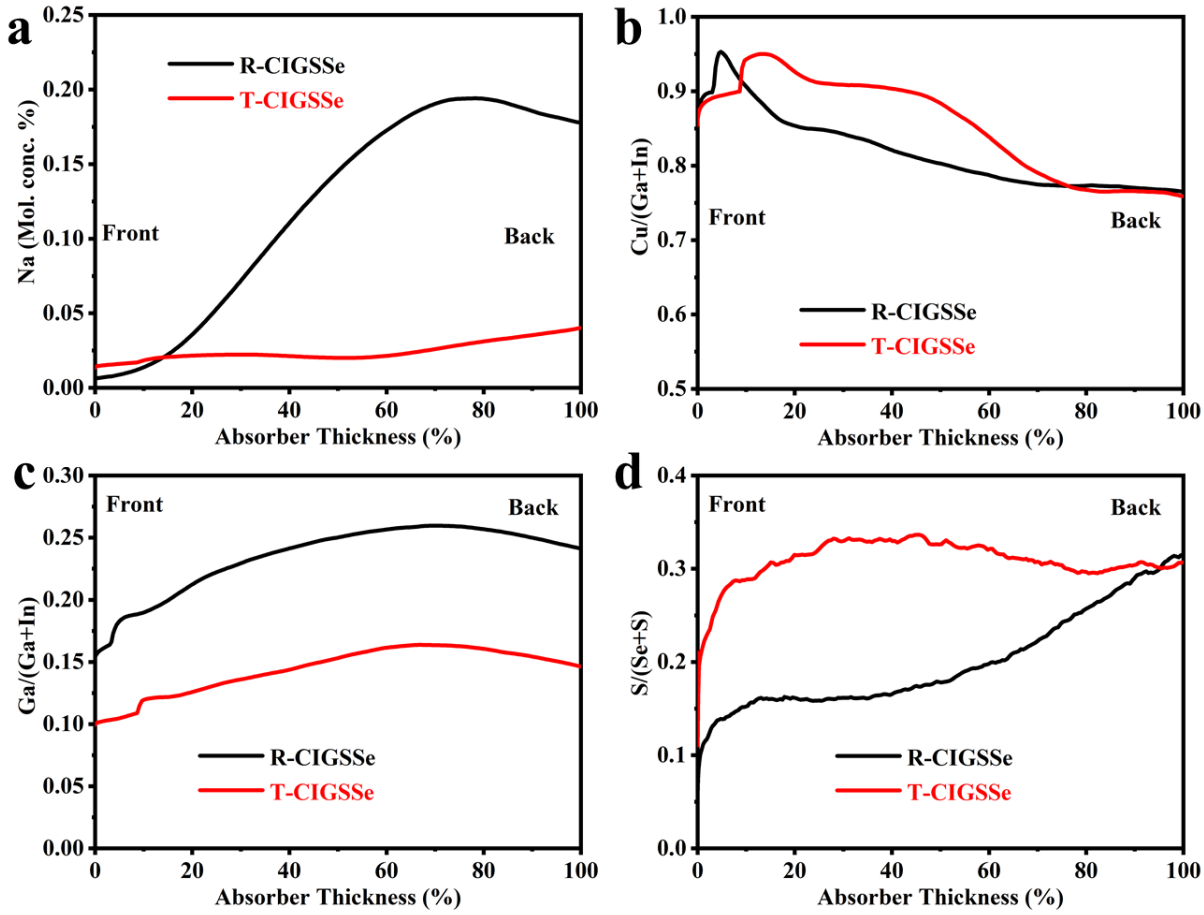

Figure 7.2: (a) Na concentration profiles, (b) Cu/(Ga+In), (c) Ga/(Ga+In), and (d) S/(Se+S) ratios of absorbers measured by GDOES. The x-axis is normalized to 100% absorber thickness.

Both of these two CIGSSe absorbers exhibit a similar tendency of Ga/(In+Ga) ratio (GGI) (Figure 7.2c), which can be attributed to the inter-diffusion of In and Ga. Ga diffuses toward the rear side, and In migrates toward the front side of the absorber.[20, 110, 117] The maximum GGI occurs at a depth of approx. 70%. Simultaneously, an overall larger GGI exists in the R-CIGSSe absorber rather than in the T-CIGSSe absorber. A pronounced increase in the S/(Se+S) ratio toward the rear interface is observed in the R-CIGSSe absorber in contrast to a high and homogeneous distribution for T-CIGSSe (Figure 7.2d). It is reported that In_2S_3 shows a lower standard molar formation enthalpy (-427.0 kJ/mol) at 298.15 K than In_2Se_3 (-78 kJ mol^{-1}), indicating that In_2S_3 forms easier than In_2Se_3.[113] T-CIGSSe presents a higher CGI than R-CIGSSe in the 15%-70% absorber depth (Figure 7.2b), which can be beneficial for large grain formation and reduction of the number density of grain boundaries. However, the volatilization of elemental S occurs along the grain boundaries. Both, the formation of In_2S_3 and reduction of grain boundaries hinder the volatilization of elemental S in the T-CIGSSe (S comes from the thiourea of the precursor solution), leading to the high concentration of S in the T-CIGSSe absorber.

Cross-sectional SEM images of the CIGSSe devices are shown in Figure 7.3. The thicknesses of the CIGSSe absorbers are 730 nm. The R-CIGSSe can be divided into an approximately 300 nm thick layer with small grains on top and a 400 nm thick layer with a non-uniform size of CIGSSe grains on the bottom (Figure 7.3a). These larger gains on the bottom can be attributed to the high content of Na (Figure 7.2a). Unlike the R-CIGSSe absorber, a large-grain top layer of approximately 450 nm is observed in the T-CIGSSe (Figure 7.3b), which can be explained by a slightly higher Na content near the front surface (0-15% depth of absorber) of the T-CIGSSe. A continuous dense bottom layer is observed in the T-CIGSSe. It has been proven that CISe and $Cu_{2-x}Se$ have a similar lattice constant, and the CISe absorber is denser than the CGSe absorber.[84] When the absorbers have similar Cu content, the In-rich absorber consists of uniform and dense grains rather than the Ga-rich absorber.[117]

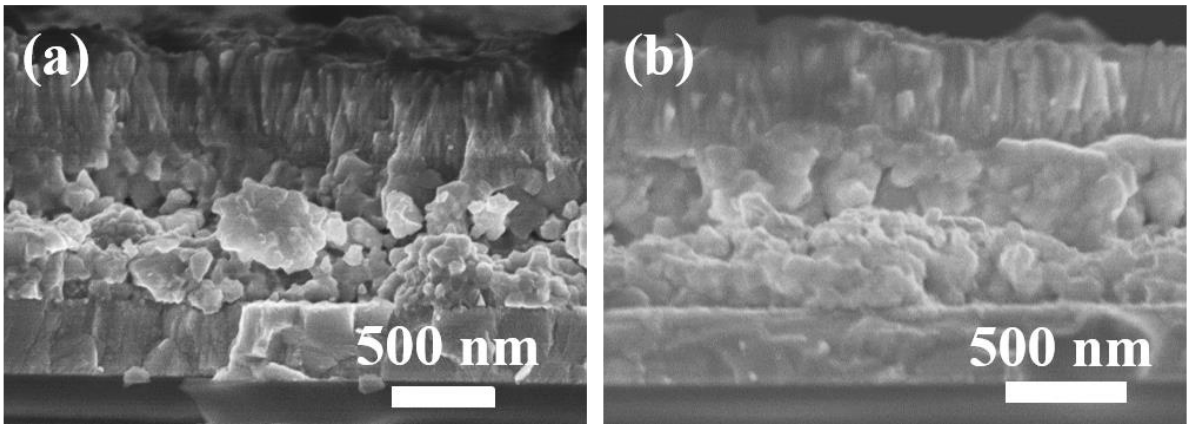

Figure 7.3: Cross-sectional SEM images of the (a) R-CIGSSe device, and (b) T-CIGSSe device.

The R-CIGSSe and the T-CIGSSe absorbers show similar CGI ratios in 75% to 100% depth (Figure 7.2b). The dense bottom layer of the T-CIGSSe absorber consisting of uniform grains in this depth is ascribed to smaller GGI (Figure 7.2c).

Figure 7.4a presents the current density-voltage (*J-V*) curves of the optimum R-CIGSSe and T-CIGSSe devices. A power conversion efficiency (*PCE*) of 2.4% is obtained for the R-CIGSSe solar cell with V_{oc} = 327.1 mV, J_{sc} = 14.0 mA/cm^2, and *FF* = 51.2%, respectively. When a Cu-In-TU-DMF layer is applied for rear interface modification, the *PCE* of the resulting T-CIGSSe device is significantly improved to 7.9% with V_{oc} = 565.8 mV, J_{sc} = 23.4 mA/cm^2, and *FF* = 59.5%, respectively. The improvement of *PCE* of the T-CIGSSe device can be ascribed to the remarkable increase in V_{oc} and J_{sc}. The statistical distributions of photovoltaic parameters for 14 CIGSSe sub-cells of each recipe are shown in Figure 7.4b and 7.4c. *PCE*, V_{oc}, J_{sc}, and *FF* of T-CIGSSe devices are superior to those of the R-CIGSSe devices, implying that the rear interface modification is an effective strategy to obtain high-efficiency CIGSSe/TCO structure solar cells.

The series resistance (R_s), the shunt conductance (G_{sh}), the shunt resistance (R_{sh}), the ideality factor (*A*), and the reverse saturation current density (J_0) are calculated from the illumination *J-V* data by using the Hegedus method.[55, 72]

$$J = J_0 exp\left[\frac{q}{AkT}(V - JR_s)\right] + G_{sh}V - J_{sc} \quad (7.1)$$

These electrical parameters are presented in Figure 7.4 and summarized in Table 7.1. The best T-CIGSSe device exhibits a smaller R_s and a larger R_{sh}, indicating that the Cu-In-TU-DMF interface modification can improve the charge transport and reduce the bulk recombination (Figure 7.4d and 7.4e).[110, 115]

The smaller J_0 in the T-CIGSSe device confirms reduced bulk recombination (Figure 7.4f). Therefore, the T-CIGSSe device presents better PV performance. However, the ideality factor of the T-CIGSSe device is higher than the R-CIGSSe (Figure 7.4d and Table 7.1), which can be explained by the high Na content near the front surface of the T-CIGSSe absorber (Figure 7.2).[78] This high Na-content will occupy the Cu vacancies and form Na_{Cu} defects, which will hinder the Cd^{2+} diffusion and formation of Cd_{Cu} donor defects during the CdS chemical bath deposition process. The high Na_{Cu} defect concentration located at the front surface of the absorber will thus limit the formation of a high-quality p-n junction, leading to a high ideality factor.[55] The PV performance of T-CIGSSe are still superior to the R-CIGSSe, indicating that the front surface is not the main reason for the limitation of achieving high efficiency in CIGSSe solar cells.

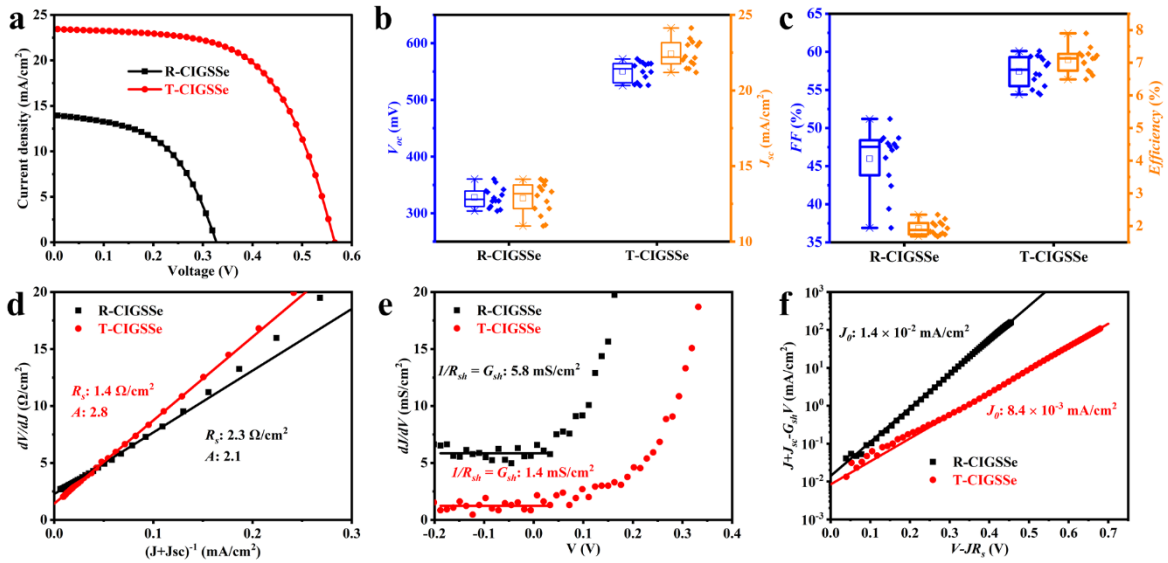

Figure 7.4: (a) *J-V* curves of the best CIGSSe solar cells; (b) statistical distributions of open circuit voltage V_{oc}, short current density J_{sc}, (c) fill factor *FF* and efficiency derived form 14 devices for each fabrication method; (d) *dV/dJ* as a function of $1/(J + J_{sc})$ with a linear fit to extract R_s from the y-intercept and *A* from slope, (e) *dJ/dV vs. V* for R_{sh} extraction, (f) $\ln(J+J_{sc}-G_{sh}V)$ with fit to determine J_0. (d) - (f) refer to the beset CIGSSe solar cells.

EQE measurements of the best R-CIGSSe and the best T-CIGSSe device are depicted in Figure 7.5a. They show a similar EQE in the short wavelength range (300-390 nm). Yet, the T-CIGSSe device exhibits a significantly higher spectral response in the 390-1100 nm range than the R-CIGSSe device. The band gap (E_g) values of the two cells are obtained from the plot of $[E\times\ln(1\text{-EQE})]^2$ *vs. E*.[84] The E_g of R-CIGSSe is 1.143 eV, while the E_g of T-CIGSSe is 1.155 eV (Figure 7.5b). The E_g value slightly increases by 0.012 eV, which can be ascribed to a high content of S in the T-CIGSSe absorber (Figure 7.2d). The Urbach energy (E_U) can be extracted from the EQE at the long-wavelength edge and reflects the carrier mobility and lifetime of the solar cells.[78-79] Figure 7.5c shows the corresponding relation between ln(EQE) and photon energy: E_U = 39.13 meV is obtained for the R-CIGSSe solar cell. The E_U value of the T-CIGSSe reduces to 18.94 meV, implying a significantly improved absorber quality.[78]

Table 7.1: Summary of photovoltaic parameters of the best CIGSSe device with or without interface modification.

	PCE (%)	V_{oc} (mV)	J_{sc} (mA/cm²)	*FF* (%)	R_s (Ω cm²)	R_{sh} (Ω cm²)	*A*	J_0 (mA/cm²)
R-CIGSSe	2.4	327.1	14.0	51.2	2.24	178.1	2.1	1.8×10^{-2}
T-CIGSSe	7.9	565.8	23.4	59.5	1.45	1176.5	2.8	8.6×10^{-3}

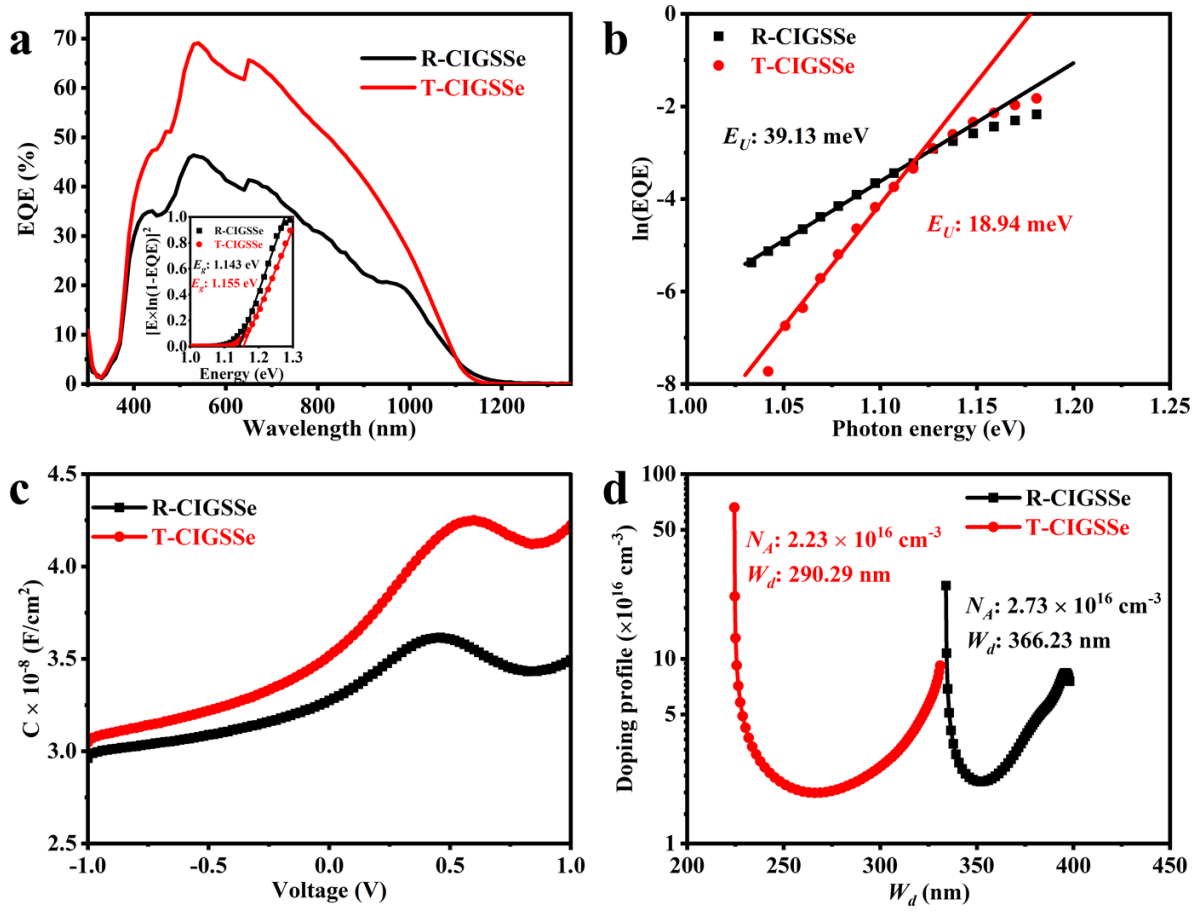

Figure 7.5: (a) External quantum efficiency, inset: bandgap extraction, (b) ln(EQE) as a function of photon energy at the long-wavelength edge to determine the Urbach energy E_U, (c) *C-V* curves, and (d) doping profiles for the best R-CIGSSe and T-CIGSSe solar cell.

The deficit in open circuit voltage, $V_{oc,def}$, calculated as the difference between this band gap value and the open circuit voltage from Table 7.1, is given in Table 7.2. It reduces from 815.9 mV to 589.2 mV, i.e. by > 25% relative, with interface modification and can partially be explained by a smaller E_U value of the T-CIGSSe device.[78]

Figure 7.5d shows the depletion width (W_d) as a function of charge carrier density (N_A) extracted from capacitance-voltage (CV) measurements at a bias voltage of 0 V. The R-CIGSSe device exhibits a larger N_A and wider W_d than the T-CIGSSe (Figure 7.5d and Table 7.2), which can be explained by the high Na content in the bulk and low Na content near the front surface of the R-CIGSSe absorber (Figure 7.2a). Generally, a wide W_d can promote the separation of photo-generated electron-hole pairs and benefit carrier transportation.[103] However, the PV performance of the R-CIGSSe device are significantly inferior. Therefore, the limitation of high-efficiency achievement in R-CIGSSe may come from the CIGSSe/ITO interface.

Figure 7.6 shows the voltage plotting obtained from temperature-dependent current density-voltage curves of CIGSSe solar cells. The activation energy E_a can be extracted from the *JVT* profile by linear extrapolation of V_{oc} to T = 0 K using the equation:[43, 55]

$$V_{oc} = \frac{E_a}{q} - \frac{AkT}{q} \ln\left(\frac{J_{00}}{J_{sc}}\right) \quad (7.2)$$

where k is the Boltzmann constant, A is the diode ideality factor, J_{sc} and J_{00} denote the short-circuit current density and the prefactor of saturation current density. Generally, when a CIGSSe absorber is fabricated on Mo back contact, E_a is close to the E_g of the CIGSSe absorber owing to a quasi-Ohmic contact assisted by the formation of $Mo(S,Se)_2$.

However, there is a non-negligible back barrier (Φ_B) remaining at the CIGSSe/ITO interface. Therefore, the back barrier is extracted from the plot of $\ln(R_sT)$ *vs.* $1/T$. The sheet resistance of as-sputtered ITO back contact is 32.02 Ω/sq, it can be reduced to 17.14 Ω/sq after subjecting to a pre-annealing at 500°C for 10 min. The sheet resistance of ITO back contact in the completed CIGSSe solar cells further reduces to 9.15 Ω/sq, which is measured by mechanically removing the CIGSSe absorber. However, this sheet resistance is still higher than the 0.3 Ω/sq for CIGSSe/Mo after removing the CIGSSe absorber. Therefore, the $\ln[(R_s\text{-}R_0)T]$ *vs.* $1/T$ plot cannot be applied to the back barrier calculation. E_a in equation (7.2) should be modified to $E_g\text{-}\Phi_B$, and the back barrier height can be extracted as $\Phi_B = E_g\text{-}E_a$.[43, 55]

A small value of E_a = 0.644 eV is observed for the R-CIGSSe device, revealing a large gap compared with E_g and pointing to interface recombination (Figure 7.6 and Table 7.2).[43, 121] There are two interfaces in the CIGSSe absorber: CdS/CIGSSe front interface and the CIGSSe/ITO rear interface. The R-CIGSSe device has a better p-n junction quality than the T-CIGSSe device, which is identified by GDOES (low Na content at the front surface) and *J-V* measurement (small ideality factor).

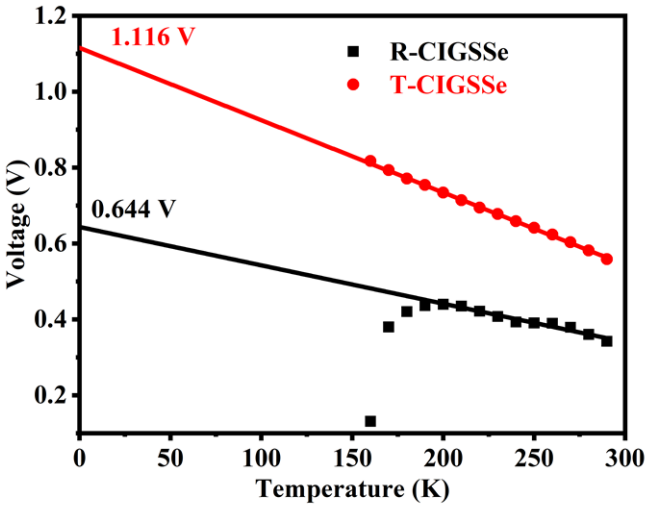

Figure 7.6: Temperature-dependent open-circuit voltage of CIGSSe solar cells and linear extrapolations to T = 0 K.

These results reveal that the main limitation for achieving high efficiency of the R-CIGSSe device is the serious rear interface recombination and the back barrier Φ_B amounts to 499 meV. On the contrary to the R-CIGSSe device, E_a of the T-CIGSSe device is significantly improved to 1.116 eV, i.e., only 39 meV (equal to Φ_B), smaller than E_g (Figure 7.5b). Thus, the dominant recombination mechanism in the T-CIGSSe devices is bulk recombination rather than interface recombination.[8] These results indicate that the dominant recombination path of the CIGSSe device can be changed from interface recombination to bulk recombination by utilizing Cu-In-TU-DMF for rear interface modification.

Combining the results of *J-V* and *JVT*, we derive the order of dominant recombination paths of these two CIGSSe devices:

R-CIGSSe interface recombination (dominant recombination)

> R-CIGSSe bulk recombination

> T-CIGSSe bulk recombination (dominant recombination)

> T-CIGSSe interface recombination.

Table 7.2: Electrical properties of the best R-CIGSSe and the best T-CIGSSe solar cells.

	E_g (eV)	E_U (meV)	N_A (cm^{-3})	W_d (nm)	E_a (eV)	$V_{oc,def}$ (mV)	Φ_B (meV)
R-CIGSSe	1.143	39.13	2.73×10^{16}	366.23	0.644	815.9	499
T-CIGSSe	1.155	18.94	2.23×10^{16}	290.29	1.116	589.2	39

8 Conclusion and outlook

8.1 Conclusion

In this thesis, we investigate Mo and ITO back contacts for submicron chalcopyrite solar cells. This submicron chalcopyrite absorber allows less raw material consumption in solar cell fabrication. Simultaneously, the solution-processed fabrication can further reduce the budget of starting materials. However, the parameters of the selenization process will affect the absorber quality and the PV performance. Generally, the quality of the solution-processed absorber is worse than that of fabricating by co-evaporation. In addition, the opaque Mo back contact will limit its application in bifacial and semi-transparent structures. This thesis solves those challenges in the following sequence: optimizing selenization and Se and S co-annealing conditions (chapter 4), strategies of Na incorporation for improving the absorber quality (chapter 5), the semi-transparent chalcopyrite solar cells (chapter 6) and improvement of the back contact using an interface modification layer (chapter 7).

A high quality CISSe absorber is achieved in a high Se content atmosphere. Additionally, S is introduced to solution-processed submicron CISSe absorbers during the annealing process to improve the PV performance. The corresponding high content of S and Se in the co-annealed absorber (HS-CISSe) presents larger CISSe grains than absorbers annealed in low and high selenium-only content (L-CISSe and H-CISSe). As a result, an optimum efficiency of 10.44% is achieved for the HS-CISSe solar cells with a significantly high open circuit voltage of 601.2 mV. Simultaneously, the highest efficient HS-CISSe solar cell exhibits a significant reduction in open circuit voltage deficit. Yet, the HS-CISSe devices exhibit a higher back contact barrier than H-CISSe devices, leading to a smaller short circuit current density.

As an increase in the back contact barrier is observed from the S and Se co-annealing process, only Se annealing (selenization) is utilized for further research. We investigated the PV performance improvement of solution-processed CISSe solar cells by using NaCl aqueous-ethanol solution for Na incorporation. The Na-treated CISSe absorbers present a significantly lower S content, resulting in narrower band gaps and J_{sc} improvement. For the Pre-ST CISSe absorbers (adding Na before selenization), the CISSe absorbers exhibit a uniform Na distribution and large grains. The Pre-ST CISSe solar cells achieve better PV performances than Pre-DT (Na deposition before spin-coating of precursor solution) and PST (addition of Na after selenization) CISSe. Additionally, Na-treated CISSe solar cells have a lower open circuit voltage deficit and back barrier height compared to the reference CISSe. The Na content can be adjusted by the soaking time of the precursor films or the concentration of NaCl solution. The optimal strategy in our research is to soak the precursor films (Pre-ST) in 1 M NaCl solution for 10 min. The open circuit voltage, short circuit current density, fill factor, and

efficiency of the Pre-ST CISSe are improved as compared to the reference CISSe. Furthermore, the open circuit voltage deficit and the back barrier height are reduced, underlining the improvement by adequate Na treatment. The Pre-ST for Na incorporation is a promising strategy for the efficiency improvement of solution-processed chalcopyrite solar cells.

Ultra-thin and sub-micron CISSe solar cells are successfully fabricated on ITO back contact via a low-cost metal-chloride DMF solution process. Variations of selenization temperature are investigated. Increasing the selenization temperature above 520°C may improve the crystallinity, morphology, and homogeneity of the CISSe absorbers. We demonstrate that 7.5% efficiency for semi-transparent ultra-thin CISSe solar cells (550 nm CISSe absorber thickness) is obtained at 520°C of selenization. The efficiency of CISSe solar cells firstly increases with the absorber thickness increasing to sub-micron (740 nm), however, it decreases when reaching micron (1440 nm) thickness. In addition, 8% efficiency for CISSe solar cells can be achieved when the sub-micron absorber is subject to a 1 M NaCl solution treatment. This work offers a facile method to prepare high-quality Na-doped CISSe films for integration in semi-transparent solar cell devices.

A Cu-In-TU-DMF layer is utilized for the CIGSSe/ITO interface (T-CIGSSe) modification, which presents a lower Na content than the reference absorber (R-CIGSSe) and is beneficial for suppressing the GaO_x rear interlayer formation. The origin of the lower Na content can be found in a denser bottom layer with uniform grain size. A smaller Urbach energy of the T-CIGSSe absorber indicates an improved absorber quality. Owing to the large grains and a better absorber quality, the T-CIGSSe device has a larger shunt resistance and a smaller reverse saturation current density than the R-CIGSSe device, confirming that the bulk recombination can be mitigated by interface modification. The open circuit voltage deficit of the T-CIGSSe device is significantly smaller than for R-CIGSSe and can also be explained by the better absorber quality of T-CIGSSe (smaller Urbach energy). However, the pn-junction quality of the R-CIGSSe devices appears better due to a smaller ideality factor and larger charge carrier density and depletion width values. Furthermore, a significantly smaller value of barrier height observed for the T-CIGSSe device indicates that the rear interface modification is a simple and effective strategy to reduce interface recombination and improve the properties of submicron CIGSSe solar cells on TCO back contact. As a result, the optimum efficiency of the rear interface modified CIGSSe (T-CIGSSe) solar cell achieves 7.9% with an open circuit voltage of 565.8 mV, a short circuit current density of 23.4 mA/cm^2, and a fill factor of 59.5%.

8.2 Outlook

This thesis shows an optimum efficiency of 10.4% for CISSe solar cells on Mo back contact produced via a solution process. Compared to the efficiency of CISSe on Mo back contact (η = 14.5%), there is still room for improving the performance of the CISSe solar cells.

Generally, when the precursor film is annealed in a selenium-only atmosphere, the V_{oc} of the CISSe solar cells is smaller than 550 mV. The V_{oc} of CISSe solar cells via an S and Se co-annealing strategy presents over 600 mV in our research (chapter 3). However, S-doped CISSe solar cells lead to low J_{sc}, simultaneously, the absorber quality deteriorates when applying a high content of S for S and Se co-annealing. Therefore, the S content should be controlled during the selenization process. Na-treated CISSe absorbers present a better quality than the Na-free CISSe, indicating that the alkali treatment effectively improves the PV performance of CISSe solar cells (chapter 4). For achieving a higher efficiency CISSe solar cell, a light-management structure is an alternative method to improve the efficiency of CISSe because this structure can improve the J_{sc}. Incorporating heavy alkali elements is a promising method to significantly improve the PV performance of our CISSe solar cells more than the Na treatment. Another strategy for PV performance improvement is the Ga incorporation because CIGSSe has a higher V_{oc} owing to the wider band gap than CISSe.

Our ITO-based CISSe and CIGSSe achieve around 7.9% efficiency, but they are still significantly lower than the co-evaporated CIGSe. The ITO-based CISSe solar cell with Na incorporation presents 8% efficiency. However, this efficiency improvement is not significant. In addition, the Ga-gradient CIGSSe solar cell can further improve its efficiency by facilitating the separation and collection of photo-generated charge carriers. Therefore, simultaneous Ga-gradient and alkali treatment could be a promising ITO-based CIGSSe solar cell improvement strategy. Finally, the bifacial ITO-based CIGSSe solar cells will further improve efficiency via increasing the usage of the illuminating light.

In summary, the efficiency improvement of CIGSSe solar cells could achieve the cost-efficient goal, which is beneficial for the large-scale manufacturing of CIGSSe solar cells.

Appendix A – Detail of Experiments

1. Materials

Thiourea (TU; 99%) is purchased from Alfa Aesar company; N, N-Dimethylformamide (DMF; 99.8%), ammonia ($NH_3 \cdot H_2O$; 25%), copper (I) chloride (CuCl; 99.8%), indium (III) chloride ($InCl_3$; 99.8%), gallium chloride ($GaCl_3$, 99.99%), selenium powder (Se, 99.5%), sulfur powder (S; 99.99%) cadmium acetate ($Cd(CH_3CO_2)_2$; 99.0%), sodium chloride (NaCl, 99.8%), potassium cyanide (KCN; 96%), and potassium hydroxide (KOH; 85%) from Sigma-Aldrich. All chemicals are used as received without further purification.

The molybdenum back contacts (with/without S_3N_4 barrier) are purchased from PVcomB, Helmholtz-Zentrum Berlin, Germany.

A tin-doped indium oxide (ITO) back contact is deposited on SLG (soda-lime glass) substrate using a DC-sputtering a PRO Line PVD 75 (Kurt J. Lesker Company).

2. Precursor solution preparation

2.1 Preparation of Cu-In-TU-DMF precursor solution:

First, 34.5 mmol of TU is added to 16 mL DMF solvent with stirring vigorously until a clear TU-DMF solution formed. Following, 5.1 mmol CuCl is completely dissolved in the previous TU-DMF solution under severe stirring. To obtain a Cu-poor molecular precursor solution, 5.5 mmol $InCl_3$ is added, and a yellowish solution (Cu-In-TU-DMF solution) is obtained after overnight stirring (Figure A1.1). Finally, the solution is filtered by using a 0.45 µm polytetrafluoroethylene filter.

2.2 Preparation of Cu-In-Ga-TU-DMF precursor solution

For the Cu-In-Ga-TU-DMF solution, the 8.45 mmol $InCl_3$ is replaced by 2.53 mmol $GaCl_3$ and 5.92 mmol $InCl_3$ (Ga/(In+Ga) = 0.3).

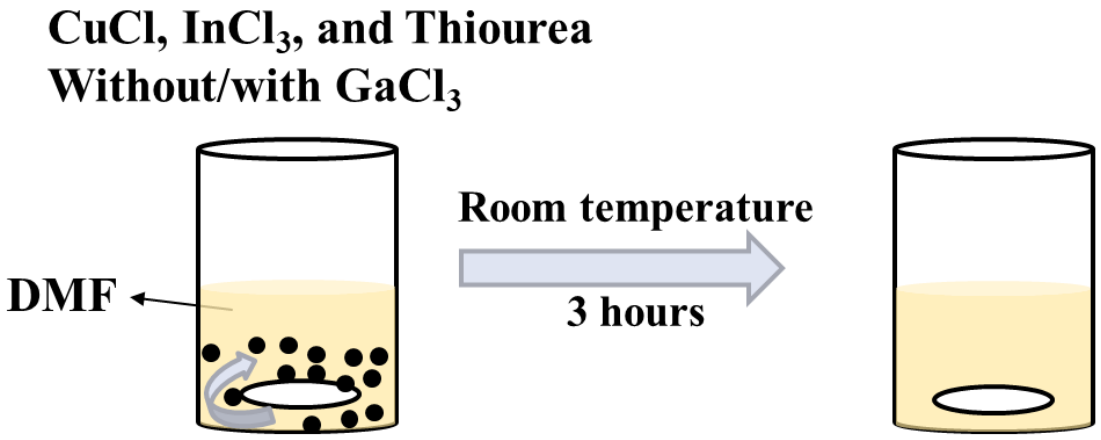

Figure A1.1: Scheme of Cu-In-(Ga)-TU-DMF precursor solution formation.

3. Preparation of chalcopyrite absorber

3.1 Precursor films deposition

The precursor solution is spin-coated on various back contacts (2.5 cm × 2.5 cm) at 1500 rpm for 60 s. Then, the wet film is immediately annealed on a hot plate at 350℃ for 2 min and moved to a ceramic plate for cooling down by natural convection. The coating-annealing-cooling cycle is repeated several times to get a total film thickness (Figure A1.2).

For the CIGSSe absorber with an interface treatment, the first layer is replaced by the Cu-In-TU-DMF solution (without Ga). This Cu-In-TU-DMF layer is used for interface modification. The other seven layers are spin-coated with Cu-In-Ga-TU-DMF solution.

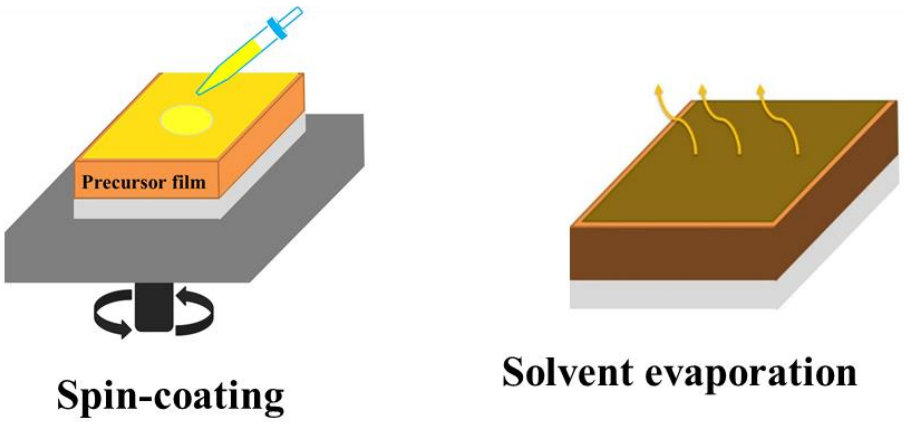

Figure A1.2: Schematic illustration of the spin-coating/annealing method for the deposition of CISSe or CIGSSe on Mo and ITO back contact.

3.2 Selenization

The as-prepared precursor films are processed in a tube furnace under Ar atmosphere with 180 mg or 240 mg Se powder for 2 samples (2.5 cm × 2.5 cm) by a first annealing step at 350℃ for 15 min and a second step at 540℃ for 20 min to form the CISSe absorber (Figure A1.3). In order to study the S and Se co-annealing, 200 mg Se and 40 mg S are used for annealing.

When the precursor films are fabricated on ITO back contacts, the temperature for selenization reduces to 520℃.

3.3 Sodium incorporation

The effect of Na incorporation strategies is investigated using 1M NaCl aqueous-ethanol solution (the volume ratio of ultra-pure water to ethanol is 1:1) for Na incorporation. NaCl is introduced in various experimental stages (Figure A1.4b), either prior to absorber deposition (pre-deposition treatment, Pre-DT), before selenization (pre-selenization treatment, Pre-ST), or after selenization (post-selenization treatment, PST). For the Pre-DT, the Mo back contact is soaked in 1 M NaCl for 10 min, then dried in N_2 flow. After that, the precursor film is deposited on the treated Mo back contact and subject to selenization, just as the reference sample. For the Pre-ST, the as-deposited precursor film is soaked in 1 M NaCl solution for 10 min, and then dried in N_2 flow. The selenization process of the Pre-ST film is identical to the reference sample. For the PST, a sample of reference type is soaked in 1 M NaCl solution for 10 min, dried in N_2, and annealed in 250 mg Se powder for 2 samples at 540℃ for 20 min.

The effect of treatment times of Pre-ST is studied using the precursor films soaked in 1 M NaCl solution for 5, 10, and 15 min. The Na-doped precursor films are subject to selenization under the same conditions as the reference sample.

The effect of NaCl concentration on the Pre-ST is investigated in a concentration range from 0.2 to 1.2 M with a step of 0.2 M. The soaking time is 10 min, then the samples are dried in N_2 gas flow. The procedure following the selenization is identical to the reference sample.

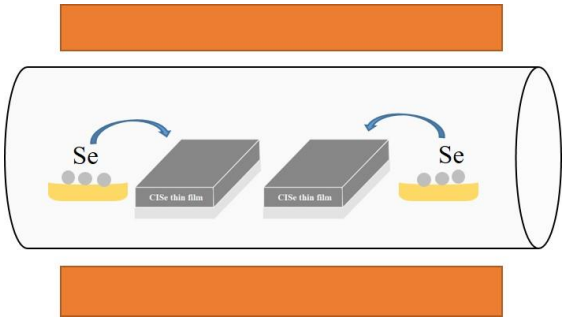

Figure A1.3: The selenization process of CI(G)SSe absorbers.

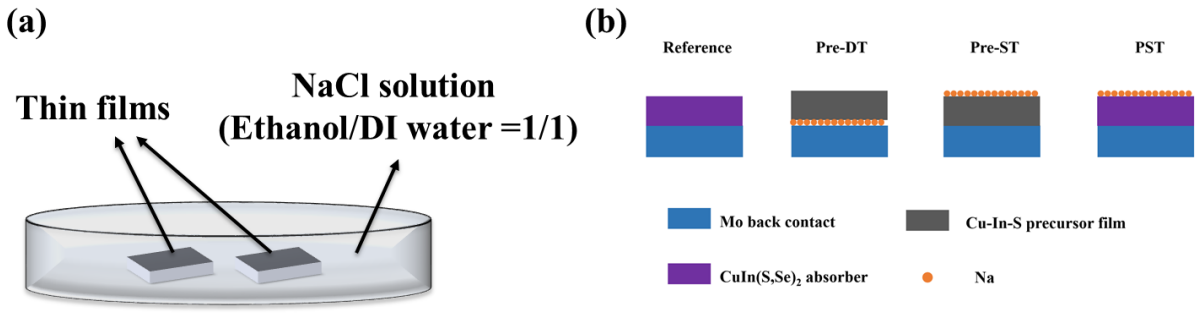

Figure A1.4: (a) a NaCl solution for Na incorporation, (b) NaCl treatment in various experiment stages.

4. Fabrication of Chalcopyrite solar cells

A solution of 10% KCN is used to etch the CIGSSe absorbers for 3 min to remove $Cu_{2-x}Se$, $Cu_{2-x}(S,Se)$, and excessive Se. CdS buffer layers of 80 nm thickness are deposited on CISSe absorber layers by a chemical bath deposition (CBD) method using a 50 mL precursor solution consisting of 0.075 M $Cd(CH_3CO_2)_2$, 0.1 M TU, and 19.9 M $NH_3 \cdot H_2O$. The CdS buffer layers are grown at 80°C for 6 min. 80 nm i-ZnO layers are deposited via a radio-frequency (RF) magnetron sputtering method at 120°C with 100 sccm Ar and 4 sccm O_2 and 1.5 $W \cdot cm^{-2}$ at 0.6 Pa. The high conductive aluminum doped zinc oxide (AZO) layers with 300 nm thickness are deposited by an RF magnetron sputtering method at 120°C with 100 sccm Ar and 2.5 $W \cdot cm^{-2}$ at 0.6 Pa. Finally, Ni/Al contact grids are deposited by thermal evaporation. The active area of each CISSe solar cell is 0.5 cm^2 defined by mechanical scribing.

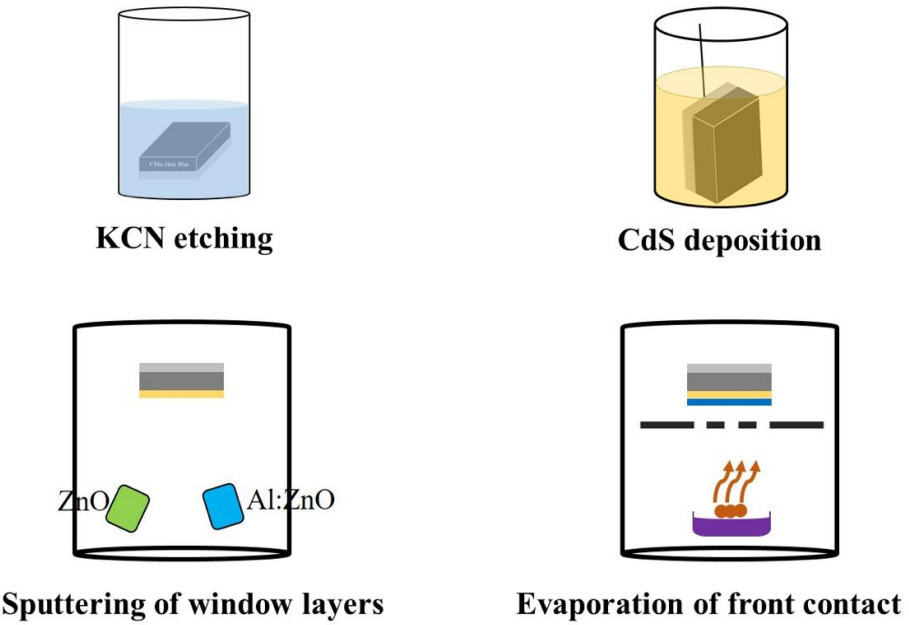

Figure A1.5: Fabrication processes of chalcopyrite solar cell.

Appendix B – Acknowledgement

Weakness and ignorance are not barriers to survival, but arrogance is. I suffered from some failed experiments in the past five years of my PhD study. Life's goal has been to surpass and become a better version of ourselves constantly. When the going gets tough, the tough keep going. I am very lucky that I got great helps from my supervisor, friends, colleagues, and my families.

I am grateful to my supervisors, Professor Markur Winterer and Professor Martina Schmid. They gave me an opportunity to start my PhD study. I am thankful to Guanchao Yin for guiding me in solving the trouble with my research. I am grateful to Sara El-Molla for teaching me how to start the spin-coating technique of solar cell fabrication. I am grateful to Tristan Köhler. He coached me in all the machines I used and taught me how to characterize my solar cells. I am grateful to Klaus Pärschke. He taught me how to measure absorber thickness, resistance, and optical measurements. I am grateful for Heidi. She provides a lot of useful information for my research and life. I am grateful to Yong Li for many discussions. I am grateful to Dr. Setarh Sedaghat. She gave me many suggestions regarding research and writing. I am grateful for Jan Lacaßen. He set up the CV characterization and analysis of our group. I am grateful to Dr Ihab Kardosh for the Raman and XRD measurements.

Luckily, I also got many reliable and friendly help from other groups. I would like to thank Alexander Poßberg from AG Weimann group (UDE), for supporting with XRD measurements. I would like to thank Jeldrik Schulte from AG Winterer group (UDE) for his support with SEM measurements. The X-ray data are collected using the Rigaku Smartlab High-Resolution X-ray diffractometer of the Nanoparticle Processing Technology (NPPT) group at the University of Duisburg-Essen. The instrument is funded through the DFG (German Research Foundation) Instrument proposal INST 20876/395-1 FUGG project number 450350889 and the state of North Rhine-Westphalia, Germany. We would like to thank Dr. Martin A. Schroer for assistance in using the instrument.

I especially acknowledge the financial support of the Chinese Scholarship Committee. I am thankful for the XRF and GD-OES equipment funding by the Deutsche Forschungsgemeinschaft (DFG, German Research Foundation) – INST 20876/324-1 FUGG and are acknowledged as follows: “Gefördert durch die Deutsche Forschungsgemeinschaft (DFG) – Projektnummer INST 20876/324-1 FUGG”. I am thankful for the Raman equipment funding by a Next-Gen Cluster-Tool of the Deutsche Forschungsgemeinschaft (DFG, German Research Foundation)—INST 20876/347-1 FUGG and are acknowledged as follows: “Gefördert durch die Deutsche Forschungsgemeinschaft (DFG)—Projektnummer INST 20876/347-1 FUGG”.

I would like to thank my family for supporting and financing my dreams of becoming a scientist. I am forever grateful to them for constantly encouraging me to take risks for what I

love to do. And tremendous thanks to my girlfriend, Yi Yu, for being supportive and cheering me up when I faced challenges during the course of my PhD program. I want to thank all who do not give up when life is at a low ebb.

Appendix C – Abbreviations and Symbols

Φ_B	Back barrier height
$\Phi(\lambda)$	Spectral photon flux of the AM1.5 spectrum
η *or PCE*	Power conversion efficiency
θ	Incident angle
ε_0	Vacuum permittivity
ε_R	Semiconductor dielectric constant
ΔE	Electrical field flux
ΔV	Reverse-bias voltage increment
υ	Frequency
λ	Wavelength
µm	Micrometer
Ω cm^2	Ohmic square centimeter
Ω/sq	Ohmic-per-square
A	Ideality factor
abs.	Absolute
Al	Aluminum
Ag	Silver
AM 1.5G	A global horizontal irradiance spectrum
approx.	Approximately
Ar	Argon
a-Si	Amorphous silicon
at.%	Atomic percentage
Au	Gold
AZO	Aluminium-doped zinc oxide
c	Speed of light in vacuum
CBD	Chemical bath deposition
CGI	Copper/(Gallium + Indium)

CGSe	Copper gallium selenide
CISSe	Copper indium sulfoselenide
CISe	Copper indium selenide
CIGSe	Copper indium gallium selenide
CIGSSe	Copper indium gallium sulfoselenide
CO_2	Carbon dioxide
CV or C-V	Capacitance-voltage
Cd	Cadmium
Cd^{2+}	Cadmium ion
Cd_{Cu}	Cd-on-Cu substitution donor defect
CdS	Cadmium sulfide
CdTe	Cadmium telluride
Cu	Copper
CuCl	Copper Chloride
$Cu_{2-x}Se$	Copper selenide
$Cu_{2-x}(S,Se)$	Copper sulfoselenide
℃	Degree celsius
DMF	N,N-Dimethylformamid
DMSO	Dimethyl sulfoxide
EQE	External quantum efficiency
E_a	Activation energy
E_{a1}	Activation energy at above 200 K
E_{a2}	Activation energy at below 200 K
E_C	Conduction band
E_F	Fermi level
E_g	Band gap
E_V	Valence band
E_U	Urbach energy

eV	Electronvolt
FF	Fill factor
FTO	Fluorine-doped tin oxide
FWHM	Full width at half maximum
g	Gram
GD-OES	Glow discharge optical emission Spectroscopy
GGI	Gallium/(Gallium +Indium)
GIXRD	Grazing incidence X-ray diffraction
GW	Giga watt
Ga	Gallium
$GaCl_3$	Gallium chloride
GaO_x	Gallium oxide
Ge	Germanium
G_{sh}	Conductance
h	Planck constant
H_2S	Hydrogen sulfide
HCl	Hydrogen chloride
H-CISSe	High selenium content selenized CISSe
HS-CISSe	High (Se and S) content annealed CISSe
IOH	Hydrogen-doped indium oxide
ITO	Tin-doped indium oxide
JVT	Temperature-dependent current density voltage
i-ZnO	Intrinsic zinc oxide
In	Indium
$InCl_3$	Indium chloride
J-V	Current density-voltage
J_0	Saturation current density
J_{00}	Reverse saturation current density

J_L	Light-generated current
J_{mpp}	Current density at the maximum power point
J_{sc}	Short-circuit current density
J_{EQE}	Current density calculated from EQE
J_{sc}^{SQ}	Current density limit according to Shockley-Queisser
k	Boltzmann constant
K	Kelvin
KCN	Potassium cyanide
KOH	Potassium hydroxide
kHZ	Kilohertz
K_{sp}	Solubility product constant
L-CISSe	Low selenium content selenized CISSe
M	Molar per liter
mA	Milliamps
mA/cm^2	Milliamps per square centimeter
mg	Milligram
min	Minute
mL	Milliliter
mV	Millivolt
mW/cm^2	Milli power per square centimeter
Mg	Magnesium
Mo	Molybdenum
MoNa	Na-coated Mo
MoO_3	Molybdenum oxide
$MoSe_2$	Molybdenum diselenide
$Mo(S,Se)_2$	Molybdenum dichalcogenide
N_2	Nitrogen
$NH_3{\cdot}H_2O$	Ammonia

Na	Sodium
NaCl	Sodium chloride
Na_{Cu}	Sodium atom occupies copper vacancy
NaF	Sodium fluoride
Na_2Se_x	Sodium selenide
N_A	Doping density of acceptors,
N_{cv}	Carrier density
N_D	Doping density of donors
Ni	Nickel
n_e	Number of generated electrons
nm	Nano meter
n_{ph}	Number of incident photons
OVC	Ordered vacancy compound
Pre-DT	Pre-deposition treatment
Pre-ST	Pre-selenization treatment
PST	Post-selenization treatment
PV	Photovoltaic
Pa	Pascal
P_{max}	Maximum generated power of solar cell
P_{in}	Incident power
P_L	Power of the input light source
q	Elemental charge
R	Reflection
RbF	Rubidium fluoride
rpm	Revolutions per minute
R_s	Series resistance
R_{sh}	Shunt resistance
s	second

S	Sulfur
SCR	Space charge region
sccm	Standard cubic centimetre per minute
Se	Selenium
SEM	Scanning electron micronscope
SH-based	Amine-thiol-based precursor
Si	Silicon
SIMS	Secondary-ion mass spectrometry
SiO_x	Silicon oxide
SLG	Soda-lime glass
T	Temperature
TA	Thioacetamide
TCO	Transparent conductive oxide
TU	Thiourea
V	Voltage
VBM	Valence band maximum
V_{bi}	Bias voltage
V_{Cu}	Cu vacancies
V_{mpp}	Voltage at the maximum power point
V_{oc}	Open-circuit voltage
$V_{oc,def}$	Open-circuit voltage deficit
vs.	Versus
V_{Se}	Se vacancies
V_{Se}-V_{Cu}	Se-Cu di-vacancy complex
W_d	Width of the depletion region
x_p	Width of space charge region in p-type semiconductor
x_n	Width of space charge region in n-type semiconductor
XRD	X-ray diffraction

XRF	X-ray fluorescence
Zn	Zinc

Appendix D – Publications and Conferences

Publications

1. **Yao Gao**, Guanchao Yin, Yong Li, Tristan Köhler, Ihab Kardosh, and Martina Schmid. An efficient S and Se co-annealing strategy for performance enhancement of solution-processed submicron $CuIn(S,Se)_2$ solar cells. ***IEEE Journal of Photovoltaic.*** (Early Access, DOI: 10.1109/JPHOTOV.2023.3334479).

2. **Yao Gao**, Guanchao Yin, and Martina Schmid. Sodium Incorporation for Performance Improvement of Solution-Processed Submicron $CuIn(S,Se)_2$ Thin Film Solar Cells. ***Small*** 2023, 19, 2302581 (DOI: 10.1002/smll.202302581).

3. **Yao Gao**, Gaunchao Yin, Yong Li, Tristan Köhler, Jan Lucaßen, Martina Schmid. 8.0% Efficient Submicron $CuIn(S,Se)_2$ Solar Cells on $Sn:In_2O_3$ Back Contact via a Facile Solution Process. ***ACS Applied Energy Materials***, 2022, 5, 12252-12260 (DOI: 10.1021/acsaem.2c01764).

4. **Yao Gao**, Guanchao Yin, Martina Schmid. Rear Interface Engineering in Solution-processed Submicron $Cu(In,Ga)(S,Se)_2$ Solar Cells on Transparent $Sn:In_2O_3$ Back Contact. ***Advanced Materials Interfaces***. 2023, 10, 2300566 (DOI: 10.1002/admi.202300566).

5. **Yao Gao**, Jilin Wang, Shuyi Mo, Fuwen Wang, Fei Long, Zhengguang Zou. Synthesis of High-Quality Wurtzite $Cu_2ZnSn(S_{1-x},Se_x)_4$ Nanocrystals with Non-Toxic Selenium Precursor and the Photoelectrochemical Performance of ZnO NAs/CZTSSe Heterojunction. ***Solar RRL***, 2018, 2, 1800015 (DOI: 10.1002/solr.201800015).

6. **Yao Gao**, Fei Long, Jilin Wang, Jin Zhang, Shuyi Mo, Zhengguang Zou. Understanding the growth mechanism of wurtzite Cu_2ZnSnS_4 nanocrystals and the photodegradation properties. ***Materials & Design***, 2017, 123, 24-31 (DOI: 10.1016/j.matdes.2017.03.012).

7. Christoph Rath, **Yao Gao**, Tristan Köhler, Martina Schmid. Impact of Band-gap Gradient in Semi-Transparent and Bifacial Ultra-Thin $Cu(In,Ga)Se_2$ Solar Cells. ***Advanced Materials Interfaces***. 2023, 2024, 11, 2400085 (DOI: 10.1002/admi.202400085).

8. Yong Li, Guanchao Yin, **Yao Gao**, Tristan Köhler, Jan Lucaßen, Martina Schmid. Sodium control in Ultrathin $Cu(In,Ga)Se_2$ solar cells on transparent back contact for efficiencies beyond 12%. ***Solar Energy Materials and Solar Cells***, 2021, 223, 110969 (DOI: 10.1016/j.solmat.2021.110969).

9. Julius Kruip, Ihab Kardosh, Tristan Köhler, **Yao Gao**, Martina Schmid. Growth of $(Ag,Cu)(In,Ga)Se_2$ Absorbers under Band Gap Variation and Characterization with a Focus on Optical Spectroscopy. ***Processes***, 2023, 11, 392 (DOI: doi.org/10.3390/pr11020392).

10. Yong Li, Guanchao Yin, Ye Tu, Setareh Sedaghat, **Yao Gao**, Martina Schmid. Ultrathin Cu(In,Ga)Se_2 Solar Cells with a Passivated Back Interface: A Comparative Study between Mo and In_2O_3: Sn Back Contacts. ***ACS Applied Energy Materials***, 2022, 5, 7956-7964 (DOI: 10.1021/acsaem.2c00088).

Conferences

1. **Yao Gao**, Yong Li, Jan Lucaßen, Martina Schmid. Effect of Pre-selenization Treatment with NaCl Solution on the Performance of Solution-Processed $CuIn(S,Se)_2$ Solar Cells. Poster Presentation at the Thin film chalcogenide photovoltaic materials, 31 May-4 June 2021, E-MRS Spring Meeting 2021.

2. **Yao Gao**, Yong Li, Martina Schmid. Solution-processed Growth of High-quality CISSe Solar Cells on ITO Back Contact. Poster Presentation at the 38th European Photovoltaic Solar Energy Conference and Exhibition, 6-10 September 2021.

List supervised bachelor students

1. Lukas Schneider, Injet Printing of CIGSe Absorber Islands, 2019.

2. Christoph Rath, Tuning Ga-gradient and Na concentration in Cu(In,Ga)Se_2 solar cell, 2023.

Appendix E - Curriculum Vitae

Personal information

Name	Yao Gao
Address	Mercatorstraße 112, 47051 Duisburg, Germany
Date of birth	4 August 1988
Place of birth	Guangxi, China
Nationality	Chinese
E-mail	yao.gao@uni-due.de

Eduction

November 2017 - present	**PhD student** at MultioptiX, Duisburg-Essen University, Germany
Sep. 2012 – Jul. 2015	**M.S. in Materials Science and Engineering,** Guilin University of Technology, China
Sep. 2008 – Jul. 2012	**B.S. in Inorganic Non-metal Material Engineering**, Guilin University of Technology, China

References

1. Dolf, G.; Ricardo, G.; Nicholas, W.; Rodrigo, L.; Gayathri, P.; Luca, L.; Elisa, A.; Sean, C.; Luis, J.; Rajon, B. *Global renewables outlook: Energy transformation 2050*; Abu Dhabi, United Arab Emirates: 2020.
2. REN21, P. R. S. *Renewables 2022 Global Status Report*; Renewable Energy Policy Network for the 21st Century: 2022.
3. Fraunhofer Institute for Solar Energy Systems, I. w. s. o. P. P. G. *Photovoltaics-Report*; 21 February 2023.
4. Green, M. A.; Dunlop, E. D.; Siefer, G.; Yoshita, M.; Kopidakis, N.; Bothe, K.; Hao, X., Solar Cell Efficiency Tables (Version 61). *Prog. Photovoltaics Res. Appl.* **2022,** *31*, 3-16.
5. van Lare, C.; Yin, G.; Polman, A.; Schmid, M., Light Coupling and Trapping in Ultrathin Cu(In,Ga)Se_2 Solar Cells Using Dielectric Scattering Patterns. *ACS Nano* **2015,** *9* (10), 9603-9613.
6. Massiot, I.; Cattoni, A.; Collin, S., Progress and Prospects for Ultrathin Solar Cells. *Nat. Energy* **2020,** *5*, 959-972.
7. Shin, M. J.; Lee, A.; Park, J. H.; Cho, A.; Ahn, S. K.; Shin, D.; Gwak, J.; Yun, J. H.; Yoo, J.; Cho, J.-S., Ultrathin Cu(In,Ga)Se_2 Transparent Photovoltaics: an Alternative to Conventional Solar Energy-Harvesting Windows. *Nano Energy* **2022,** *92*, 106711.
8. Yang, S.-C.; Lin, T.-Y.; Ochoa, M.; Lai, H.; Kothandaraman, R.; Fu, F.; Tiwari, A. N.; Carron, R., Efficiency Boost of Bifacial Cu(In,Ga)Se_2 Thin-Film Solar Cells for Flexible and Tandem Applications with Silver-Assisted Low-Temperature Process. *Nat. Energy* **2022,** *8*, 40-51.
9. Suresh, S.; Uhl, A. R., Present Status of Solution - Processing Routes for Cu(In,Ga)$(S,Se)_2$ Solar Cell Absorber. *Adv. Energy Mater.* **2021,** *11*, 2003743.
10. Kim, D.; Saifullah, M.; Jo, Y.; An, J. G.; Cho, J.-S.; Ahn, S.; Gwak, J.; Lee, H. S.; Park, J. H., Sulfur-Treated ITO Back Contact for Enhanced Performance of Semitransparent Ultrathin Cu(In,Ga)Se_2 Solar Cells. *ACS Appl. Energy Mater.* **2022,** *5*, 10611-10621.
11. Hölscher, T.; Placidi, M.; Becerril-Romero, I.; Fonoll-Rubio, R.; Izquierdo-Roca, V.; Thomere, A.; Bailo, E.; Schneider, T.; Kempa, H.; Scheer, R.; Pérez-Rodríguez, A., Effects of ITO Based Back Contacts on Cu(In,Ga)Se_2 Thin Films, Solar Cells, and Mini-Modules Relevant for Semi-Transparent Building Integrated Photovoltaics. *Sol. Energy Mater. Sol. Cells* **2023,** *251*, 112169.
12. Sousa, V.; Gonçalves, B. F.; Rosen, Y. S.; Virtuoso, J.; Anacleto, P.; Cerqueira, M. F.; Modin, E.; Alpuim, P.; Lebedev, O. I.; Magdassi, S.; Sadewasser, S.; Kolen'ko, Y. V., Over 6% Efficient Cu(In,Ga)Se_2 Solar Cell Screen-Printed from Oxides on Fluorine-Doped Tin Oxide. *ACS Appl. Energy Mater.* **2020,** *3*, 3120-3126.
13. Shin, M. J.; Park, S.; Lee, A.; Park, S. J.; Cho, A.; Kim, K.; Ahn, S. K.; Hyung Park, J.; Yoo, J.; Shin, D.; Jeong, I.; Yun, J. H.; Gwak, J.; Cho, J.-S., Bifacial Photovoltaic

Performance of Semitransparent Ultrathin Cu(In,Ga)Se_2 Solar Cells with Front and Rear Transparent Conducting Oxide Contacts. *Appl. Surf. Sci.* **2021,** *535*, 147732.

14. Chantana, J.; Arai, H.; Minemoto, T., Trap-assisted Recombination for Ohmic-like Contact at p-type Cu(In,Ga)Se_2/Back n-type TCO Interface in Superstrate-type Solar Cell. *J. Appl. Phys.* **2016,** *120* (4), 045302.
15. Nakamura, M.; Yamaguchi, K.; Kimoto, Y.; Yasaki, Y.; Kato, T.; Sugimoto, H., Cd-Free Cu(In,Ga)$(Se,S)_2$ Thin-Film Solar Cell With Record Efficiency of 23.35%. *IEEE J Photovolt.* **2019,** *9*, 1863-1867.
16. Sun, Y.; Lin, S.; Li, W.; Cheng, S.; Zhang, Y.; Liu, Y.; Liu, W., Review on Alkali Element Doping in Cu(In,Ga)Se_2 Thin Films and Solar Cells. *Engineering* **2017,** *3*, 452-459.
17. Laemmle, A.; Wuerz, R.; Schwarz, T.; Cojocaru-Mirédin, O.; Choi, P.-P.; Powalla, M., Investigation of the Diffusion Behavior of Sodium in Cu(In,Ga)Se_2 Layers. *J. Appl. Phys.* **2014,** *115*, 154501.
18. Wang, Y.; Lv, S.; Li, Z., Review onIincorporation of Alkali Elements and their Effects in Cu(In,Ga)Se_2 Solar Cells. *J Mater. Sci. Technol.* **2022,** *96*, 179-189.
19. Lin, T.-Y.; Chen, C.-H.; Wang, L.-W.; Huang, W.-C.; Jheng, Y.-W.; Lai, C.-H., Engineering Na-Transport to Achieve High Efficiency in Ultrathin Cu(In,Ga)Se_2 Solar Cells with Controlled Preferred Orientation. *Nano Energy* **2017,** *41*, 697-705.
20. Ramanujam, J.; Singh, U. P., Copper Indium Gallium Selenide Based Solar Cells - a Review. *Energy Environ. Sci.* **2017,** *10*, 1306-1319.
21. Pianezzi, F.; Reinhard, P.; Chirilă, A.; Bissig, B.; Nishiwaki, S.; Buecheler, S.; Tiwari, A. N., Unveiling the Effects of Post-Deposition Treatment with Different Alkaline Elements on the Electronic Properties of CIGS Thin Film Solar Cells. *Phys. Chem. Chem. Phys.* **2014,** *16*, 8843-8851.
22. Kato, T.; Wu, J.-L.; Hirai, Y.; Sugimoto, H.; Bermudez, V., Record Efficiency for Thin-Film Polycrystalline Solar Cells Up to 22.9% Achieved by Cs-Treated Cu(In,Ga)$(Se,S)_2$. *IEEE J Photovolt.* **2019,** *9*, 325-330.
23. Kim, J.-H.; Bae, S.; Min, B. K., Impact of Absorber Layer Morphology on Photovoltaic Properties in Solution-Processed Chalcopyrite Solar Cells. *ACS Appl. Mater. Interfaces* **2021,** *13*, 34-47.
24. Albalawneh, G.; Ramli, M., Review-Solution Processing of CIGSe Solar Cells Using Simple Thiol-Amine Solvents Mixture: A Review. *ECS J Solid State Sci. Technol.y* **2020,** *9*, 061013.
25. Mitzi, D. B., Solution Processing of Chalcogenide Semiconductors via Dimensional Reduction. *Adv. Mater.* **2009,** *21*, 3141-3158.
26. Gonçalves, B. F.; Sadewasser, S.; Salonen, L. M.; Lanceros-Méndez, S.; Kolen'ko, Y. V., Merging solution processing and printing for sustainable fabrication of Cu(In,Ga)Se_2 photovoltaics. *Chem. Eng. J* **2022,** *442*, 136188.
27. McCarthy, C. L.; Brutchey, R. L., Solution Processing of Chalcogenide Materials using Thiol-Amine "Alkahest" Solvent Systems. *Chem. Commun.* **2017,** *53*, 4888-4902.

28. Zhang, T.; Zhang, L.; Yin, Y.; Jiang, C.; Li, S. a.; Zhu, C.; Chen, T., A Thiol-Amine Mixture for Metal Oxide Towards Device Quality Metal Chalcogenides. *Sci. China Mater.* **2018,** *62*, 899-906.
29. Zhang, T.; Yang, Y.; Liu, D.; Tse, S. C.; Cao, W.; Feng, Z.; Chen, S.; Qian, L., High Efficiency Solution-Processed Thin-Film Cu(In,Ga)(Se,S)$_2$ Solar Cells. *Energy Environ. Sci.* **2016,** *9*, 3674-3681.
30. Park, G. S.; Chu, V. B.; Kim, B. W.; Kim, D.-W.; Oh, H.-S.; Hwang, Y. J.; Min, B. K., Achieving 14.4% Alcohol-Based Solution-Processed Cu(In,Ga)(S,Se)$_2$ Thin Film Solar Cell through Interface Engineering. *ACS Appl. Mater. Interfaces* **2018,** *10*, 9894-9899.
31. Lin, X.; Klenk, R.; Wang, L.; Köhler, T.; Albert, J.; Fiechter, S.; Ennaoui, A.; Lux-Steiner, M. C., 11.3% Efficiency Cu(In,Ga)(S,Se)$_2$ Thin Film Solar Cells via Drop-on-Demand Inkjet Printing. *Energy Environ. Sci.* **2016,** *9*, 2037-2043.
32. Kim, J.-H.; Kim, M. K.; Gadisa, A.; Stuard, S. J.; Nahid, M. M.; Kwon, S.; Bae, S.; Kim, B.; Park, G. S.; Won, D. H.; Lee, D. K.; Kim, D.-W.; Shin, T. J.; Do, Y. R.; Kim, J.; Choi, W. J.; Ade, H.; Min, B. K., Morphological-Electrical Property Relation in Cu(In,Ga)(S,Se)$_2$ Solar Cells: Significance of Crystal Grain Growth and Band Grading by Potassium Treatment. *Small* **2020,** *16*, 2003865.
33. Gao, Q.; Yuan, S.; Zhou, Z.; Kou, D.; Zhou, W.; Meng, Y.; Qi, Y.; Wu, S., Over 16% Efficient Solution-Processed Cu(In,Ga)Se$_2$ Solar Cells via Incorporation of Copper-Rich Precursor Film. *Small* **2022,** *18*, 2203443.
34. Aramoto, T.; Kawaguchi, Y.; Liao, Y.-C.; Kikuchi, Y.; Ohashi, T.; Iida, H.; Nakamura, N. In *High Efficiency Solution Coated Cu(In,Ga)(Se,S)$_2$ Thin Film Solar Cells*, Presented at 32nd European Photovoltaic Solar Energy Conf. and Exhibition, Munich, Germany, June 2016, 2016; pp 1108–1111.
35. Uhl, A. R.; Rajagopal, A.; Clark, J. A.; Murray, A.; Feurer, T.; Buecheler, S.; Jen, A. K. Y.; Hillhouse, H. W., Solution-Processed Low-Bandgap CuIn(S,Se)$_2$ Absorbers for High-Efficiency Single-Junction and Monolithic Chalcopyrite-Perovskite Tandem Solar Cells. *Adv. Energy Mater.* **2018,** *8*, 1801254.
36. Jiang, J.; Giridharagopal, R.; Jedlicka, E.; Sun, K.; Yu, S.; Wu, S.; Gong, Y.; Yan, W.; Ginger, D. S.; Green, M. A.; Hao, X.; Huang, W.; Xin, H., Highly Efficient Copper-rich Chalcopyrite Solar Cells from DMF Molecular Solution. *Nano Energy* **2020,** *69*, 104438.
37. Jiang, J.; Yu, S.; Gong, Y.; Yan, W.; Zhang, R.; Liu, S.; Huang, W.; Xin, H., 10.3% Efficient CuIn(S,Se)$_2$ Solar Cells from DMF Molecular Solution with the Absorber Selenized under High Argon Pressure. *Sol. RRL* **2018,** *2*, 1800044.
38. Clark, J. A.; Murray, A.; Lee, J.-M.; Autrey, T. S.; Collord, A. D.; Hillhouse, H. W., Complexation Chemistry in N,N-Dimethylformamide-Based Molecular Inks for Chalcogenide Semiconductors and Photovoltaic Devices. *J Am. Chem. Soc.* **2019,** *141*, 298-308.
39. Ma, C.; Xiang, C.; Liu, X.; Li, B.; Li, X.; Han, S.; Dai, Q.; Yan, W.; Xin, H., Over 12% Efficient CuIn(S,Se)$_2$ Solar Cell with the Absorber Fabricated from

Dimethylformamide Solution by Doctor-Blading in Ambient Air. *Sol. RRL* **2022,** *6*, 2200150.

40. Mansfield, L. M.; Kanevce, A.; Harvey, S. P.; Bowers, K.; Beall, C.; Glynn, S.; Repins, I. L., Efficiency Increased to 15.2% for Ultra-Thin Cu(In,Ga)Se_2 Solar Cells. *Prog. Photovoltaics Res. Appl.* **2018,** *26*, 949-954.
41. Kong, Y.; Huang, L.; Chi, Z.; Wu, X.; Li, J.; Xiao, X., Failure and Recovery Modes of Submicron Cu(In,Ga)Se_2 Solar Cells with High Cu Content. *ACS Appl. Mater. Interfaces* **2020,** *12*, 52857-52863.
42. Gloeckler, M.; Sites, J. R., Potential of Submicrometer Thickness Cu(In,Ga)Se_2 Solar Cells. *J. Appl. Phys.* **2005,** *98*, 103703.
43. Yin, G.; Knight, M. W.; van Lare, M.-C.; Solà Garcia, M. M.; Polman, A.; Schmid, M., Optoelectronic Enhancement of Ultrathin $CuIn_{1-x}Ga_xSe_2$ Solar Cells by Nanophotonic Contacts. *Adv. Opt. Mater.* **2017,** *5*, 1600637.
44. Gouillart, L.; Cattoni, A.; Chen, W. C.; Goffard, J.; Riekehr, L.; Keller, J.; Jubault, M.; Naghavi, N.; Edoff, M.; Collin, S., Interface Engineering of Ultrathin Cu(In,Ga)Se_2 Solar Cells on Reflective Back Contacts. *Prog. Photovoltaics Res. Appl.* **2020,** *29*, 212-221.
45. Gouillart, L.; Chen, W.-C.; Cattoni, A.; Goffard, J.; Riekehr, L.; Keller, J.; Jubault, M.; Naghavi, N.; Edoff, M.; Collin, S., Reflective Back Contacts for Ultrathin Cu(In,Ga)Se_2-Based Solar Cells. *IEEE J Photovolt.* **2019,** *10*, 250-254.
46. Shin, M. J.; Lee, A.; Cho, A.; Kim, K.; Ahn, S. K.; Park, J. H.; Yoo, J.; Yun, J. H.; Gwak, J.; Shin, D.; Jeong, I.; Cho, J.-S., Semitransparent and Bifacial Ultrathin Cu(In,Ga)Se_2 Solar Cells via a Single-Stage Process and Light-Management Strategy. *Nano Energy* **2021,** *82*, 105729.
47. Kobayashi, T.; Yamaguchi, H.; Jehl Li Kao, Z.; Sugimoto, H.; Kato, T.; Hakuma, H.; Nakada, T., Impacts of Surface Sulfurization on Cu(In_{1-x},Ga_x)Se_2 Thin-Film Solar Cells. *Prog. Photovoltaics Res. Appl.* **2015,** *23*, 1367-1374.
48. Ohashi, D.; Nakada, T.; Kunioka, A., Improved CIGS thin-film solar cells by surface sulfurization using In_2S_3 and sulfur vapor. *Sol. Energy Mater. Sol. Cells* **2001,** *67*, 261-265.
49. Keller, J.; Bilousov, O. V.; Neerken, J.; Wallin, E.; Martin, N. M.; Riekehr, L.; Edoff, M.; Platzer-Björkman, C., Heavy Alkali Treatment of Post-Sulfurized Cu(In,Ga)Se_2 Layers: Effect on Absorber Properties and Solar Cell Performance. *Sol. RRL* **2020,** *4*, 2000248.
50. Zhang, Y.; Gao, Q.; Ao, J.; Zhang, Y.; Bi, J.; Guo, J.; Han, Y.; Sun, G.; Zhang, Y.; Liu, W.; Liu, F., Enhancing Surface Properties for Electrodeposited Cu(In,Ga)Se_2 Films by (NH4)2S Solution at Room Temperature. *ACS Appl. Energy Mater.* **2021,** *4*, 3822-3831.
51. Yuan, S.; Wang, X.; Zhao, Y.; Chang, Q.; Xu, Z.; Kong, J.; Wu, S., Solution Processed Cu(In,Ga)$(S,Se)_2$ Solar Cells with 15.25% Efficiency by Surface Sulfurization. *ACS Appl. Energy Mater.* **2020,** *3*, 6785-6792.

52. Kim, S.; Mina, M. S.; Lee, J.; Kim, J., Sulfur-Alloying Effects on Cu(In,Ga)(S,Se)$_2$ Solar Cell Fabricated Using Aqueous Spray Pyrolysis. *ACS Appl. Mater. Interfaces* **2019,** *11*, 45702-45708.
53. Lin, Y.-C.; Wei, S.-J.; Liang, Y.-J.; Syus, W.-J., A Simple Non-Toxic Simultaneous Selenization/Sulfurization Process for Cu(In,Ga)(S,Se)$_2$ Solar Cells. *Mater. Chem. Phys.* **2018,** *219*, 283-291.
54. Li, W.; Song, Q.; Zhao, C.; Qi, T.; Zhang, C.; Wang, W.; Gao, C.; Zheng, X.; Ning, D.; Ma, M.; Zhang, J.; Feng, Y.; Chen, M.; Li, W.; Yang, C., Toward High-Efficiency Cu(In,Ga)(S,Se)$_2$ Solar Cells by a Simultaneous Selenization and Sulfurization Rapid Thermal Process. *ACS Appl. Energy Mater.* **2021,** *4*, 14546-14553.
55. Li, Y.; Yin, G.; Gao, Y.; Köhler, T.; Lucaßen, J.; Schmid, M., Sodium Control in Ultrathin Cu(In,Ga)Se$_2$ Solar Cells on Transparent Back Contact for Efficiencies Beyond 12%. *Sol. Energy Mater. Sol. Cells* **2021,** *223*, 110969.
56. Uličná, S.; Welch, L. M.; Abbas, A.; Togay, M.; Tsai, V.; Betts, T. R.; Malkov, A. V.; Walls, J. M.; Bowers, J. W., Sodium Doping of Solution-Processed Amine-Thiol Based CIGS Solar Cells by Thermal Evaporation of NaCl. *Prog. Photovoltaics Res. Appl.* **2021,** *29*, 546-557.
57. Li, W.; Yan, X.; Aberle, A. G.; Venkataraj, S., Effect of Sodium Diffusion on the Properties of CIGS Solar Absorbers Prepared using Elemental Se in a Two-step Process. *Sci. Rep.* **2019,** *9*, 2637.
58. Rehan, S.; Moon, J.; Kim, T. G.; Gwak, J.; Kim, J.; Kim, J. W.; Jo, W.; Ahn, S. K.; Ahn, S., Role of Na in Solution-Processed CuInSe$_2$ (CISe) Devices: A Different Story for Improving Efficiency. *Nano Energy* **2018,** *48*, 401-412.
59. Berner, U.; Colombara, D.; de Wild, J.; Robert, E. V. C.; Schütze, M.; Hergert, F.; Valle, N.; Widenmeyer, M.; Dale, P. J., 13.3% Efficient Solution Deposited Cu(In,Ga)Se$_2$ Solar Cells Processed with Different Sodium Salt Sources. *Prog. Photovoltaics Res. Appl.* **2016,** *24*, 749-759.
60. Guo, Q.; Ford, G. M.; Agrawal, R.; Hillhouse, H. W., Ink Formulation and Low-Temperature Incorporation of Sodium to Yield 12% Efficient Cu(In,Ga)(S,Se)$_2$ Solar Cells from Sulfide Nanocrystal Inks. *Prog. Photovoltaics Res. Appl.* **2013,** *21*, 64-71.
61. Gao, Y.; Yin, G.; Schmid, M., Sodium Incorporation for Performance Improvement of Solution-Processed Submicron CuIn(S,Se)$_2$ Thin Film Solar Cells. *Small* **2023,** *19*, 2302581.
62. Green, M. A.; Dunlop, E. D.; Levi, D. H.; Hohl-Ebinger, J.; Yoshita, M.; Ho-Baillie, A. W. Y., Solar cell efficiency tables (version 54). *Prog. Photovoltaics Res. Appl.* **2019,** *27*, 565-575.
63. Kato, Y.; Fujiwara, H., Numerical Values of Shockley-Queisser Limit. In *Hybrid Perovskite Solar Cells*, 2021; pp 563-565.
64. Kim, D.; Shin, S. S.; Lee, S. M.; Cho, J. S.; Yun, J. H.; Lee, H. S.; Park, J. H., Flexible and Semi-Transparent Ultra-Thin CIGSe Solar Cells Prepared on Ultra-Thin Glass

Substrate: A Key to Flexible Bifacial Photovoltaic Applications. *Adv. Funct. Mater.* **2020,** *30*, 2001775.

65. Nakada, T.; Hirabayashi, Y.; Tokado, T.; Ohmori, D.; Mise, T., Novel Device Structure for Cu(In,Ga)Se_2 Thin Film Solar Cells using Transparent Conducting Oxide Back and Front Contacts. *Sol. Energy* **2004,** *77*, 739-747.
66. Mavlonov, A.; Nishimura, T.; Chantana, J.; Kawano, Y.; Masuda, T.; Minemoto, T., Back-Contact Barrier Analysis to Develop Flexible and Bifacial Cu(In,Ga)Se_2 Solar Cells using Transparent Conductive In_2O_3:SnO_2 Thin Films. *Sol. Energy* **2020,** *211*, 1311-1317.
67. Schneider, T.; Dethloff, C.; Hölscher, T.; Kempa, H.; Scheer, R., Comparison of Mo and ITO Back Contacts in CIGSe Solar Cells: Vanishing of the Main Capacitance Step. *Prog. Photovoltaics Res. Appl.* **2021,** *30*, 191-202.
68. Heinemann, M. D.; Greiner, D.; Unold, T.; Klenk, R.; Schock, H. W.; Schlatmann, R.; Kaufmann, C. A., The Importance of Sodium Control in CIGSe Superstrate Solar Cells. *IEEE J Photovolt.* **2015,** *5*, 378-381.
69. Simchi, H.; McCandless, B. E.; Meng, T.; Shafarman, W. N., Structure and Interface Chemistry of MoO_3 Back Contacts in Cu(In,Ga)Se_2 Thin Film Solar Cells. *J. Appl. Phys.* **2014,** *115*, 033514.
70. Saifullah, M.; Rasool, S.; Ahn, S.; Kim, K.; Cho, J.-S.; Yoo, J.; Shin, W. S.; Yun, J. H.; Park, J. H., Performance and Uniformity Improvement in Ultrathin Cu(In,Ga)Se_2 Solar Cells with a WO_x Nanointerlayer at the Absorber/Transparent Back-Contact Interface. *ACS Appl. Mater. Interfaces* **2019,** *11*, 655-665.
71. Hamada, N.; Nishimura, T.; Chantana, J.; Kawano, Y.; Masuda, T.; Minemoto, T., Fabrication of Flexible and Bifacial Cu(In,Ga)Se_2 Solar Cell with Superstrate-Type Structure using a Lift-off Process. *Sol. Energy* **2020,** *199*, 819-825.
72. Hegedus, S. S.; Shafarman, W. N., Thin-Film Solar Cells: Device Measurements and Analysis. *Prog. Photovoltaics Res. Appl.* **2004,** *12*, 155-176.
73. Abou-Ras, D.; Kirchartz, T.; Rau, U., *Advanced Characterization Techniques For Thin Film Solar Cells*. Weinheim, Germany: Wiley-Vch: 2011.
74. Gong, Y.; Qiu, R.; Niu, C.; Fu, J.; Jedlicka, E.; Giridharagopal, R.; Zhu, Q.; Zhou, Y.; Yan, W.; Yu, S.; Jiang, J.; Wu, S.; Ginger, D. S.; Huang, W.; Xin, H., Ag Incorporation with Controlled Grain Growth Enables 12.5% Efficient Kesterite Solar Cell with Open Circuit Voltage Reached 64.2% Shockley-Queisser Limit. *Adv. Funct. Mater.* **2021,** *31*, 2101927.
75. Halim, M. A.; Islam, M. M.; Luo, X.; Sakurai, T.; Sakai, N.; Kato, T.; Sugimoto, H.; Tampo, H.; Shibata, H.; Niki, S.; Akimoto, K., A Comparative Study on Charge Carrier Recombination Across the Junction Region of $Cu_2ZnSn(S,Se)_4$ and Cu(In,Ga)Se_2 Thin Film Solar Cells. *AIP Adv.* **2016,** *6*, 035216.
76. Gunawan, O.; Todorov, T. K.; Mitzi, D. B., Loss mechanisms in hydrazine-processed Cu2ZnSn(Se,S)4 solar cells. *Appl. Phys. Lett.* **2010,** *97*, 233506.

77. Ott, T.; Schönberger, F.; Walter, T.; Hariskos, D.; Kiowski, O.; Salomon, O.; Schäffler, R., Verification of Phototransistor Model for Cu(In,Ga)Se_2 Solar Cells. *Thin Solid Films* **2015,** *582*, 392-396.
78. Chantana, J.; Kawano, Y.; Nishimura, T.; Kimoto, Y.; Kato, T.; Sugimoto, H.; Minemoto, T., Effect of Alkali Treatment on Photovoltaic Performances of Cu(In,Ga)$(S,Se)_2$ Solar Cells and Their Absorber Quality Analyzed by Urbach Energy and Carrier Recombination Rates. *ACS Appl. Energy Mater.* **2020,** *3*, 1292-1297.
79. Chantana, J.; Nishimura, T.; Kawano, Y.; Teraji, S.; Watanabe, T.; Minemoto, T., Examination of Relationship between Urbach Energy and Open-Circuit Voltage Deficit of Flexible Cu(In,Ga)Se_2 Solar Cell for Its Improved Photovoltaic Performance. *ACS Appl. Energy Mater.* **2019,** *2*, 7843-7849.
80. Nayak, P. K.; Mahesh, S.; Snaith, H. J.; Cahen, D., Photovoltaic Solar Cell Technologies: Analysing the State of the Art. *Nat. Rev. Mater.* **2019,** *4*, 269-285.
81. Kimerling, L. C., Influence of Deep Traps on the Measurement of Free - Carrier Distributions in Semiconductors by Junction Capacitance Techniques. *J. Appl. Phys.* **1974,** *45*, 1839-1845.
82. Elanzeery, H. The Cause of Interface Recombination in Cu-rich CIS Thin Film Solar Cells. University of Luxembourg, 2019.
83. Kim, S. T.; Larina, L.; Yun, J. H.; Shin, B.; Ahn, B. T., Surface Passivation and Point Defect Control in Cu(In,Ga)Se_2 Films with a Na_2S Post Deposition Treatment for higher than 19% CIGS Cell Performance. *Sustain. Energy Fuels* **2019,** *3*, 709-716.
84. Gao, Y.; Yin, G.; Li, Y.; Köhler, T.; Lucaßen, J.; Schmid, M., 8.0% Efficient Submicron CuIn$(S,Se)_2$ Solar Cells on Sn:In_2O_3 Back Contact via a Facile Solution Process. *ACS Appl. Energy Mater.* **2022,** *5*, 12252-12260.
85. Khavari, F.; Keller, J.; Larsen, J. K.; Sopiha, K. V.; Törndahl, T.; Edoff, M., Comparison of Sulfur Incorporation into $CuInSe_2$ and $CuGaSe_2$ Thin - Film Solar Absorbers. *Physica Status Solidi (a)* **2020,** *217*, 2000415.
86. Zhao, Y.; Yuan, S.; Chang, Q.; Zhou, Z.; Kou, D.; Zhou, W.; Qi, Y.; Wu, S., Controllable Formation of Ordered Vacancy Compound for High Efficiency Solution Processed Cu(In,Ga)Se_2 Solar Cells. *Adv. Funct. Mater.* **2020,** *31*, 2007928.
87. Zhao, Y.; Yuan, S.; Kou, D.; Zhou, Z.; Wang, X.; Xiao, H.; Deng, Y.; Cui, C.; Chang, Q.; Wu, S., High Efficiency CIGS Solar Cells by Bulk Defect Passivation through Ag Substituting Strategy. *ACS Appl. Mater. Interfaces* **2020,** *12*, 12717-12726.
88. Khallaf, H.; Chai, G.; Lupan, O.; Chow, L.; Park, S.; Schulte, A., Investigation of Aluminium and Indiumin Situdoping of Chemical Bath Deposited CdS Thin Films. *J Phys. D Appl. Phys.* **2008,** *41*, 185304.
89. Shukla, S.; Sood, M.; Adeleye, D.; Peedle, S.; Kusch, G.; Dahliah, D.; Melchiorre, M.; Rignanese, G.-M.; Hautier, G.; Oliver, R.; Siebentritt, S., Over 15% Efficient Wide-Band-Gap Cu(In,Ga)S_2 Solar Cell: Suppressing Bulk and Interface Recombination through Composition Engineering. *Joule* **2021,** *5*, 1816-1831.

90. Raghuwanshi, M.; Chugh, M.; Sozzi, G.; Kanevce, A.; Kühne, T. D.; Mirhosseini, H.; Wuerz, R.; Cojocaru-Mirédin, O., Fingerprints Indicating Superior Properties of Internal Interfaces in Cu(In,Ga)Se_2 Thin-Film Solar Cells. *Adv. Mater.* **2022,** *34*, 2203954.
91. Yin, G.; Brackmann, V.; Hoffmann, V.; Schmid, M., Enhanced Performance of Ultra-Thin Cu(In,Ga)Se_2 Solar Cells Deposited at Low Process Temperature. *Sol. Energy Mater. Sol. Cells* **2015,** *132*, 142-147.
92. Yin, G.; Song, M.; Schmid, M., Rear Point Contact Structures for Performance Enhancement of Semi-Transparent Ultrathin Cu(In,Ga)Se_2 Solar Cells. *Sol. Energy Mater. Sol. Cells* **2019,** *195*, 318-322.
93. Lin, T.-Y.; Khatri, I.; Matsuura, J.; Shudo, K.; Huang, W.-C.; Sugiyama, M.; Lai, C.-H.; Nakada, T., Alkali-induced Grain Boundary Reconstruction on Cu(In,Ga)Se_2 Thin Film Solar Cells using Cesium Fluoride Post Deposition Treatment. *Nano Energy* **2020,** *68*, 104299.
94. Kim, K.; Jeong, I.; Cho, Y.; Shin, D.; Song, S.; Ahn, S. K.; Eo, Y.-J.; Cho, A.; Jung, C.; Jo, W.; Kim, J. H.; Choi, P.-P.; Gwak, J.; Yun, J. H., Mechanisms of Extrinsic Alkali Incorporation in CIGS Solar Cells on Flexible Polyimide Elucidated by Nanoscale and Quantitative Analyses. *Nano Energy* **2020,** *67*, 104201.
95. Schöppe, P.; Schönherr, S.; Chugh, M.; Mirhosseini, H.; Jackson, P.; Wuerz, R.; Ritzer, M.; Johannes, A.; Martínez-Criado, G.; Wisniewski, W.; Schwarz, T.; Plass, C. T.; Hafermann, M.; Kühne, T. D.; Schnohr, C. S.; Ronning, C., Revealing the Origin of the Beneficial Effect of Cesium in Highly Efficient Cu(In,Ga)Se_2 Solar Cells. *Nano Energy* **2020,** *71*, 104622.
96. Lin, Y.-C.; Hong, D.-H.; Hsieh, Y.-T.; Wang, L.-C.; Hsu, H.-R., Role of Mo:Na Layer on the Formation of $MoSe_2$ Phase in Cu(In,Ga)Se_2 Thin Film Solar Cells. *Sol. Energy Mater. Sol. Cells* **2016,** *155*, 226-233.
97. Carron, R.; Nishiwaki, S.; Feurer, T.; Hertwig, R.; Avancini, E.; Löckinger, J.; Yang, S.-C.; Buecheler, S.; Tiwari, A. N., Advanced Alkali Treatments for High-Efficiency Cu(In,Ga)Se_2 Solar Cells on Flexible Substrates. *Adv. Energy Mater.* **2019,** *9*, 1900408.
98. Caballero, R.; Kaufmann, C. A.; Eisenbarth, T.; Grimm, A.; Lauermann, I.; Unold, T.; Klenk, R.; Schock, H. W., Influence of Na on Cu(In,Ga)Se_2 Solar Cells Grown on Polyimide Substrates at Low Temperature: Impact on the Cu(In,Ga)Se_2/Mo Interface. *Appl. Phys. Lett.* **2010,** *96*, 092104.
99. Chung, C.-H.; Hong, K.-H.; Lee, D.-K.; Yun, J. H.; Yang, Y., Ordered Vacancy Compound Formation by Controlling Element Redistribution in Molecular-Level Precursor Solution Processed $CuInSe_2$ Thin Films. *Chem. Mater.* **2015,** *27*, 7244-7247.
100. Yu, S.; Gong, Y.; Jiang, J.; Wu, S.; Yan, W.; Li, X.; Huang, W.; Xin, H., Over 10% Efficient $CuIn(S,Se)_2$ Solar Cells Fabricated From Environmentally Benign Solution in Air. *Sol. RRL* **2019,** *3*, 1900052.
101. Yen, Y.-T.; Wang, Y.-C.; Chen, Y.-Z. C.; Tsai, H.-W.; Hu, F.; Lin, S.-M.; Chen, Y.-J.; Lai, C.-C.; Liu, W.; Wang, T.-H.; Hong, H.-F.; Chueh, Y.-L., Large Scale and Orientation-controllable Nanotip Structures on $CuInS_2$, Cu(In,Ga)S_2, $CuInSe_2$, and

Cu(In,Ga)Se_2 by Low Energy Ion Beam Bombardment Process: Growth and Characterization. *ACS Appl. Mater. Interfaces* **2014,** *6*, 8327-36.

102. Wu, S.; Jiang, J.; Yu, S.; Gong, Y.; Yan, W.; Xin, H.; Huang, W., Over 12% Efficient Low-Bandgap CuIn(S,Se)$_2$ Solar Cells with the Absorber Processed from Aqueous Metal Complexes Solution in Air. *Nano Energy* **2019,** *62*, 818-822.
103. Duan, B.; Guo, L.; Yu, Q.; Shi, J.; Wu, H.; Luo, Y.; Li, D.; Wu, S.; Zheng, Z.; Meng, Q., Highly Efficient Solution-Processed CZTSSe Solar Cells Based on a Convenient Sodium-Incorporated Post-Treatment Method. *J Energy Chem.* **2020,** *40*, 196-203.
104. Cojocaru-Mirédin, O.; Ghorbani, E.; Raghuwanshi, M.; Jin, X.; Pandav, D.; Keutgen, J.; Schneider, R.; Gerthsen, D.; Albe, K.; Scheer, R., Intense Sulphurization Process can lead to Superior Heterojunction Properties in Cu(In,Ga)(S,Se)$_2$ Thin-Film Solar Cells. *Nano Energy* **2021,** *89*, 106375.
105. Yu, S.; Li, B.; Jiang, J.; Liu, X.; Hao, S.; Han, S.; Yan, W.; Xin, H., Solution‐Processed Chalcopyrite Solar Cells: the Grain Growth Mechanism and the Effects of Cu/In Mole Ratio. *Adv. Energy Mater.* **2021,** *12*, 2103644.
106. Romanyuk, Y. E.; Hagendorfer, H.; Stücheli, P.; Fuchs, P.; Uhl, A. R.; Sutter-Fella, C. M.; Werner, M.; Haass, S.; Stückelberger, J.; Broussillou, C.; Grand, P.-P.; Bermudez, V.; Tiwari, A. N., All Solution-Processed Chalcogenide Solar Cells - from Single Functional Layers Towards a 13.8% Efficient CIGS Device. *Adv. Funct. Mater.* **2015,** *25*, 12-27.
107. Guo, Q.; Ford, G. M.; Hillhouse, H. W.; Agrawal, R., Sulfide Nanocrystal Inks for Dense Cu($In_{1-x}Ga_x$)($S_{1-y}Se_y$)$_2$ Absorber Films and Their Photovoltaic Perfoemance. *Nano Lett.* **2009,** *9*, 3060-3065.
108. McLeod, S. M.; Hages, C. J.; Carter, N. J.; Agrawal, R., Synthesis and Characterization of 15% Efficient CIGSSe Solar Cells from Nanoparticle Inks. *Prog. Photovoltaics Res. Appl.* **2015,** *23*, 1550-1556.
109. Wong, J.; Omelchenko, S. T.; Atwater, H. A., Impact of Semiconductor Band Tails and Band Filling on Photovoltaic Efficiency Limits. *ACS Energy Lett.* **2020,** *6*, 52-57.
110. Son, Y.-S.; Yu, H.; Park, J.-K.; Kim, W. M.; Ahn, S.-Y.; Choi, W.; Kim, D.; Jeong, J.-H., Control of Structural and Electrical Properties of Indium Tin Oxide (ITO)/Cu(In,Ga)Se_2 Interface for Transparent Back-Contact Applications. *J Phys. Chem. C* **2019,** *123*, 1635-1644.
111. Barange, N.; Chu, V. B.; Nam, M.; Ahn, I.-H.; Kim, Y. D.; Han, I. K.; Min, B. K.; Ko, D.-H., Ordered Nanoscale Heterojunction Architecture for Enhanced Solution-Based $CuInGaS_2$ Thin Film Solar Cell Performance. *Adv. Energy Mater.* **2016,** *6*, 1601114.
112. Yuan, Z.-K.; Chen, S.; Xie, Y.; Park, J.-S.; Xiang, H.; Gong, X.-G.; Wei, S.-H., Na-Diffusion Enhanced p-type Conductivity in Cu(In,Ga)Se_2: A New Mechanism for Efficient Doping in Semiconductors. *Adv. Energy Mater.* **2016,** *6*, 1601191.
113. Chantana, J.; Nishimura, T.; Kawano, Y.; Suyama, N.; Yamada, A.; Kimoto, Y.; Kato, T.; Sugimoto, H.; Minemoto, T., Aging Effect of a Cu(In,Ga)(S,Se)$_2$ Absorber on the

Photovoltaic Performance of Its Cd-Free Solar Cell Fabricated by an All-Dry Process: Its Carrier Recombination Analysis. *Adv. Energy Mater.* **2019,** *9*, 1902869.

114. Fan, P.; Lin, J.; Hu, J.; Yu, Z.; Zhao, Y.; Chen, S.; Zheng, Z.; Luo, J.; Liang, G.; Su, Z., Over 10% Efficient Cu_2CdSnS_4 Solar Cells Fabricated from Optimized Sulfurization. *Adv. Funct. Mater.* **2022,** *32*, 2207470.
115. Nakada, T., Microstructural and Diffusion Properties of CIGS Thin Film Solar Cells Fabricated using Transparent Conducting Oxide Back Contacts. *Thin Solid Films* **2005,** *480-481*, 419-425.
116. Gouillart, L.; Cattoni, A.; Goffard, J.; Donsanti, F.; Patriarche, G.; Jubault, M.; Naghavi, N.; Collin, S., Development of Reflective Back Contacts for High-Efficiency Ultrathin Cu(In,Ga)Se_2 Solar Cells. *Thin Solid Films* **2019,** *672*, 1-6.
117. Ishizuka, S.; Nishinaga, J.; Beppu, K.; Maeda, T.; Aoyagi, F.; Wada, T.; Yamada, A.; Chantana, J.; Nishimura, T.; Minemoto, T.; Islam, M. M.; Sakurai, T.; Teradaf, N., Physical and Chemical Aspects at the Interface and in the Bulk of $CuInSe_2$-Based Thin-Film Photovoltaics. *Phys. Chem. Chem. Phys.* **2022,** *24*, 1262-1285.
118. Heinemann, M. D.; Efimova, V.; Klenk, R.; Hoepfner, B.; Wollgarten, M.; Unold, T.; Schock, H.-W.; Kaufmann, C. A., Cu(In,Ga)Se_2 Superstrate Solar Cells: Prospects and Limitations. *Prog. Photovoltaics Res. Appl.* **2015,** *23*, 1228-1237.
119. Keller, J.; Stolt, L.; Donzel-Gargand, O.; Kubart, T.; Edoff, M., Wide-Gap Chalcopyrite Solar Cells with Indium Oxide–Based Transparent Back Contacts. *Sol. RRL* **2022,** *6*, 2200401.
120. Chirilă, A.; Reinhard, P.; Pianezzi, F.; Bloesch, P.; R., U. A.; Fella, C.; Kranz, L.; Keller, D.; Gretener, C.; Hagendorfer, H.; Jaeger, D.; Erni, R.; Nishiwaki, S.; Buecheler, S.; Tiwari, A. N., Potassium-Induced Surface Modification of Cu(In,Ga)Se_2 Thin Films for High-Efficiency Solar Cells. *Nat. Mater.* **2013,** *12*, 1107-11.
121. Villanueva-Tovar, A.; Kodalle, T.; Kaufmann, C. A.; Schlatmann, R.; Klenk, R., Limitation of Current Transport across the Heterojunction in Cu(In,Ga)Se_2 Solar Cells Prepared with Alkali Fluoride Postdeposition Treatment. *Sol. RRL* **2020,** *4*, 1900560.

DOI: 10.17185/duepublico/82326
URN: urn:nbn:de:hbz:465-20240819-150807-9